UNIVERSITY OF SOUTHAMPTON

FACULTY OF ENGINEERING AND PHYSICAL SCIENCES

Physics and Astronomy

Optical Properties of Lead Halide Perovskites for Optoelectronics

by

Christopher Bailey

Orchid ID: 0000-0001-6593-1381

A thesis submitted in partial fulfillment for the degree of Doctor of Philosophy

November 2019

UNIVERSITY OF SOUTHAMPTON

ABSTRACT

FACULTY OF ENGINEERING AND PHYSICAL SCIENCES

Physics and Astronomy

Doctor of Philosophy

OPTICAL PROPERTIES OF LEAD HALIDE PEROVSKITES FOR OPTOELECTRONICS

by Christopher Bailey

This thesis presents a collection of work investigating the optical properties of lead halide perovskites for optoelectronic applications. Lead halide perovskites are currently the state–of–the–art in terms of efficiency for thin-film photovoltaics, yet they are not fully understood and require further studies to elucidate their fundamental properties. Firstly in this thesis, the optical constants for lead halide perovskite thin films are determined using spectroscopic ellipsometry, providing important information for future optical modelling and calculations of the electronic structure. Following this, physical insights into the charge carrier dynamics in these materials are provided, revealing the effects of material disorder over a large range of temperatures. In relation to the charge carrier dynamics, the crucial topic of grain boundaries in lead halide perovskites is also investigated, showing their detrimental effects by providing non-radiative recombination centres in perovskite materials. Lastly, an application of colloidal semiconductor nanocrystals for perovskite solar cells is investigated, with the aim to enhance photocurrent in the devices. The prospect of this is shown by the successful dispersion of colloidal CdTe core-type quantum dots in the hole–transporting layer within solution-processed photovoltaic devices. This work is a promising advancement towards perovskite solar cells employing additional light harvesting processes from nanomaterials.

Contents

List of Figures

List of Tables

Publications

- Phonon-Assisted Trapping and Re-excitation of Free Carriers and Excitons in Lead Halide Perovskites

  Giacomo M. Piana, Christopher G. Bailey, and Pavlos G. Lagoudakis

  The Journal of Physical Chemistry C **2019** *123* (32), 19429-19436

- High-Energy Optical Transitions and Optical Constants of $CH_3NH_3PbI_3$ Measured by Spectroscopic Ellipsometry and Spectrophotometry

  Christopher G. Bailey, Giacomo M. Piana, and Pavlos G. Lagoudakis

  The Journal of Physical Chemistry C **2019**

- Influence of Grain Boundaries on Recombination in Lead Halide Perovskites

  Christopher G. Bailey, Giacomo M. Piana, Katarzyna Rechcińska, and Pavlos G. Lagoudakis – In preparation

Conferences

- Effect of Illumination, Ambient Conditions, and Grain Size on Recombination Dynamics in Lead Halide Perovskites

  Christopher G. Bailey, Giacomo M. Piana, and Pavlos G. Lagoudakis

  International Conference on Physics of Light-Matter Coupling in Nanostructures (PLMCN-20), Moscow, 2019

- Phonon-assisted Trapping of Carriers in Lead Halide Perovskites

  Giacomo M. Piana, Christopher G. Bailey, and Pavlos G. Lagoudakis

  Hybrid and Organic Photovoltaics (HOPV), Rome, 2019

- Inverted Planar Perovskite Solar Cells with Hybrid Quantum Dot and PEDOT:PSS Hole-Transporting Layer

  Christopher G. Bailey, Giacomo M. Piana, and Pavlos G. Lagoudakis

  UK Semiconductors, Sheffield, 2018

Declaration of Authorship

I Christopher Bailey, declare that the thesis entitled *Optical Properties of Lead Halide Perovskites for Optoelectronics* and the work presented in the thesis are both my own, and have been generated by me as the result of my own original research. I confirm that:

- This work was done wholly or mainly while in candidature for a research degree at this University;
- Where any part of this thesis has previously been submitted for a degree or any other qualification at this University or any other institution, this has been clearly stated;
- Where I have consulted the published work of others, this is always clearly attributed;
- Where I have quoted from the work of others, the source is always given. With the exception of such quotations, this thesis is entirely my own work;
- I have acknowledged all main sources of help;
- Where the thesis is based on work done by myself jointly with others, I have made clear exactly what was done by others and what I have contributed myself;
- Parts of this work have been published in Ref [68]

Signed:.....

Date:.....

Acknowledgements

Firstly, I am extremely grateful for the work carried out by colleagues in the Laboratories for Hybrid Optoelectronics (Hybrid Photonics group) in Southampton. Thanks to Giacomo Piana for being incredibly patient colleague and friend, with my millions of basic questions about optics and constant bothering of him in the lab. Thanks to my supervisor Pavlos Lagoudakis for and all other academic staff for the guidance during of the project and keeping me in an excited state. They have provided extensive input during regular meetings and correspondence, providing both structure and momentum to the research. Thanks to all my collaborators and other colleagues including Peter Shaw, Tasmiat Rahman, Edris Khorani, Thomas Mercier, Nicholas Klokkou, Abinash Poudel, Kevin Dannecker, Philip Hank and Lucas Brand. Everyone involved has contributed tremendously with substantial effort and efficiency. I am also thankful to Mike Stringer and Ben Freestone (University of Sheffield) for invaluable discussions and advice.

I also acknowledge my partner, my friends, my current housemates, and my family for their support during my studies. Sorry to my mum and dad for not sending enough messages or calling often enough at times. Thanks to my dog Maple, who has helped so much in stabilising my lifestyle and proof-reading my work, listening to my presentations etc. Thanks to all of the group for the amazing parties, coffee breaks and DnD sessions. Thanks to Nick for all the normalising discussions about PhD life. Thanks to Abi for always providing unique perspectives, playing sports with me, and sharing adventures. Thanks to all my friends at home, enhancing the nostalgic trips back to Wales.

I am thankful to the EPSRC for funding this project as part of the Centre for Doctoral Training in New and Sustainable Photovoltaics (CDT-PV). Thanks to everyone in CDT-PV, especially cohort 2 for providing an incredible and unique first year of the PhD. The CDT-PV has been an excellent experience providing a dynamic learning opportunity. Due to all this help, I have absorbed a broad spectrum of knowledge during my PhD studies, which has reflected so much in my confidence and ability. I feel truly privileged to have been a student for so long and hope that I can continue to learn as much science stuff as possible before I'm dead.

Chapter 1

Introduction

Fossil fuels are our primary source of energy but due to the finite reserves, it is estimated that only a few hundred years' supply is available at our current rate of consumption, which is ever increasing. As the concentration of gas in the atmosphere that contributes to global warming increases due to this fossil–fuel consumption, deforestation, and many other factors, we are beginning to observe the unprecedented detrimental effects. One such effect is a rise in global average temperature, with 16 of the 17 warmest years ever recorded having occurred since 2001 [1] and a likely range of global temperature increase of 2.0 – 4.9 °C by the year 2100 [2]. By of diversifying our energy portfolio, these effects can be minimised and economic benefits may be enjoyed due to the use of locally available energy resources. Renewable energy sources provide the ideal mechanism of achieving this. For example, converting energy from sunlight at only 10 % efficiency, using 1 % of Earth's land area would deliver twice the world's energy demand [3]. One solar-energy conversion technology is photovoltaic (PV) solar cells, which convert sunlight directly into electricity. One of the major drawbacks with PV technologies is that they are initially more expensive than many other sources of electricity. Costs for PV systems are dropping, from over $100 per peak watt in the 1970s to now less than $0.50 [4]. Despite this, production costs still need to continue to decrease considerably, however there are many other factors that influence the success of PV as a renewable energy technology. The properties that are currently targeted by scientific research and

engineering include the energy cost of producing solar cells, the applicability of PV systems for various scenarios, and of course, the performance of the devices.

Most PV systems that are produced, sold and implemented are based on the material silicon. This is one of many contributions to the expense of PV systems but another issue is the energy required to produce silicon solar cells. Although silicon is abundant, the process to produce solar cells from raw material is very energy intensive and in most cases it takes several years for a PV system to produce the same amount of energy used in its production. One other major drawback of silicon-based PV is that due to fundamental limitations (and current manufacturing techniques), the resulting solar cells are relatively thick (several µm is required, but in practice > 100 µm is used). As a result, silicon photovoltaics cannot provide the solution to applications that require flexible or semi-transparent devices. However, emerging 'thin-film' technologies aim to fill this gap, using different photovoltaic materials that can be used to manufacture solar cells, with entire devices being on the order of 1 µm in thickness. A group of materials called 'perovskites' have emerged in the field of thin-film photovoltaics in the past decade. Perovskite is the name given to the family of materials that share the crystal structure of calcium titanate ($CaTiO_3$). Many of these materials have gained recent interest in the fields of optoelectronic devices such as solar cells [5], light emitting diodes [6], photodetectors [7] and lasers [8, 9]. They have the general chemical formula of ABX_3, where A can be an inorganic or organic cation, B is a smaller metal cation and X is an anion bonding to both. For photovoltaic (PV) applications, A is usually methylammonium 'MA' ($CH_3NH_3^+$), formamidinium 'FA' ($CH(NH_2)_2^+$) or Cs^+, B is Pb_2^+ or Sn_2^+, and X is a halide such as I^-, Cl^- or Br^-. Methylammonium lead iodide or $MAPbI_3$, with the formula $CH_3NH_3PbI_3$, is the archetypal perovskite material pertaining to PV. $MAPbI_3$ was first reported in the cubic perovskite phase in 1978 [10] but it was not until 2009 that the first solar cell was reported using $MAPbI_3$ as the absorbing layer [11]. Since, the power conversion efficiency (PCE) of perovskite solar cells has inclined rapidly with the record device now reaching a PCE over 25 % [12], with state-of-the-art devices comprised of mixed-cation, mixed-halide perovskites.

Entire perovskite solar cells (PSCs) can be fabricated to be < 1 µm thick due to the high

absorption coefficient of the active layer [13, 14] and can be entirely solution-processed at low temperatures. Their success as solar cell materials is owed to these factors and also other factors such as the high yield of free charges following photo-excitation, slow charge recombination, and excellent ambipolar charge transport properties [15–17]. Additionally, the optical bandgap of perovskites can be tuned between 1.30 – 2.30 eV by varying the X-site halide or A-site cation content [18–23], providing the potential for perovskite tandem solar cells utilising a larger portion of the solar spectrum. This can be achieved using more than one layer of perovskite of varying composition [24–26] or combining a perovskite absorbing layer with an absorbing layer of a different material. The latter have been fabricated using silicon for example, with a record PCE of 28 % [12, 27–30] and also copper indium gallium diselenide (CIGS) with $>$ 20 % PCE [31–33]. Wide-bandgap perovskites also present an application for building-integrated PV, as modules can be made transparent to a portion of the visible spectrum and hence integrated with windows [34–40].

Since the emergence of perovskite solar cells, device performances have improved predominantly via empirical research, with studies of optimisation of fabrication techniques leading the progress. As a result, the understanding of the science underpinning the success of the technology has naturally taken the back seat and hence is currently lagging behind. However, when the technology begins to approach the theoretical limit of its performance, an exhaustive comprehension of the fundamental mechanisms responsible for its success will be come of greater importance. Moreover, the unique science of perovskites can be of interest to other fields of optoelectronics and also fundamental semiconductor physics.

Another broad group of materials of interest to PV are those that have at least one dimension on the manometer scale, known as ‘nanomaterials’. Particular examples that have been applied to photovoltaic technology include semiconductor nanocrystals, plasmonic nanoparticles and upconversion nanoparticles. In general, these examples of nanomaterials have desirable optical properties relating to PV that are unique to their material class. Nanocrystals for example have high absorption cross-section and the ability to tune their optical energy-bandgap by varying their size only. Spherical

nanocrystals that are deposited from a colloidal solution, known as colloidal quantum dots (CQDs) have been implemented with limited success in solar cell technologies with the active layer exclusively comprised of QDs. CQD solar cells are limited by their charge transport properties which are hindered by insulating molecules surrounding each QD, necessary in most cases to prevent aggregation of material when dispersed in a liquid solution. Hence, the world record PCE for QD solar cells is just 16.6% [12].

Another approach is to utilise the optical properties of nanotechnology and the proficient charge-transport properties of bulk semiconductors to form hybrid-technology optoelectronic devices [41]. Nanocrystals have been hybridised with bulk semiconductors in solar cells where processes such as luminescent down-shifting (LDS) and resonant energy transfer (RET) have been utilised to convert higher energy photoexcited states to lower energy excited states. The nanocrystals can by used to absorb light and transfer the energy non-radiatively via RET or radiatively via LDS to the bulk semiconductor PV material. Due to the tunability of the nanocrystals, light from any portion of the solar spectrum can be efficiently harvested, regardless of the spectral response of the bulk PV material. Such principles have been demonstrated for inorganic PV devices [42–44] and also light-emitting diodes [45, 46], where the principles are reversed; the superior electrical properties of bulk semiconductors are exploited to inject charge into the highly emissive nanocrystals. A similar approach has also been adopted for upconversion and plasmonic nanoparticles. The former are used to convert multiple lower energy photons to a photon with higher energy, optimised for absorption by the bulk PV material in a device [47] whereas the latter are used in devices to increase photon scattering in the plane of the device [48].

1.1 Thesis Structure and Style

This thesis is comprised of nine chapters in total, with four covering the main experimental research work carried out during this PhD project. The writing style changes accordingly throughout the thesis, switching between the active and passive voice. The

research chapters use mainly the active voice, since this is more appropriate when reporting results, especially from collaborative work. Each of these chapters begins with an introduction, then several sections that essentially comprise the results and discussion, lastly finishing with a conclusion and note on contributions.

Chapter 2 is an introduction to the science of PV, highly relevant to the later chapters. Starting with bulk semiconductors, the chapter continues through to the physics of full PV devices.

Chapter 3 follows from the theoretical background by a reviewing the literature associated with perovskite materials for PV, which has become a very rich, diverse, and currently highly active research field. This is necessary as the reader may be unaware of the major differences and uniqueness of perovskite materials in comparison to traditional semiconductors. Moreover, there have been many recent advances in both theoretical and experimental work surrounding this material confined mainly within past decade, which are worth covering.

Chapter 4 covers the experimental techniques and processes that are utilised in subsequent chapters. All the techniques mentioned in the later experimental chapters are touched on, with more in-depth sections for those most important for the experiments in the thesis.

Chapter 5 is the first experimental research chapter of the thesis. Here, spectroscopic ellipsometry and spectrophotometry is used to identify optical transitions in $MAPbI_3$ thin films and determine the optical constants over a wide spectral range. The work provides the reader with a step-by-step process of analysing ellipsometry data for thin absorbing films such as $MAPbI_3$. The work provides important information relating to the band structure of $MAPbI_3$ and the potential applications of the material.

Chapter 6 presents a study of the charge carrier recombination in lead halide perovskite thin films. It is the first chapter in which the photoluminescence properties of perovskites are studied. In the chapter, absorption spectroscopy is used to show that there is a coexistence of structural phases in $MAPbI_{3-x}Cl_x$ at low temperatures. The data from these experiments is further analysed to determine the binding energy for excitons in the

material across a range of temperatures. A model is produced to describe recombination of free carriers and excitons, showing that both are subject to trapping and re-excitation via shallow traps. This provides an explanation for unusually long lifetimes observed in lead halide perovskites. Analysis of the trap-state density versus temperature suggests that their main origin is a consequence of disorder, which is increased at temperatures close to the phase transition.

Chapter 7 follows from chapter 6, where the photoluminescence properties are observed in more detail. The effect of grain boundaries on the photoluminescence properties is revealed by utilising scanning near-field optical microscopy to map the photoluminescence on a nano-scale.

Chapter 8 is the final experimental chapter, outlining subjects of future research. Colloidal inorganic semiconductor QDs are applied to inverted planar perovskite solar cells. Photovoltaic devices using a PEDOT:PSS/QD hole-transporting layer are fabricated, with an enhancements observed compared to reference devices without QDs.

Chapter 9 marks the end of main body of the thesis, summarising the work and providing an outlook on the research.

Chapter 2

Theoretical Background

2.1 Bulk Semiconductors for Optoelectronics

A **semiconductor** is a type of solid with electrical conductivity lying between that of a **conductor** (i.e. metal) and an **insulator**. Semiconductors are the most important materials for optoelectronic devices, including solar cells. Therefore the science of semiconductors is a natural starting point for understanding the properties of photovoltaic (PV) materials and ultimately the design of the devices. In solar cells they are used as the active layer where light is absorbed and charge is generated. They are also used as the charge extraction layers, allowing electrical energy to be used in an external circuit. This section introduces some basic concepts of semiconductor physics, which will be prerequisite for the next section and later chapters. Semiconductors exist in many forms and can be comprised of many different chemical compounds. Semiconductors may be elemental such as silicon, the most well-known and applied semiconductor, or carbon in many different forms such as fullerenes and nanotubes. They may also be **inorganic** compounds such as GaAs or CdTe, or **organic** compounds such as regioregular poly(3-hexylthiophene-2,5-diyl) (P3HT). These all have a range of different periodic (crystalline) structures, giving rise to delocalisation of electrons and hence conductivity. Yet they differ from metals as their conduction and valence energy bands do not overlap (Figure 2.1), as will be explained in the following sections.

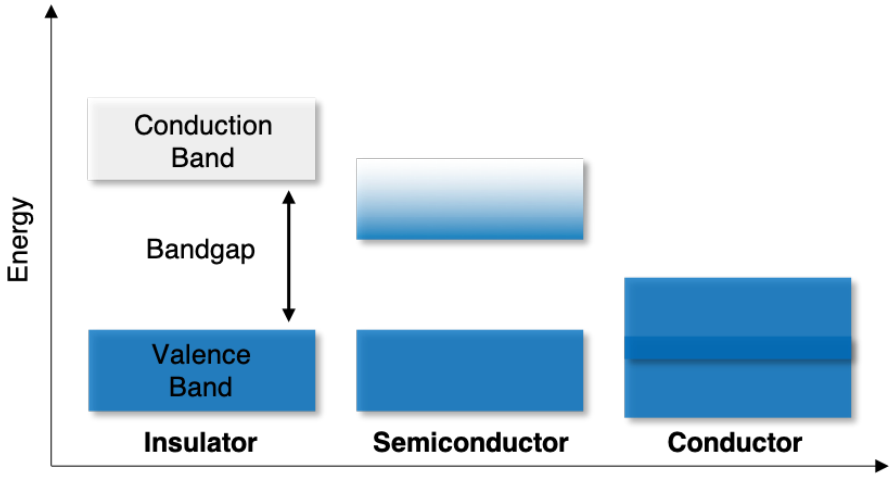

Figure 2.1: Energy bands in solids. Solid materials can be grouped in to three categories depending on their electrical conductivity. Insulators low conductivity, with a large gap between the conduction and valence bands. Conductors have the high conductivity and their valence and conduction band overlap. Semiconductors are have intermediate values of conductivity, with a moderate gap between their conduction and valence bands, usually falling between the infrared and ultraviolet photon energies.

2.1.1 Electronic Structure

The major distinguishing feature of semiconductors is the presence of energy gaps (the **bandgap**) in their electronic structure that can be observed experimentally from excitation spectra. This means that a material will only absorb photons that have an energy equal to or greater than the width of the gap. Although insulating materials also possess an energy gap, their conductivity at room temperature is significantly lower due to the larger width of the gap. Semiconductors are defined conventionally as materials with resistivity in the range of 10^{-2} – 10^{9} Ω cm or materials that possess an energy gap of 0 – 4 eV [49]. Hence, most of the interaction between semiconductors and light occurs in the ultraviolet, visible and infrared portions of the electromagnetic spectrum.

By close examination of the energy-band structure of a material, many fundamental properties and much of its behaviour can be understood. Quantum mechanics provides a suitable description for the interactions of electrons in a semiconductor with a periodic potential, such as that found in a crystalline material. However, solving the many-body problem for the large number of electrons in such solids is not possible, so **group theory** is utilised for this analysis. By combining this mathematical tool with some major

approximations, various computational techniques can be used to calculate electronic band structures. The choice of approximations is crucial and should depend on which properties are to be investigated. Methods using very few approximations have been developed that can calculate the resulting energy from all interactions between particles in a crystalline system. These *"ab initio"* techniques have proven successful for both predicting and providing explanation for optoelectronic properties of semiconductors.

An example of a commonly used approximation is the **Born-Oppenheimer approximation**. Since the ions in a crystal are far heavier than the electrons, they vibrate much more slowly (at a lower frequency), typically less than 10^{13} s^{-1} [49]. In order to excite electrons in a semiconductor, an energy greater than the bandgap is required. This is on the order of 1 eV for most semiconductors, corresponding to a frequency of 10^{15} s^{-1}. Using this as an estimate for the response time for electrons, the ions can be considered stationary from the perspective of the electrons. The ions only interact with a time-averaged adiabatic electronic potential. Considering this approximation, the Hamiltonian of an ideal crystal is the sum of three terms:

$$\hat{H} = \hat{H}_{ions}(\boldsymbol{R}_j) + \hat{H}_e(\boldsymbol{r}_i, \boldsymbol{R}_{j0}) + \hat{H}_{e-ions}(\boldsymbol{r}_i, \delta\boldsymbol{R}_j), \tag{2.1}$$

where $\boldsymbol{R}_j$ is the position of the jth ion and $\boldsymbol{r}_i$ is the position of the ith electron. $\hat{H}_{ions}(\boldsymbol{R}_j)$ is the contribution from the total ionic motion, $\hat{H}_e(\boldsymbol{r}_i, \boldsymbol{R}_{j0})$ is the electronic Hamiltonian with stationary ions in their equilibrium positions $\boldsymbol{R}_{j0}$ and $\hat{H}_{e-ions}(\boldsymbol{r}_i, \delta\boldsymbol{R}_j)$ is the electron–phonon interaction arising from the change in energy caused by movement of ions $\delta\boldsymbol{R}_j$ from the equilibrium positions. Importantly, the electronic Hamiltonian is given by

$$\hat{H}_e(\boldsymbol{r}_i, \boldsymbol{R}_{j0}) = \sum_i \frac{p_i^2}{2m_i} + \frac{1}{2}\sum_{i,i'}{}' \frac{e^2}{4\pi\epsilon_0 \mid \boldsymbol{r}_i - \boldsymbol{r}_{i'} \mid} - \sum_{i,j} \frac{Z_j e^2}{4\pi\epsilon_0 \mid \boldsymbol{r}_i - \boldsymbol{R}_{j0} \mid}. \tag{2.2}$$

Here, p_i is the momentum operator for electrons, m_i is the mass of the electron, Z_j is the atomic number of the nucleus and $\sum'$ denotes a summation only over pairs of non-identical indices.

The final major approximation is that all electrons experience the same average potential

$V(\boldsymbol{r})$ (the mean-field approximation). As a result, the Schrödinger equation for a single electron becomes:

$$\hat{H}_{e1}\psi_n(\boldsymbol{r}) = \left(\frac{p^2}{2m_i} + V(\boldsymbol{r})\right)\psi_n(\boldsymbol{r}) = E_n\psi_n(\boldsymbol{r}) \tag{2.3}$$

where $\hat{H}_{e1}$ is the single-electron Hamiltonian, $\psi_n(\boldsymbol{r})$ is the wavefunction eigenstate and E_n is the corresponding energy eigenvalue. To obtain these energy states, $V(\boldsymbol{r})$ must first be calculated. This can be achieved using various approaches with knowledge of the geometrical symmetry of a crystal. Self-consistent approaches including Hartree or Hartree-Fock are more complicated whereas simpler methods consider a periodic arrangement of screened Coulomb potentials.

2.1.2 Energy Bandgap and Transitions

There are essentially two main categories of band structure calculations. The first group of methods involve adding terms to the periodic electronic potential as perturbations. The weak periodic potentials are called pseudopotentials and therefore these methods are known as **pseudopotential methods**. The second category of techniques starts from the atomic orbitals of the atoms that form the solid. The orbitals positioned at every atom site are summed over in the crystal and the interaction between neighbouring sites is considered and hence the wave function overlap is the perturbation. These methods include the **linear combination of atomic orbitals** (LCAO) and the **tight-binding method**.

Regardless of approach adopted, it is found that electron states in a periodic potential form bands of energy that may have gaps between, where no states exist. The eigenstates of the electrons in a periodic potential are referred to as **Bloch waves**, given by

$$\phi_{\boldsymbol{k},i}(\boldsymbol{r}) = e^{i\boldsymbol{k}\boldsymbol{r}}u_{\boldsymbol{k},i}(\boldsymbol{r}), \tag{2.4}$$

where

$$u_{\boldsymbol{k},i}(\boldsymbol{r}) = u_{\boldsymbol{k},i}(\boldsymbol{r})(\boldsymbol{r} + \boldsymbol{R}), \tag{2.5}$$

$\boldsymbol{k}$ is the wavevector and i is the index of the energy band. The Bloch waves are hence a product of a plane wave and a lattice periodic term $u_{\boldsymbol{k},i}(\boldsymbol{r})$. The periodicity allows the dispersion relation (E versus $\boldsymbol{k}$) to be reduced to the first Brillouin zone (primitive cell in the reciprocal lattice). The extrema of energy bands tend to lie in the centre and the edges of the Brillouin zone. The energy bands are most often approximately parabolic at the extrema, shown in Figure 2.2. Band calculations of semiconductors result in a

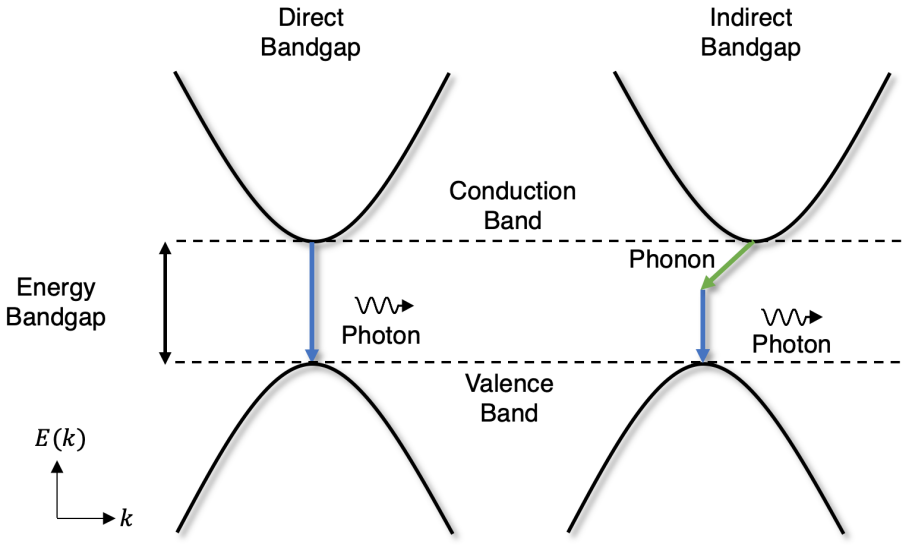

Figure 2.2: Dispersion for direct- and indirect- semiconductors. The allowed energy levels in a semiconductor form almost continuous bands of levels, separated by a gap of forbidden energy values. Indirect-bandgap semiconductors allow electronic transitions between bands via absorption or emission of phonons. Indirect-bandgap semiconductor transitions require phonon absorption or emission additionally, due to momentum conservation.

formation of a gap in the allowed energy levels for electrons in a semiconductor. Bands of energy levels form with very little energy difference between the discrete states they contain and thus the bands can be treated as almost continuous, with electrons able to occupy any energy within the band. However, only two electrons of different spin may occupy each state (Pauli's exclusion principle). The bands of energy above the gap are referred to as the conduction bands since electrons that occupy states within the band are mobile and hence can contribute to conduction. The bands below the gap are referred to as valence bands since they are comprised of states belonging to valence electrons. The gap forms at the **Fermi level** (E_F), between the absolute conduction band minimum and valence band maximum. The Fermi level is an energy level that has a 50% probability of

being occupied by an electron at any given time at thermal equilibrium. However, if the Fermi level lies within the bandgap such as in a semiconductor, an electron is forbidden from occupying it of course, which renders the Fermi level only a statistical entity. At zero temperature, the energy states of the valence band should be completely occupied by electrons and the conduction-band states empty. Since electrons are Fermions, they obey Fermi-Dirac statistics and their energy distribution is therefore given by the Fermi-Dirac distribution, $f(E)$ at thermal equilibrium:

$$f(E) = \frac{1}{e^{(E-E_F)/k_BT} + 1} \tag{2.6}$$

The distribution is a function of the temperature, T and the Fermi level, E_F, and also includes Boltzmann's constant, k_B. Since the Fermi energy lies within the bandgap for semiconductors, the population of energy states within the conduction band will zero at zero temperature, and can only become occupied non-zero temperatures (Figure 2.3). Semiconductors can have the ability to absorb and emit light, transferring energy be-

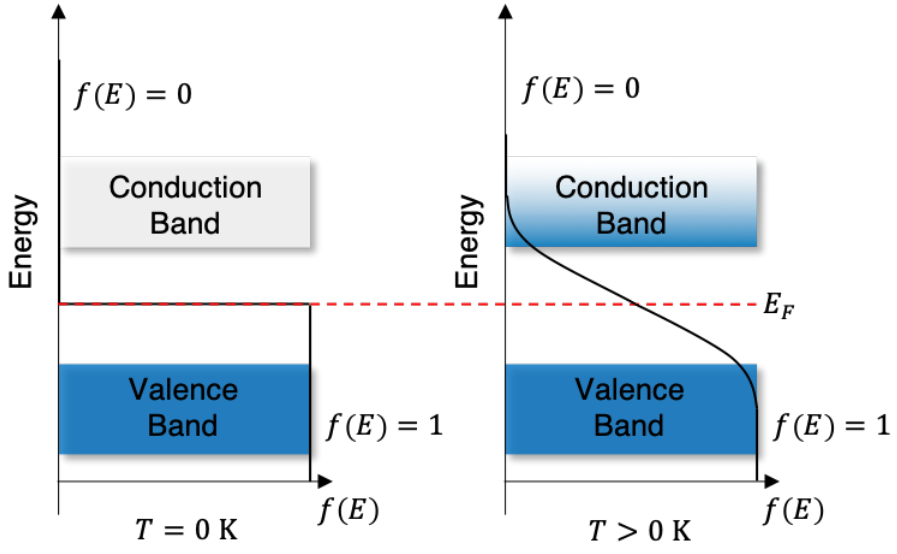

Figure 2.3: Effect of temperature on the occupancy of states in a semiconductor. At zero temperature, all electrons occupy states in the valence band only. As the temperature is increased, the Fermi-Dirac distribution dictates the occupancy of electrons and can be non-zero in the conduction band, allowing electrons to occupy states within it.

tween photons, electrons and phonons within the material. If photons have sufficient energy, they may excite electrons from energy states in the filled valence bands to states

in the empty conduction bands. Therefore, optical spectroscopy measurements of semiconductors are can be used effectively to gain an insight to their electronic properties. Often photons can also interact with phonons and with charges localised on defects, which can also be investigated via optical spectra. Their optical properties are the basis of their applications as optoelectronic devices.

A material is referred to as a **direct-bandgap** semiconductor if its absolute conduction band minimum lies at the same $\boldsymbol{k}$ as the valence band maximum. This is often at the Γ-point (i.e. $\boldsymbol{k} = 0$) of the Brillouin zone. Semiconductors for which this is not the case (energy band extrema lie at different $\boldsymbol{k}$ value) are said to have an **indirect bandgap**. Semiconductors with a direct-bandgap can absorb and emit photons easily. The reason for this is that electronic transitions between band extrema via only photon interactions are allowed, since photons with energies similar to the bandgap energy have almost no momentum on the scale of the Brillouin zone. Hence the transition is almost purely a transfer of energy, given by a vertical transition, as depicted in Figure 2.2. For an indirect-bandgap semiconductor to absorb or emit photons, momentum must be contributed to (or transferred from) the electron for the transition to occur. This is usually facilitated by electron–phonon interactions and is one of the many ways temperature plays an important role in the behaviour of semiconductors, regarding their optical properties.

2.1.3 Fermi's Golden Rule

Fermi's Golden Rule has importance in semiconductors regarding electron transitions as most cases can be described using this approximation, which is based on first order perturbation theory. Fermi's Golden Rule for the the full quantum mechanical transition rate and states that the probability per unit time of a transition from an initial filled state $|i\rangle$ with an energy E_i to a final empty state $|i\rangle$ with energy E_f with an energy difference of E due to the result of a perturbing Hamiltonian $\hat{\boldsymbol{H}}'$ is given by

$$\frac{2\pi}{\hbar}|\langle i|\hat{\boldsymbol{H}}'|f\rangle|^2\delta(E_\mathrm{f} - E_\mathrm{i} \pm E). \tag{2.7}$$

The bracketed term is a matrix element coupling initial and final states, describing the interaction under perturbation from a light field, phonon interactions, carrier interactions etc.

Band-to-band transitions occur during free-carrier generation and recombination. In a perfect direct-bandgap semiconductor only radiative recombination occurs since this is the only thermodynamically unavoidable form of recombination, as discussed in the following section. In indirect-bandgap semiconductors, such as silicon and germanium, electron–hole pairs can recombine radiatively only via phonon-assisted transitions due to the difference in wavevector between the conduction band minimum and valence band maximum.

If τ_r is the lifetime of an electron and a hole before radiative recombination occurs and the free electron and hole concentrations are, n_e and n_h respectively, then the rate of photon emission following recombination is $n_e n_h/\tau_r$.

2.1.4 Free Charges and Excitons

The Coulombic interaction of electrons and holes with the same wavenumber gives rise to bound states called **excitons**, manifested just below the conduction band. From the hydrogenic effective mass equation in a crystal potential, the binding energies for exciton states are given by

$$E_{\mathrm{B}} = \frac{\mu^* \epsilon_0^2 R_{\mathrm{y}}}{m_{\mathrm{e}} \epsilon_{\mathrm{r}}^2 l^2}, \tag{2.8}$$

where μ^* is the reduced effective mass of the electron–hole pair, ϵ_r is the dielectric constant (relative permittivity) of the material, ϵ_0 is the permittivity of free space, R_y is the Rydberg energy and $l = 1, 2, 3...$ is the angular momentum quantum number.

The **exciton binding energy**, E_{B} in optoelectronic materials is an insightful value, since it determines the type of charge carriers that are predominant in the material under given conditions. The type of charge carriers generated by absorbed photons within photovoltaic materials affects both the electrical and optical characteristics significantly. If the exciton binding energy is large (excitons are tightly bound), the carriers formed are termed **Frenkel excitons**. Frenkel excitons typically have exciton binding energies

$>$ 100 meV and as a result may be observed at room temperature, where thermal energy is 26 meV. The types of carriers typically found in bulk (non-spatially confined) inorganic semiconductors at room temperature are free electrons and holes or weakly-bound excitons, known as **Wannier–Mott excitons**. This is due to their large dielectric constant, screening the coulombic interaction between electrons and holes; examples include group IV semiconductors such as silicon ($E_{\mathrm{B}} = 14.7$ meV) and compounds such as GaAs ($E_{\mathrm{B}} = 4.2$ meV) [50]. As a result, Wannier–Mott excitons are usually only observed at low temperatures in most bulk inorganic semiconductors. However, strong interaction in some ionic crystals mean that Frenkel excitons can actually exist, being localised to individual or two nearest-neighbour unit cells (Figure 2.4). Photo-generated carriers in

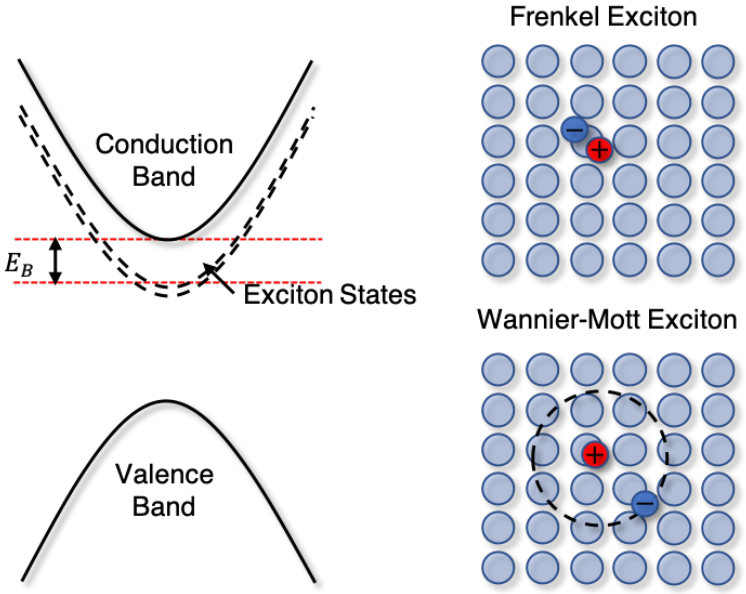

Figure 2.4: Types of excitons in semiconductors. Exciton states exist at energies just below the conduction band. The exciton binding energy is the energy difference between the conduction band and first exciton state. Frenkel excitons are often localised to individual unit cells, whereas Wannier–Mott excitons can span several unit cells.

organic semiconductor materials for photovoltaics such as P3HT, PCBM and PCDTBT manifest as Frenkel excitons, typically localised to individual molecules or unit cells of a molecular crystal.

2.2 Absorption and Emission Processes

2.2.1 Elliott's Theory

Elliott's theory describes the intensity of optical absorption of direct bandgap semiconductors near the band-edge. According to the model, the absorption coefficient is given by [51],

$$\alpha(E) = \frac{A}{E}\left(\sum_{n=1}^{\infty}\frac{4\pi E_B^{\frac{3}{2}}}{n^3}\delta\left(E-\left(E_G-\frac{E_B}{n^2}\right)\right)+\frac{2\pi\sqrt{\frac{E_B}{E-E_G}}}{1-\exp\left(-2\pi\sqrt{\frac{E_B}{E-E_G}}\right)}\theta(E-E_G)\right) \tag{2.9}$$

where E is the photon energy, A is a scaling factor that accounts for the transition dipole moment $\langle\psi_v|q\mathbf{r}|\psi_c\rangle^2$, E_B is the exciton binding energy and E_G is the bandgap energy. The theory encompasses the contribution of absorption of photons by both exciton states within the bandgap, and also via band-to-band transitions. The former is characterised by a series of delta functions due to the discrete nature of exciton transitions. The band-to-band (free-carrier) absorption is described by a step function, proportional the square root of the photon energy for all real values of $\sqrt{(E-E_G)}$ and zero elsewhere. This function represents the **joint density of states** in a direct bandgap semiconductor. Figure 2.5 shows the typical shape of equation 2.9, where the transitions are broadened due to electron–phonon interactions at non-zero temperatures.

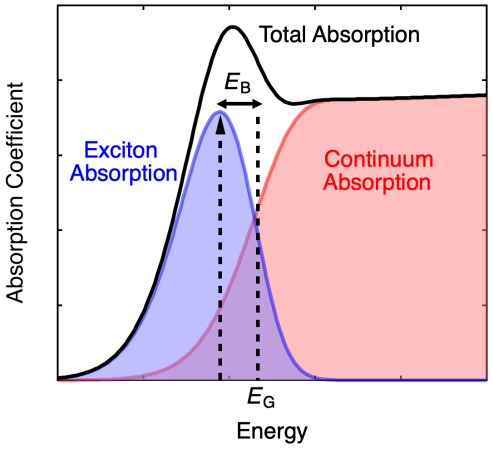

Figure 2.5: Elliott's theory for absorption in direct-bandgap semiconductors. Elliott's theory describes the absorption coefficient in terms of exciton and band-to-band transitions. The delta and step-like functions given in equation 2.9 are broadened due to electron–phonon interactions.

2.2.2 Photoluminescence

Photoluminescence is the **spontaneous emission** of light following the absorption of light, shown in Figure 2.6. If a photon with above-bandgap energy is incident on semi-

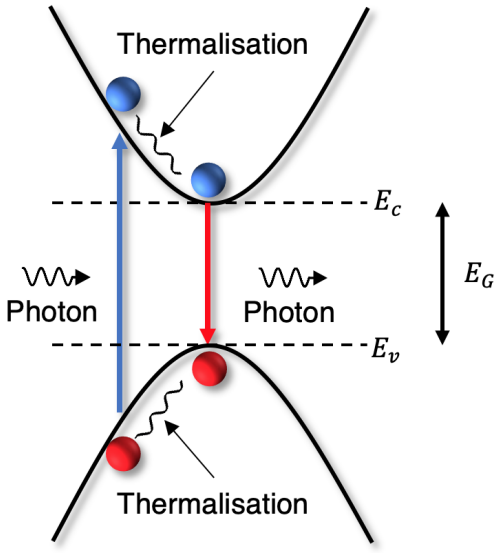

Figure 2.6: Principle of photoluminescence. A photon is absorbed and the energy is transferred to an electron. The electron transitions to the conduction band and thermalises to the band edge via phonon emission. The electron–hole pair recombines and emits a photon.

conductor, the photon can be 'absorbed' and the energy is transferred to an electron which transitions from the valence band to the conduction band. This process forms a free electron–hole pair, which may then form an exciton, depending on the material and conditions. The electron will transition to a state at some energy above the conduction band edge (E_c), depending on the energy difference, ΔE between the absorbed photon energy, E_{ph} and the bandgap energy, E_G ($\Delta E = E_{ph} - E_G$). The electron at the energy $E_c + \Delta E$ will then transition to a state close to the band-edge (depending on the occupancy of states), transferring the additional energy ΔE to phonons via a process called **thermalisation**. The same process occurs with the hole in the valence band, and hence the thermalisation energy ΔE is actually split between the free electron and hole. The electron at the band edge may then recombine radiatively with a hole to emit a photon of lower energy than the one absorbed. If the electron–hole pair instead formed

an exciton, the principle is still the same, except instead of thermalising to the band edges, they form an exciton state with energy less than E_G before recombining.

The spectral intensity of the photoluminescence for a direct-bandgap semiconductor, with a joint density of states given by $\sqrt{(E_{\mathrm{ph}} - E_{\mathrm{G}})}$ is given by [49],

$$I_{\mathrm{PL}}(E_{\mathrm{ph}}) \propto \sqrt{(E_{\mathrm{ph}} - E_{\mathrm{G}})} e^{-(E_{\mathrm{ph}} - E_{\mathrm{G}})/(k_{\mathrm{B}}T)} \tag{2.10}$$

for $E_{\mathrm{ph}} > E_{\mathrm{G}}$, where E_{ph} is the emitted photon energy. However, a Gaussian distribution is often used as a method to characterise the linewidth of the transition.

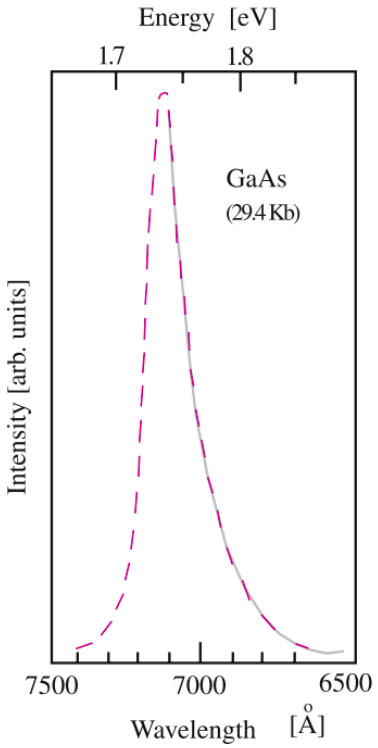

Figure 2.7: PL spectrum of GaAs due to a band-to-band transition. PL spectrum of GaAs following a band-to-band transition (dashed line), measured at room temperature and at 29.4 kbar. The solid curve is a plot of 2.10 with $T = 373$ K [49].

2.2.3 Shibata Model

For any semiconductor, the intensity of photoluminescence will vary with the excitation intensity. For direct bandgap semiconductors, Schmidt [52] and Shibata [53] describe

a model for the dependence of photoluminescence on excitation intensity. The model considers various possible transitions between different states, outlined in Figure 2.8 and

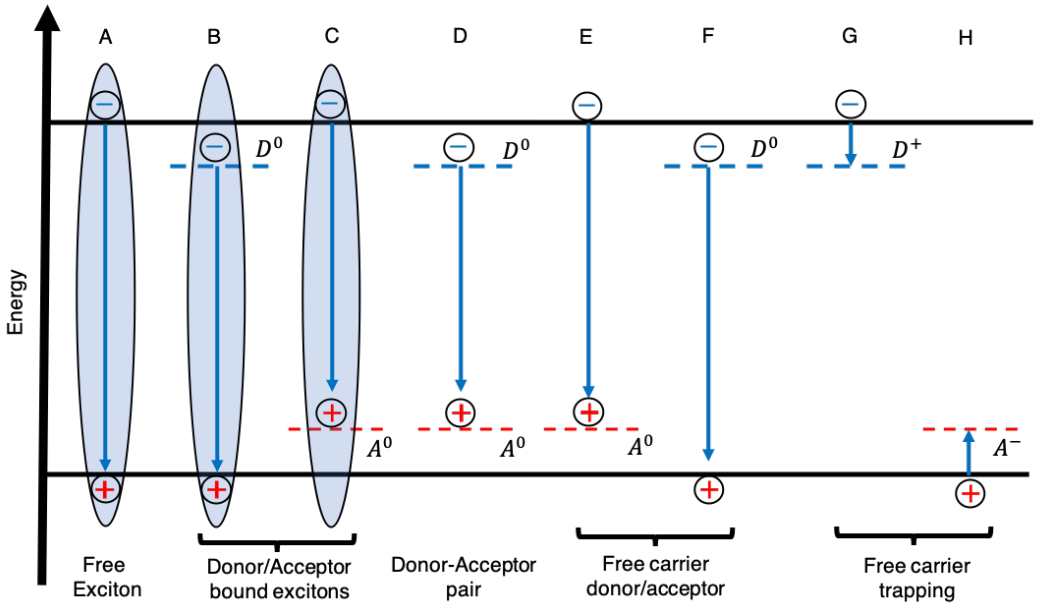

Figure 2.8: Recombination transitions affecting photoluminescence intensity. The various forms of recombination that effect the excitation intensity dependence of photoluminescence in direct-bandgap semiconductors, considered in the model by Schmidt. Recreated from ref [52].

uses the following set of coupled rate equations:

$$\frac{dn}{dt} = iL - an^2 - gn\left(N_D - N_{D^0}\right) - enN_{A^0}, \tag{2.11}$$

$$\frac{dn_{\mathrm{FE}}}{dt} = an^2 + jL - \left[\frac{1}{\tau_{\mathrm{FE}}} + \frac{1}{\tau_{\mathrm{FE}}^{\mathrm{nr}}}\right] n_{\mathrm{FE}} - bn_{\mathrm{FE}}N_{D^0} - cn_{\mathrm{FE}}N_{A^0}, \tag{2.12}$$

$$\frac{dn_{DX}}{dt} = bn_{\mathrm{FE}}N_{D^0} - \left[\frac{1}{\tau_{DX}} + \frac{1}{\tau_{DX}^{\mathrm{nr}}}\right] n_{DX}, \tag{2.13}$$

$$\frac{dn_{AX}}{dt} = cn_{\mathrm{FE}}N_{A^0} - \left[\frac{1}{\tau_{AX}} + \frac{1}{\tau_{AX}^{\mathrm{nr}}}\right] n_{AX}, \tag{2.14}$$

$$\frac{dN_{A^0}}{dt} = h\left(N_A - N_{A^0}\right)n + i\left(N_A - N_{A^0}\right)L - cn_{\mathrm{FE}}N_{A^0} + \left[\frac{1}{\tau_{AX}} + \frac{1}{\tau_{AX}^{\mathrm{nr}}}\right] n_{AX} - dN_{D^0}N_{A^0}, \tag{2.15}$$

$$\frac{dN_{D^0}}{dt} = g\left(N_D - N_{D^0}\right)n - kN_{D^0}L - bn_{\mathrm{FE}}N_{D^0} + \left(\frac{1}{\tau_{DX}} + \frac{1}{\tau_{DX}^{\mathrm{nr}}}\right) n_{DX} - dN_{D^0}N_{A^0} - fN_{D^0}n. \tag{2.16}$$

In these equations, N_D and N_A are the total concentrations of donor and acceptor states, N_D^0 and N_A^0 are the concentration of neutral (occupied) donors and acceptors, τ_{FE} and $\tau_{\mathrm{FE}}^{\mathrm{nr}}$ are the radiative and non-radiative recombination rates for free excitons, $\tau_{DX}, \tau_{DX}^{\mathrm{nr}}, \tau_{AX}, \tau_{AX}^{\mathrm{nr}}$ are the radiative and non-radiative rates for donor- and acceptor-bound excitons, n_{FE}, n_{DX}, and n_{AX} are the concentration of free and bound excitons, and L is the excitation intensity. The coefficients a–h represent the strength of the transitions shown in Figure 2.8, i is the strength of the non-resonant excitation transition, j is the strength of the resonant excitation transition (free-exciton generation)

Upon analysis of equations 2.11–2.16, it is found that the excitation intensity L relates to the observed photoluminescence intensity I with a power law given by $I \propto L^x$, where x depends on the nature of the recombination. Providing the excitation has $E_{\mathrm{ph}} > E_{\mathrm{G}}$ (non-resonant excitation), $x = 1$–2 is indicative of free- and bound- exciton recombination, whereas $x \leq 1$ corresponds to trap-assisted recombination (see section 2.3.2). Under resonant excitation ($E_{\mathrm{ph}} \approx E_{\mathrm{G}}$), the coefficient x for free-exciton emission becomes equal to 1.

2.3 General Principles of Photovoltaics

The photovoltaic effect is a process that converts light energy directly to electrical energy. This can be understood from the perspective of the quantum theory of light, where photons are absorbed by electrons in their ground state. The photon energy is transferred to excite electrons to higher energy states, in which they are mobile. In order to make use of this energy, the electron must be extracted while it is still in the excited state, before it relaxes to the ground state and loses its energy gained from the photon. Since the main application of photovoltaic devices is converting sunlight energy to electricity, they are often referred to as solar cells. The key group of materials for solar cells are semiconductors, as with many electronic devices. There are many reasons why semiconductors are used, as discussed in the previous chapter. To form a photovoltaic device, usually several layers of semiconductor material are used. They can be the same material stacked adjacently (**homojunction**), often with different Fermi-energy levels

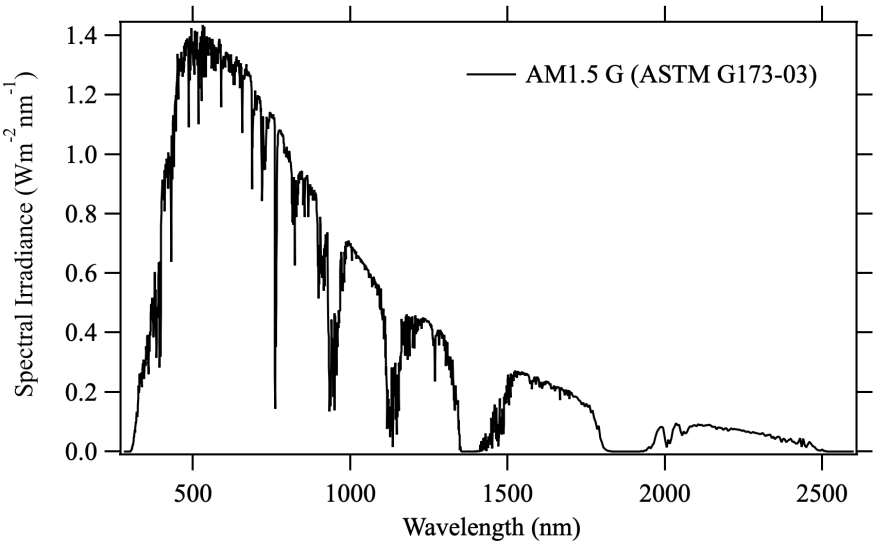

Figure 2.9: The AM1.5 global solar spectrum.

due to doping or they can be two different semiconductor materials (**heterojunction**). A solar cell is a device that can absorb photons and ultimately separate free electrons and holes so they can be used in an external electrical circuit. There may be intermediate steps involved, which are discussed in subsequent sections. Solar cells can be connected together in arrays to form solar cell modules.

A solar cell generates a voltage across its terminals and will provide a flow of current providing that it is connected in a circuit with a non-infinite load resistance. The voltage developed when the terminals are isolated (or connected to an infinite load resistance) is called the **open-circuit voltage**, V_{oc}. The current flowing when the terminals are connected is called the **short-circuit current**, I_{sc}, although it is common to refer to the short-circuit current density J_{sc} instead since this is independent of the area of the solar cell (which can vary greatly between devices). The short-circuit current generated by a solar cell is directly proportional to the intensity of light absorbed by it. In the dark a solar cell behaves like a regular diode, permitting current flow in only one direction (forward-bias) with a non-linear resistive response. A very small current flows when the polarity is reversed (reverse-bias), called the reverse saturation current I_0 (or reverse saturation current-density J_0). The additional photocurrent provided by absorbed photons acts to shift the diode response by an amount equal to the photocurrent. The

current density for an ideal diode in the dark as a function of voltage V is given by

$$J_{\text{dark}}(V) = J_0(e^{qV/k_{\text{B}}T} - 1) \tag{2.17}$$

where q is the elementary charge, k_{B} is the Boltzmann constant and T is the temperature in the Kelvin scale. If we take the photocurrent to be positive, the net current density can be found by summing the dark current and the photocurrent densities,

$$J(V) = J_{\text{sc}}(V) - J_{\text{dark}}\,, \tag{2.18}$$

which after inserting 2.17 becomes

$$J(V) = J_{\text{sc}}(V) - J_0(e^{qv/k_{\text{B}}T} - 1)\,. \tag{2.19}$$

The open-circuit voltage V_{oc} occurs when the net current is zero, and hence is given by

$$V_{\text{oc}} = \frac{k_{\text{B}}T}{q}\ln\left(\frac{J_{\text{sc}}}{J_0} + 1\right) \tag{2.20}$$

from 2.4. The current–voltage curve for a solar cell is shown in Figure 2.10. The short-circuit current acts to shift the curve downwards when the solar cell is illuminated.

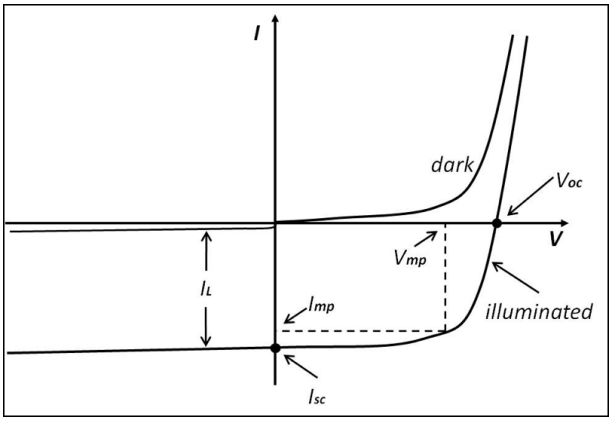

Figure 2.10: Current–voltage behaviour of a solar cell. A solar cell behaves as a regular diode when not illuminated. When the cell is illuminated, the diode response is translated downwards by an amount equivalent to the short-circuit photocurrent. This amount is proportional to the incident light intensity.

A solar cell can therefore be modelled electrically as a diode in parallel with a current generator (Figure 2.11). With the diode effectively providing the photovoltage, acting as a potential divider with the load.

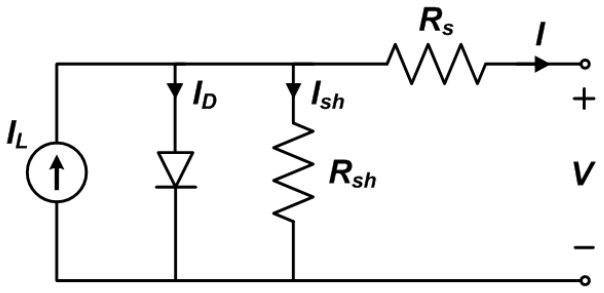

Figure 2.11: Shockley equivalent circuit for a solar cell. A solar cell can be effectively modelled with a current source in parallel with a diode. The series and shunt resistances can be modelled as lumped elements.

The **power-conversion efficiency** of a solar cell is given by the ratio of the maximum electrical power produced by the solar cell and the power of the incident sunlight (or the power densities):

$$\mathrm{PCE} = \frac{V_{\mathrm{max}} J_{\mathrm{max}}}{P_{\mathrm{inc}}} \tag{2.21}$$

V_{max} and J_{max} are the voltage and current density at the maximum power point respectively and P_{inc} is the incident power per unit area of the sunlight. Ideally, a solar cell will have values of V_{max} and J_{max} that are identical to V_{oc} and J_{sc} but in practice this is impossible. The ratio

$$\mathrm{FF} = \frac{V_{\mathrm{max}} J_{\mathrm{max}}}{V_{\mathrm{oc}} J_{\mathrm{sc}}} \tag{2.22}$$

is called the **fill factor**. A fill factor of 100% would result in a square-shaped J–V curve. The four values V_{oc}, J_{sc}, FF and PCE are the main figures of merit for solar cells.

Another important metric for PV devices is **external quantum efficiency** (EQE), which gives the photon-to-electron conversion ratio as a function of photon energy for light incident to the device by,

$$\mathrm{EQE} = \frac{electrons/second}{photons/second} = \frac{I_{\mathrm{sc}}/e}{P_{\mathrm{inc}}/h\nu}, \tag{2.23}$$

where I_{sc} is the photocurrent, P_{inc} is the optical power incident on the device and $h\nu$ is the photon energy. An EQE measurement system uses monochromatic light at a given intensity and measures the short-circuit current as a function of photon energy. The theoretical short-circuit current I_{sc}, for a device under AM1.5G illumination can be calculated from the EQE spectrum using,

$$I_{sc} = q \int \phi(E)\mathrm{EQE}(E)dE, \tag{2.24}$$

where $\phi(E)$ is the photon flux spectrum (Figure 2.9) as a function of photon energy E.

Real solar cells have both resistance to current flow through the device and also leakage currents between the contacts. The first can be modelled using a non-zero **series resistance** as a lumped component in the equivalent circuit and the second a finite **shunt resistance**. The main effect caused by these resistances is a reduction of the fill factor. The series resistance arises from the internal resistance of the materials in the device, including the contacts. The extra resistance produced by the non-ideal contact between any layer also contributes to the series resistance. In the extreme case of high series resistance, the short-circuit current is reduced, whereas it does not affect the open-circuit voltage. The shunt resistance should be ideally infinite, however current may flow between contacts either directly though leakage pathways in the device or around the device layers. The extreme case of low shunt resistance lowers the open-circuit voltage but does not affect the current at short-circuit conditions. Figure 2.11 shows the equivalent circuit with series and shunt resistances added. The diode equation becomes

$$J(V) = J_{sc}(V) - J_0(e^{q(v+JAR_s)/k_BT} - 1) - \frac{V + JAR_s}{R_p}, \tag{2.25}$$

where R_s is the series resistance, R_p is the shunt resistance and A is the active area of the solar cell.

The maximum efficiency of a solar cell is dependent on the bandgap of its absorbing material, given by the **Shockley–Queisser limit** (Figure 2.12) [54]. The optimum bandgap is 1.4 eV and results in a theoretical maximum PCE (maximum PCE of a single-material active-layer device) of 33% for the solar spectrum [55].

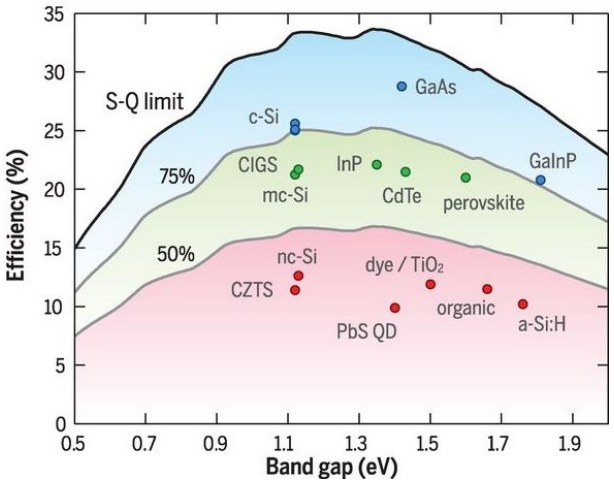

Figure 2.12: Shockley–Queisser limit. The theoretical efficiency limit of PV technologies as a function of material bandgap.

2.3.1 Generation

Charge generation is crucial to photovoltaics and is the main purpose of a device. Generation in a semiconductor is a process of electronic excitation, producing a free-carrier pair or exciton. Recombination is the relaxation process, where the energy is transferred from the excited state to a photon (radiative recombination), phonon (non-radiative recombination) or the kinetic energy of another charge carrier (Auger recombination), as discussed in the following subsection. The input energy of generation also comes from these processes. The most important form of generation for solar cells is of course where the input energy is from a photon (photogeneration). Providing that the photon energy is above the bandgap of the material, an electron can be excited from the valence band to the conduction band. Alternative processes include excitation from the valence band to a localised state within the bandgap or from a localised state to the conduction band. The first produces only a mobile hole and the latter only a mobile electron.

The amount of charge generation will depend on the incident light intensity and spectrum, the bandgap energy of the material and temperature (particularly for indirect bandgap semiconductors). The amount of energy absorbed is not important for generation but instead the number of excitation events. Photons with above-bandgap energy may transfer the surplus energy to the electron but will quickly be lost. The electron relaxes to the conduction band edge via a process known as thermalisation. The electron

loses its extra energy (kinetic energy) by undergoing multiple collisions with the lattice, hence transferring energy to phonons. This process occurs on the order of picoseconds [55], meaning that the energy is lost before the carrier can be extracted. There is much research devoted to extracting the energy from electrons before thermalisation; solar cells with this capability are known as 'hot carrier' solar cells.

2.3.2 Recombination

Charge-carrier recombination in semiconductors is an important factor for electronic devices. Recombination in solar cells is an essential process as photogenerated electrons that do work in an electrical circuit containing a solar cell will at some time then recombine with holes in the device, for example in a hole-transporting layer. However, recombination that occurs before carriers are extracted may limit the amount of charge and hence current that can be extracted from the absorbing material. The most pronounced effect of recombination is on the voltage produced by a solar cell.

The recombination of charges n in a semiconductor can be given by the equation,

$$\frac{\mathrm{d}n}{\mathrm{d}t} = G - R(n), \quad R(n) = k_1 n + k_2 n^2 + k_3 n^3. \tag{2.26}$$

Here, G is the generation rate, $R(n)$ is the recombination rate, n is the number of mobile charge carriers and k_1, k_2, and k_3 represent components of the recombination rate associated with three different processes. k_1 is the rate associated with the recombination of excitons or recombination that is assisted by a trap state within the energy gap. This is commonly referred to as **monomolecular**, **trap-assisted** or **Shockley–Read–Hall** recombination. This mechanism is a form of **non-radiative recombination** in a semiconductor, and may also result in further recombination of the trapped carrier with carriers in the band edges. k_2 is related to the recombination of electrons and holes, which is often radiative recombination resulting from band-to-band transitions. This is often referred to as **electron–hole**, **band-to-band** or **bimolecular** recombination, since it is dependent on both the electron and hole densities $n_e n_h = n^2$. The last process, related to k_3 involves the interaction of three carriers. An electron may

recombine with a hole and transfer kinetic energy (and momentum) to a third carrier, where further phonon emission or absorption may occur. This is referred to as **Auger** or **trimolecular** recombination [56]. It is strongly dependent on the charge carrier density and usually not observed at low levels of excitation. Figure 2.13 shows the different semiconductor recombination processes. The recombination rate is of course linked to

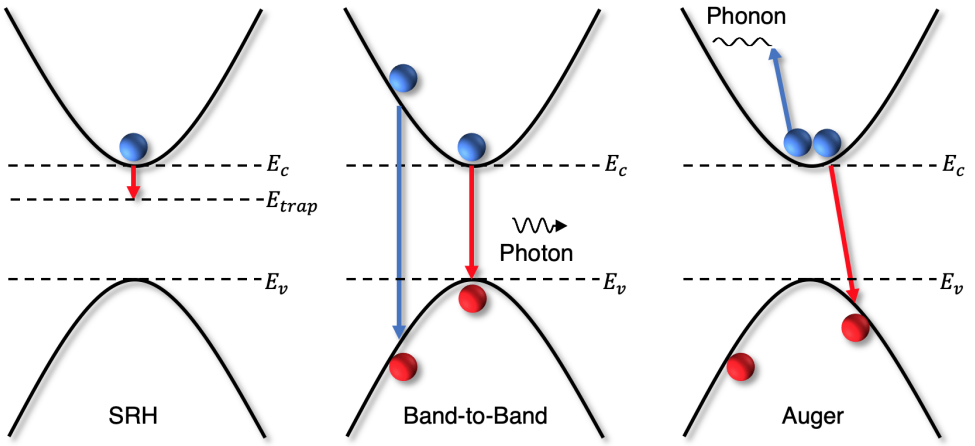

Figure 2.13: Schematic diagram of recombination processes in a semiconductor. Diagram showing trap-assisted (SRH), band-to-band and Auger recombination. Adapted from Ref. [57].

the diffusion of charges and the charge-carrier diffusion length, $L_D(n)$ depends on the global recombination rate, $R(n)$ directly as,

$$L_D(n) = \sqrt{\frac{\mu k_B T}{R(n) e}}. \tag{2.27}$$

Solar cells operate in relatively low levels of charge-carrier concentrations $\sim$ (10^{15}–10^{16} cm^3 [15]); hence, k_1 has the largest impact on $R(n)$ in solar cells. Impurity species in the material or crystal defects can introduce energy states within the bandgap that trap carriers. Therefore, a large effort is usually made to improve material quality, thus reducing the density of defects and hence trap states.

Radiative recombination in semiconductors is an unavoidable process and is not indicative of an unsuitable photovoltaic material. Counter intuitively, an ideal solar cell material should radiate all of the light incident on it provided that it is not connected to an external circuit (open-circuit condition) [58]. The reason for this is that radiative

band-to-band recombination is the reverse process of mobile charge-carrier generation. Consideration of this fact is crucial for obtaining the highest possible V_{OC} from a solar cell material in the limit of a perfect (defect-free) material. The V_{OC} relates to the external luminescence efficiency, η_{ext} (ratio of photons emitted to photons incident, or carriers injected), by the equation,

$$qV_{OC} = qV_{OC-Ideal} - kT\left|\ln \eta_{ext}\right|, \tag{2.28}$$

where $V_{OC-Ideal}$ is the ideal V_{OC} and T is the temperature [59, 60]. If a solar cell material is isolated from any electrodes, energy from photoexcited electrons should ideally be transferred to photons. Any energy not re-radiated must have been transferred via non-radiative decay channels and hence lost. Therefore a material with high photoluminescence efficiency is desirable since it indicates a lack of non-radiative recombination.

In photoluminescence measurements, an equal number of electrons and holes are excited (as opposed to electroluminescence, where an extra minority carrier is injected). Since the intrinsic carrier concentrations are typically low, it is usually easy to optically excite carriers so that the photoexcited species greatly outnumber the intrinsic carriers. In addition to radiative recombination processes, the photoexcited charge carriers can also recombine non-radiatively with a rate of $1/\tau_{nonrad}$, where the energy is dissipated as heat via electron–phonon coupling. The total decay rate ($1/\tau_{tot}$) of the photoexcited population is given by

$$\frac{1}{\tau_{tot}} = \frac{1}{\tau_{rad}} + \frac{1}{\tau_{nonrad}} \tag{2.29}$$

where $1/\tau_{rad}$ is the radiative recombination rate.

2.3.3 Junctions

Photovoltaic energy conversion requires charge generation, separation and transport. Junctions between materials with different electrical properties facilitate charge separation in solar cells. Junctions provide the driving force to separate charges and can do so with various different mechanisms. Some junctions utilise a built-in electric field that is established in equilibrium due to differences in material composition. Effective

fields can be produced by differences in work function, bandgap energy, electron affinity and effective band density of states. An example is the p–n junction, where materials with different carrier densities for electrons and holes are brought together, producing a depletion (or space-charge) region. In this region, there is a built-in potential gradient (net electric field) in equilibrium which provides the driving force. However, although the p–n junction is the classic model for diodes such as solar cells, they are not required for photovoltaic action. Instead, materials that prevent the transfer of one type of charge carrier and allow the flow of the other can be used on either side of the absorber material, as shown in Figure 2.14. This produces a gradient in carrier density of a given type

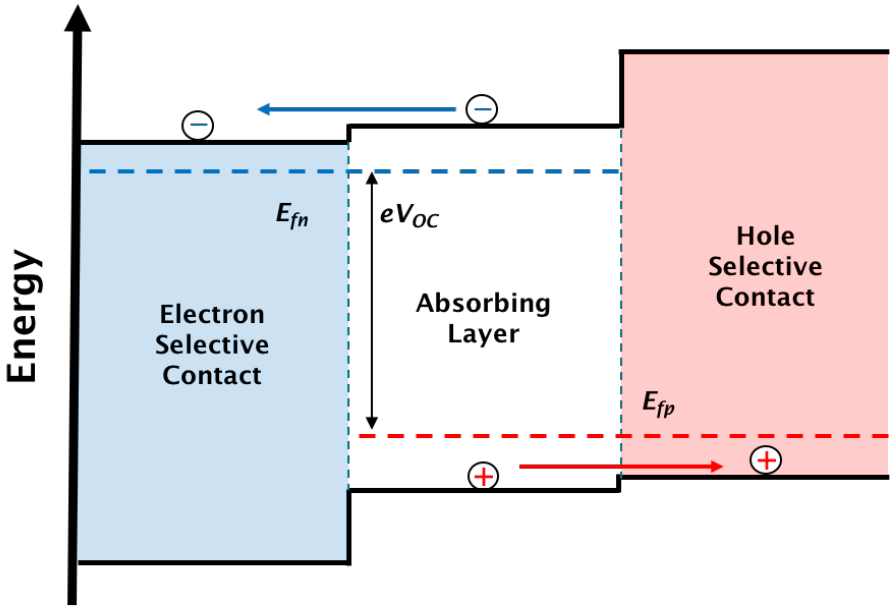

Figure 2.14: Generic solar cell architecture. Diagram of energy levels in an ideal solar cell employing two charge extraction layers.

(electrons or holes) at the interface and can be considered as electron or hole sinks. In this case, a **diffusion** current is established.

Solar cells employing organic materials require that the excitons formed are to be dissociated for charges to do work in an external circuit before recombining. Due to the excitons having large binding energies and small diffusion lengths, organic solar cells are confined to architectures where the average distance from a heterojunction is small in the active layers. Another perspective is that dissociation must occur as early as

possible following photo-generation to prevent recombination. The most successful architecture that well obeys this notion is the bulk heterojunction. Since these materials have non-crystalline or molecularly crystalline natures, charge transport occurs via hopping between molecules across a potential-energy landscape. This is typically achieved using a heterojunction where there is a large difference between the work function of the two materials.

2.4 Low–Dimensional Semiconductors

Materials with one or more dimensions less than 100 nm are often referred to as nanomaterials. Dimensions are often however 1–10 nm, and hence smaller than the Bohr radius of electrons within the material. This section introduces some basic concepts of low-dimensional semiconductor materials, with the focus on zero-dimensional (all dimensions less than 100 nm) such as spherical semiconductor nanocrystals. Such nanostructures are referred to as quantum dots (QDs). They may exist a features on a larger substrate, achieved by etching or be isolated completely by coating the surface with molecules known as ligands or surfactants. The latter are known as colloidal quantum dots, since they are use to form colloids of QDs in a liquid solution. This makes QDs compatible with 'solution processing' techniques; a facile approach to semiconductor device fabrication involving the deposition of solid materials from liquids.

2.4.1 Quantum Confinement in Semiconductor Nanocrystals

The confinement of excitons in semiconductor nanocrystals can be understood from first considering the one-dimensional case. Electron confinement in one dimension is analogous to the the infinite square-potential (particle in a box) problem of quantum mechanics, shown in Figure 2.15. Although this better represents the quantum confinement observed in quantum wells (where electrons are confined to a 2D plane) rather than quantum dots, it can be extended to all dimensions. The particle in a box model involves a potential that is zero-valued between two walls and infinite outside them. The time-independent schrödinger equation is given by,

$$-\frac{2m}{\hbar^2}\nabla^2\psi + V\psi = E\psi, \tag{2.30}$$

which for one dimension is

$$-\frac{2m}{\hbar^2}\frac{\partial\psi(x)}{\partial x}\psi + V(x)\psi(x) = E\psi(x), \tag{2.31}$$

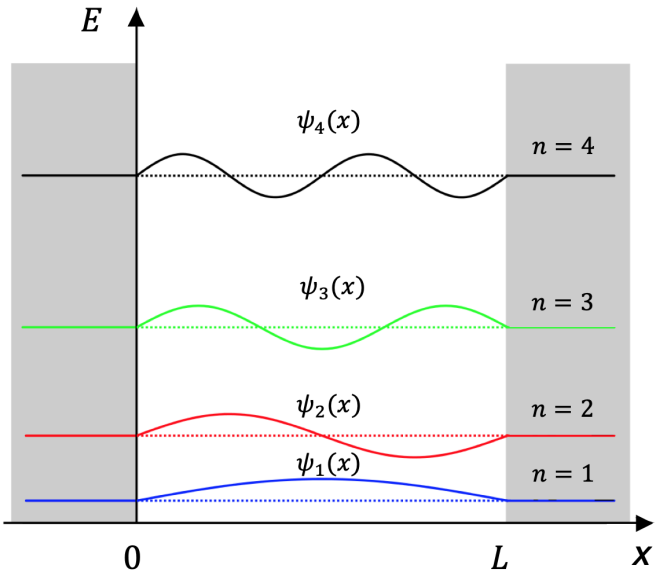

Figure 2.15: Schematic of the particle in a box.

where m is the mass of the particle, $\psi(x)$ is the wavefunction of the particle, $\hbar$ is the reduced Planck constant, $V(x)$ is the potential and E is the energy of the particle. The solution to this problem yields

$$E = \frac{n^2\pi^2\hbar^2}{2mL^2}, \tag{2.32}$$

for the allowed energy eigenvalues, where n is an integer corresponding to the energy state and L is width of the potential well. The result shows that the energy states are proportional to $1/L^2$ and thus by varying the width of the quantum well, the electronic energy states can be tuned. Note that additionally these states no longer form continuous bands as in bulk semiconductors, but instead form discrete levels analogous to individual atoms. Such quantum wells can be achieved by semiconductor heterostructures, with a common example being a thin layer of GaAs sandwiched between the larger-bandgap $Al_xGa_{1-x}As$. The result is similar when extended to electron confinement in three dimensions which can be achieved by fabricating semiconductor nanosphere cores surrounded by a shell of a different semiconductor. Such QDs are called core-shell QDs. Alternatively the core can be used as a stand-alone QD, with the potential barrier provided by the vacuum energy (core-type QDs).

The dependence of electronic state energies with QD radius allows for tuning of the optical absorption emission spectrum. The discretisation of the energy levels in QDs

also causes the density of states to form Dirac-like functions.

Chapter 3

Review of Perovskite Solar Cells

3.1 Properties of Bulk Perovskite Semiconductors

3.1.1 Structure

Perovskite is the name given to any crystalline material with the general structure of calcium titanate ($CaTiO_3$). The most interesting compounds for optoelectronic applications have been lead-halide perovskites that have the aristotype framework of a cubic structure in the space group $Pm\bar{3}m$ and a general formula of ABX_3. In 1926 Goldschmidt proposed that a solid only forms a perovskite structure if the ionic radii R_A, R_B and R_X conform to $R_A + R_X = t\sqrt{2}(R_B + R_X)$, where t is the tolerance factor between 0.8–1 [61]. A is a large cation such as methylammonium 'MA' ($CH_3NH_3{}^+$), formamidinium 'FA' ($CH(NH_2)_2{}^+$) or Cs^+, B is $Pb_2{}^+$ or another post-transition metal cation, and X is the halide such as I^-, Cl^- or Br^-. Methylammonium lead iodide (MAPI), with the formula $CH_3NH_3PbI_3$ has been the most ubiquitously reported perovskite material for solar cell applications.

In 2009, the first report (peer-reviewed journal article) of a solar cell with MAPI as the active layer was published by Kojima *et al.* [11] and subsequently the power conversion efficiency (PCE) of perovskite solar cells has improved with an unprecedented rate, with the record now over 25 % PCE [12]. Perovskite materials typically adopt the psuedo-cubic tetragonal and orthorhombic phases but can also exist in the higher-symmetry

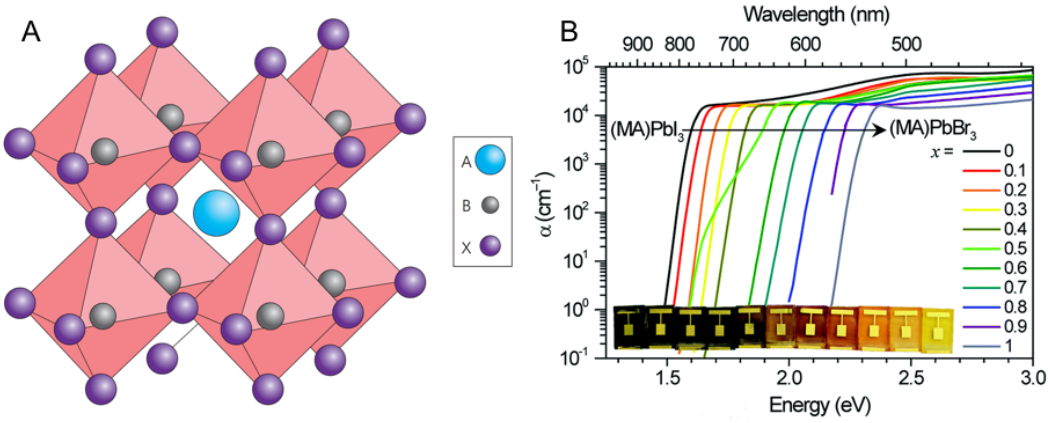

Figure 3.1: Perovskite ABX_3 structure and absorption spectra. (A) Cubic perovskite structure. **(B)** Absorption coefficient spectra for perovskite films with varying iodide–bromide ratios. Figures taken from Refs. [62] and [63].

cubic ($Pm\bar{3}m$) phase in certain conditions. For example MAPI adopts the orthorhombic ($pnma$) phase below $\sim$ 160 K, the tetragonal ($I4/mcm$) phase between $\sim 160 - 315$ K and the cubic phase above $\sim$ 315 K [64–66]. Coexistence of phases is also likely, for example spectroscopic evidence is found simultaneously of both the tetragonal and orthorhombic phases at lower temperatures [67–69]. It has also been proposed that the continuous phase transition from the tetragonal to orthorhombic phase in MAPI is not possible [64].

3.1.2 Photophysics and Charge Transport

Perovskites exhibit many desirable photophysical properties, such as an easily tuned bandgap energy close to the ideal value according to Shockley–Quiesser theory and a high extinction coefficient for photons with above-bandgap energy. They also have excellent electrical properties such as high charge carrier mobilities (> 30 cm^2(Vs)$^{-1}$), long lifetimes [15] and long diffusion lengths (> 1 µm) [17]. The primary photoexcited species in perovskites at typical operating conditions for PV is generally agreed to be free charge carriers [69–72] allowing for successful use of perovskites for the planar solar cell architecture.

A vast array of methods have been employed to investigate the photophysics of perovskite materials, including transient/time-resolved absorption spectroscopy (TAS) [73, 74],

time-resolved photoluminescence (TRPL) [75, 76], time-resolved infrared spectroscopy [77], terahertz and microwave spectroscopy [15, 78], and many other specialised techniques. Despite these considerations, the underlying physics of perovskite materials are not well understood. Specific examples include the contributions of excitons to the photoexcited states at different temperatures, the nature of the band structure, transitions during generation and recombination processes, the effect of trap states and defects, and the understanding of device operating principles. Studies of these subjects are complicated by the sensitivity of the material properties to fabrication methods and compositions used. The fact that there are so many reported routes to perovskite fabrication exacerbates this issue, although conversely shows the versatility of the material for use in photovoltaics.

3.1.2.1 Charge Carriers

Many studies have been carried out from which the exciton binding energy of perovskite materials can be inferred, with values ranging from 2 meV to >60 meV [72, 79–86] at room temperature for MAPI. The reports of intermediate values for the exciton binding energy describe a picture of photogeneration of both excitons and free carriers at room temperature, with a ratio of $\sim 1 : 10$ [70]. Miyata *et al.* reported a value of 16 meV at low temperature, measured directly via high-field magneto-optical absorption spectroscopy [71]. In the same study, the effective mass of MAPI was determined to be $m^* = 0.104 \pm 0.003 m_e$ from magnetic-field-dependent optical transitions [71], in agreement with previous theoretical work [84]. This confirmed that the exciton binding energy is well below kT at room temperature and hence free carriers should be generated upon photoexcitation. However, many reports that have determined E_B using other spectroscopic techniques have concluded the value to be larger, indicating the presence of excitons at room temperature. The large discrepancy in these values remains yet to be fully explained. He *et al.* argue that most spectroscopy studies have been carried out with pump fluences much larger than those found in the typical operating regime for solar cells and their results suggest that at lower fluences, the PL is dominated by the recombination of weakly localised excitons [87].

One method of determining the origin of PL in semiconductors is to analyse the PL behaviour as a function of excitation fluence. According to a model introduced by Shibata *et al.*, based on work by Schmidt *et al.*, the near band–edge PL following a power law $I \propto L^x$, where I is the PL intensity, L is the excitation fluence and x is the power index, can be well described by free exciton, bound exciton, free-to-bound exciton, donor–acceptor pair or free electron and hole transitions, depending on the value of x [52, 53] (see section 2.2.3).

Many studies have used spectroscopy techniques using terahertz (THz) and microwave (MW) radiation for perovskite materials. These techniques specifically involve interaction with free carriers and thus the presence of free carriers has been observed by Drude-like terahertz photoconductivity spectra [15, 75] and MW photoconductance [16, 78, 80] in perovskites at room temperature. Despite this, at temperatures lower than $\sim$ 200 K, a peak in the absorption spectrum at an energy lower than the bandgap has been identified as an exciton transition [72, 88, 89]. The explanation for this is a temperature-dependent dielectric constant that reduces the Coulombic interaction between charges. Evidence has shown that the collective rotational motion of organic cations activated above a certain temperature is the cause of this Coulombic screening of exciton transitions at higher temperatures [81, 88, 90, 91]. Despite an excitonic feature and a large absorption edge blueshift (100 meV) at lower temperatures, it is still found that the low-temperature PL is centred at the absorption onset of the room temperature (tetragonal) phase [75, 92]. Several theories for this have been reported, including the consideration that small regions of the tetragonal phase remain at lower temperatures and most photogenerated charges accumulate in or are rapidly transferred to these states due to the lower energy conduction band of the tetragonal phase inclusions [69, 92].

3.1.2.2 Bandstructure and Rashba Splitting

Density functional theory calculations show that in MAPI, the valence band maxima are comprised of $6s$ lead and $5p$ iodine orbitals, and the conduction band minima mainly $6p$ lead orbitals [93]. The organic component (methylammonium in MAPI) does not directly contribute to the electronic band structure but is important in maintaining the

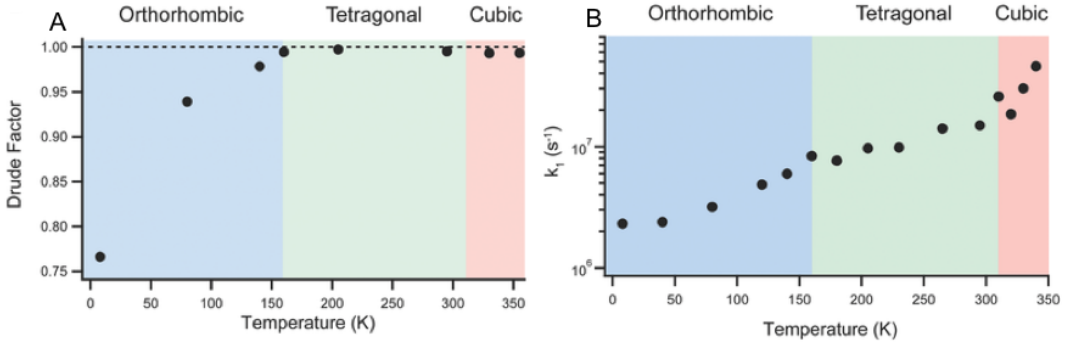

Figure 3.2: Drude factor and monomolecular recombination rate as a function of temperature. (A) Drude factor as a function of temperature calculated from THz transmission data. Values of 1 indicate ideal Drude behaviour. **(B)** First-order (monomolecular) recombination rate as a function of temperature obtained from fitting TRPL data. Figures taken from Ref. [75].

crystal structure [94]. MA possesses a static dipole moment and is free to rotate within the unit cell [95, 96]. This is thought to cause the dielectric constant to be dependent on temperature and electric field frequency, as discussed above [83, 88].

It is usually assumed that perovskites such as MAPI are direct-bandgap semiconductors [97], demonstrating high absorption coefficients and light emission typical in the presence of a direct bandgap. However, one property that requires explanation for perovskite materials is their slow charge recombination properties, typical of an indirect bandgap transition via phonon emission [98]. Another surprising observation is that the radiative recombination rate increases with temperature, suggesting that it is a thermally activated process [78], whereas the opposite trend is found with direct-bandgap semiconductors such as GaAs [99].

Many models have been proposed that describe the slow recombination in terms of trap-assisted recombination (direct-bandgap) [76, 100, 101]. However, slow recombination is also found in perovskite single crystals where the trap-state density is very low, suggesting that trap-assisted recombination may not be the prevailing mechanism contributing to long recombination lifetimes [102]. From investigations to explain this paradox, theoretical evidence has been found that perovskites may actually possess an indirect–bandgap and that slow recombination is facilitated via an indirect transition [91, 103–106]. This has been attributed to the collective orientations of organic cations [91] and due to the effect Pb spin-orbit coupling (SOC) [103, 105].

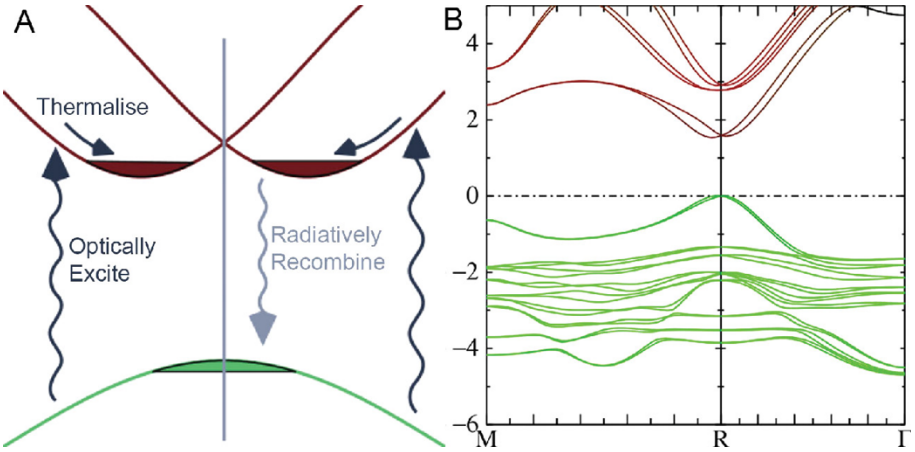

Figure 3.3: Calculated electronic band structure of MAPI. (A) Schematic of dispersion, showing interpretation of absorption and recombination processes. The conduction bands are split around the R-point. Photogenerated electron–hole pairs, relax to their respective band edges forming a quasi-equilibrium distribution of carriers. The excess electrons and hole populations can recombine radiatively without phonon assistance if the transitions are vertical, as shown. **(B)** QSGW band structure for a section of the M–R–Γ lines. Splitting of the conduction band is shown centred at R ($E \sim 1.75$ eV). Figures taken from [103].

Figure 3.3 shows the band structure calculated within the framework of the quasiparticle self-consistent GW approximation (QSGW) and proposed recombination mechanism. It is suggested that the slow recombination is inherent due to the split-spin indirect bandgap and therefore not due to trap-assisted recombination alone. Strong local electric fields act on the SOC in the conduction band minimum comprised of the lead $6p$ orbitals, splitting it to a pair of minima [103]. This is referred to the Rashba effect or Rashba splitting. It has been found that the radiative recombination rate increases with excitation fluence [76, 100] which has been previously attributed to trap-assisted recombination effects. However Azarhoosh *et al.* propose that in the spin-split band structure, an increase in excitation fluence results in a larger overlap in the density of states of the CBM and VBM, opening recombination channels that do not require phonon transfer, as shown in Figure 3.3. This provides an interpretation that does not involve trap states as the underpinning mechanism of excitation-dependent recombination dynamics in perovskites, thus bypassing the paradox of a direct-bandgap and slow recombination. Zheng and co-workers developed a tight-binding model for MAPI

in which Rashba splitting results in faster spin-allowed and slow spin-forbidden recombination pathways [104]. The mechanism described by their model allows perovskite materials to behave like direct-bandgap semiconductors on absorption of photons and indirect bandgap semiconductors on radiative emission, as observed experimentally.

Experiments revealing the indirect–bandgap nature of perovskites have also been performed. Here, slow recombination and absorption was identified from shallow states below the conduction band edge. However, when probed with time-resolved microwave conductance these states were revealed to contain highly mobile charges rather than immobilised, trapped charges [78]. It is also found that the second-order recombination (corresponding to radiative recombination between conduction-band electrons and valence-band holes) increases with increasing temperature. Therefore, a band structure is proposed that is comprised of two conduction band minima (one direct, one indirect) as shown in Figure 3.4. The conduction-band minimum is shifted in k-space to the valence-band maximum and hence the radiative recombination of electrons between the two is forbidden. However, as temperature is increased, thermal energy is transferred to the electrons so that may populate the higher-energy direct conduction band minimum. Therefore, radiative recombination becomes more prominent at higher temperatures and an activation energy for the process is calculated to be 47.0 ± 1.2 meV, extracted from the Arrhenius equation [78]. Interestingly, this value is on the same order of magnitude as the calculated energy difference between the two bandgaps.

3.1.2.3 Trap States, Defects and Ambient Effects

The room-temperature photoluminescence spectrum of lead halide perovskites typically has a single peak, showing no low-energy emission from sub-gap trap states. Therefore the trap-assisted recombination in perovskites is a non-radiative process that should be mitigated. At low temperature however, multiple peaks have been observed, with lower energy emission potentially originating from trap-assisted recombination [69]. The influence of trap states and defects on the charge carrier recombination in perovskites is another topic that is widely debated. The density and nature of trap states of perovskite

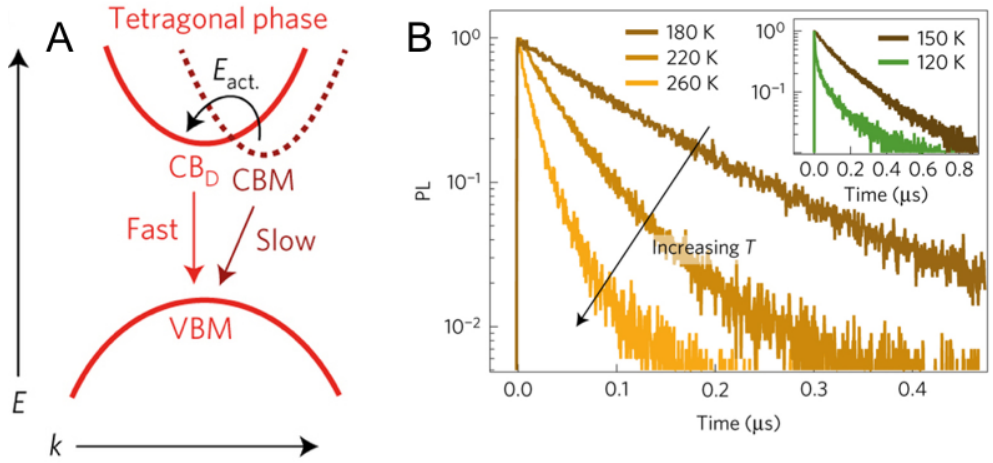

Figure 3.4: Proposed band diagram for MAPI. (A) Schematic of the direct–indirect band structure for MAPI, showing the lower energy minima of the conduction band to be indirect. **(B)** Time-resolved photoluminescence decay for several temperatures. The second-order recombination rate increases as temperature is increased, suggesting that electrons are thermally excited from the non-emissive CBM states to the CB_D band where they can the recombine radiatively. Figures taken from [78].

materials varies largely depending on the fabrication protocol. A wide range of trap-assisted (monomolecular) decay rates have been reported, corresponding to lifetimes on the order of ns to μs (k_1 =1–250 x10^6 s^{-1}) [17, 72, 100, 107–112]. Solution-processed polycrystalline films have been found to have calculated trap state densities between $\sim 10^{15} - 10^{18}$ cm^{-3} [9, 113]. Inferred from measurements of PL intensity, these values are both temperature and excitation dependent, with an order-of-magnitude reduction following light exposure demonstrated by Mosconi and co-workers (photobrightening or photocuring); a phenomenon explained by the suppression of iodine vacancy/interstitial Frenkel pairs [114]. Previous theoretical work suggests that these defects can easily diffuse across a crystal (migration activation energy $\sim$ 0.1 eV) [115]. deQuilettes *et al.* showed that the increase of PL intensity under illumination is caused by an order-of-magnitude reduction in trap-state density, which is correlated to iodine migrating away from the illumination spot [116].

Increases in photoluminescence quantum yield (PLQE) have been linked not only to light irradiation but also the environment in which the sample is kept. Specifically, it has been demonstrated that both the combination of light soaking and exposure to oxygen increases the PLQE over the time scale of hours [117–120]. Motti *et al.* showed

that trap states are induced following light exposure in inert environments (shown by a reduction in PLQE after several minutes following continuous light soaking) and can subsequently be passivated by exposure to oxygen [119]. One explanation proposed for this effect is the formation of superoxide (O_2^-) following the reaction between an absorbed oxygen molecule and a free electron [121]. The O_2^- can passivate defects such as iodine vacancies, resulting in an enhancement of radiative recombination. However, the highly reactive O_2^- has also been attributed to the long term degradation of perovskite materials [122, 123] and therefore utilising these observations as a post-fabrication treatment may be problematic in terms of device stability. Trap state densities have also been found to be spatially non-uniform, with trap state densities spanning two orders of magnitude on a single sample [124].

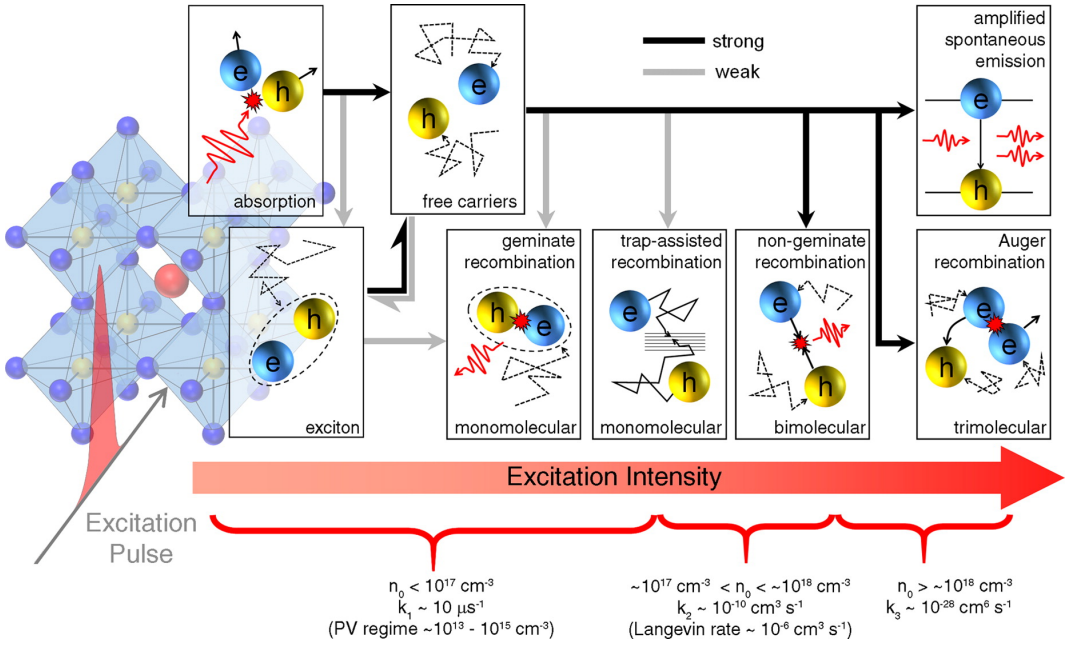

Figure 3.5: Excitation and recombination processes in MAPI. Interpretation of the recombination processes in MAPI for different excitation densities. Recombination rates are also shown. Figure taken from [73]

.

3.2 Photovoltaic Devices

3.2.1 Architectures and Device Performance

The first device architectures were adopted from the field of dye-sensitised solar cells (DSSCs), where typically an organic dye absorbs light and transfers it to a conductive oxide. This effect was discovered in 1968 [125] and the first high-efficiency devices were realised in 1991 based on titanium dioxide (TiO_2) [126]. Perovskite materials were first used in solar cells as a sensitiser for the standard TiO_2 DSSC solar cell architecture [11]. Later it was found that when TiO_2 is replaced with Al_2O_3 scaffold (insulator), device still functioned, hence ambipolar charge transport occurs through perovskite [108, 127, 128]. This allows perovskites to be used in planar solar cell architectures, although the most efficient devices are still based on the mesostructures architecture.

There are now four main architectures used for perovskite solar cells (shown in Figure 3.6): *p–i–n* planar, *n–i–p* planar, *p–i–n* mesostructured, and *n–i–p* mesostructured. The *n–i–p* mesostructured device typically consists of transparent cathode which is usually fluorine-doped tin oxide or FTO, an $\sim$ 70-nm compact ETM layer (typically TiO_2) followed by a 150 to 300 nm thick mesoporous metal oxide (mp-TiO_2 or mp-Al_2O_3) that is penetrated with perovskite material, a 300-nm perovskite active layer on top of this, then a $\sim$ 200 nm thick HTM of 2,2,7,7-tetrakis(N,N-di-p-methoxyphenylamine)-9,9-spirobifluorene (spiro-OMeTAD), and a $\sim$ 100 nm metal anode (Au or Ag).

Devices fabricated with the *n–i–p* structure (ETM deposited first) are often referred to 'standard architecture' devices due to the fact that they were the first to be fabricated, whereas the *p–i–n* devices (HTM deposited first) are referred to as 'inverted architecture' devices. The purpose of the mesoscopic layer is to provide a scaffold and is thought to enhance charge collection by increasing surface area of contact between perovskite and the ETM, and also increasing light absorption by scattering effects. A relatively thin mesoporous layer of $\sim$ 200 nm results in optimum crystallinity of the perovskite layer and hence optimum efficiency [129]. The previous record PCE value of (20.2%) was measured from a mesostructured cell as described [130]. The planar *n–i–p* structure is was developed from mesoscopic structure by using the same materials but removing the

mesoporous layer. Device engineering with particular attention to the interfaces has now led to high efficiency devices (19.3 % PCE) with the mesoporous layer omitted [110].

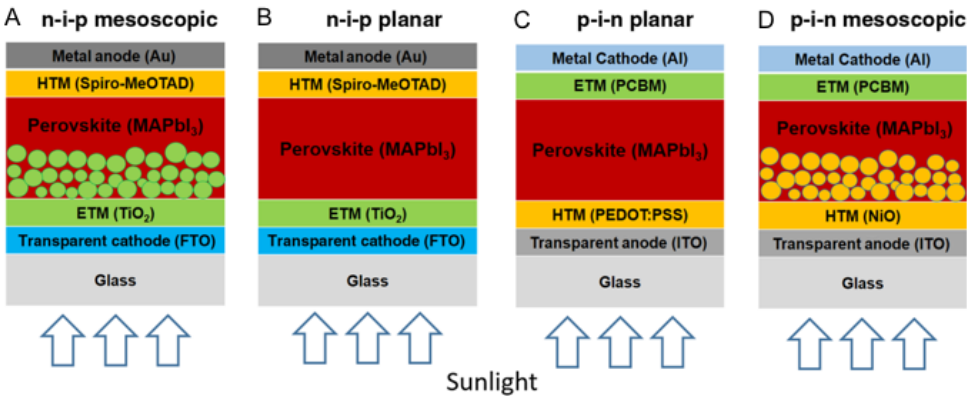

Figure 3.6: Perovskite solar cell architectures. Schematics of perovskite solar cell architectures, with typical materials used for the standard architecture **(A)** *n–i–p* mesostructured, **(B)** *n–i–p* planar, and inverted architecture **(C)** *p–i–n* planar, and **(D)** *p–i–n* mesostructured configurations. Figure taken from [129].

In the case of the inverted (*p–i–n*) planar perovskite device the HTM is deposited first on a transparent (indium tin oxide or ITO) typically using a layer of $\sim$ 50 nm p-type transparent conducting polymer such as poly(3,4-ethylenedioxythiophene) poly(styrene-sulfonate) (PEDOT:PSS). The active layer is a $\sim$ 300 nm perovskite film and the ETM on the rear of the device is an organic ETM which is typically [6,6]-phenyl C61-butyric acid methyl ester (PCBM) and a metal cathode (Al or Au). This device architecture lends its origins to organic photovoltaics, where these transport layers are commonly used. Research of the inverted device structure has involved switching the selective contacts from organic to inorganic materials (NiO, NiMgLiO, $TiNbO_2$, and $ZnOTiO_2$), even being used to fabricate large-area (1 cm^2), high-efficiency (15% PCE) devices which is a crucial landmark along the journey to commercialisation of perovskite solar cells [131, 132].

3.2.2 Perovskite Compositions

A plethora of perovskite compositions have been developed for PV applications, proving the material to be diverse and widely adaptable to given applications. Much of the work

investigating different perovskite compositions is focused on high-efficiency but also the development of a material that is stable under illumination and ambient conditions.

The second most common composition in perovskite PV literature is $MAPb_{(3-x)}Cl_x$, where the Cl is introduced via $PbCl_2$ or MACl in the precursor solution. The role of chlorine and its inclusion in the final material has been debated, with conclusions that a negligible amount of Cl is present [133–135]. Yet, the effect of chloride on the formation process of perovskite films is well documented [133–137]. One of the main observations is that inclusion of chlorine in the precursor solution results in higher electron and hole diffusion lengths and reduced trap-state density [113].

Part of the increase in device performance of perovskite solar cells is attributed to tuning of the band gap to the optimum value for the solar spectrum. It has been found that varying the X-site halide in perovskites with increasing atomic size (from Cl to Br to I) leads to a decrease in the bandgap energy [18]. Alternatively, increasing the size of the cation also decreases the bandgap energy (from Cs to MA to FA) [18, 138]. Using these methods, the bandgap can be varied over almost the entire visible spectrum from 1.5 to 2.3 eV.

Caesium based perovskites have also gained attention in the past few years, with attention focused on the prospect of improving stability of perovskite solar cells. This is based on the rationale that organic-based semiconductors are often found to encounter issues with degradation as they are often more reactive and prone to changes in composition when subjected to high amounts of energy (heat or light). All-inorganic perovskites are indeed found to have better stability at high temperatures, although devices have much lower PCE when compared to other compositions [139, 140]. $CsPbX_3$ perovskites have been found to be particularly useful as materials for nanocrystals, with caesium the most prominent cation used for perovskite nanocrystals [141–143]. Most state of the art devices use a perovskite absorbing layer composed of a mixture of cations and halides. For example Saliba and colleagues used a triple-cation mixture (Cs, MA and FA) to fabricate devices with PCE above 21 % [21].

3.2.3 Fabrication Methods

3.2.3.1 Precursor Solutions

Arguably the most important factor for fabricating solution-processed perovskite materials and solar cells is the precursor composition. Typically, metal-halide salts are combined with cation-halide compounds in a polar aprotic solvent such as dimethylformamide (DMF), dimethyl sulfoxide (DMSO), γ-butyrolactone (GBL) or acetonitrile. The most common solution used is with methylammonium iodide (CH_3NH_3I or MAI) and lead iodide (PbI_2) with a 1:1 molar ratio in DMF. Recently however, work by Noel and co-workers developed a precursor solution based on acetonitrile and methylammine as solvents. Methylammine gas is bubbled through the solution containing precipitated precursor salts and acetonitrile, forming a clear yellow solution [144]. This solvent system is far less toxic than those commonly used and owing to its low boiling point, able to induce rapid crystallisation of of the perovskite, resulting in improved morphology.

3.2.3.2 Spin Coating

The most widely used method for fabricating solution-processable solar cells for research is spin coating. This method involves dispensing a liquid solution of the solid material or solid precursor materials on to the substrate, and rotating the substrate to coat it with a thin film of the material. This technique has proved very successful for fabricating relatively small-area (< 2 cm) perovskite based solar cells but is not scalable and has low reproducibility. Therefore, it is confined to the realm of small-scale research only. For depositing the perovskite layer alone, there are several different routes to achieve a perovskite thin film via spin coating. These range from simple methods such as one-step spin coating [127, 145, 146] to more elaborate multi-step processes [147–149]. Following these processes, the solid precursors precipitate to form a bulk (three-dimensional) polycrystalline film upon evaporation of the solvents. Conversion to the perovskite tetragonal/cubic phase can occur during spin coating, following the formation of intermediate phases [147]. This is usually followed by an annealing step

which functions to fully evaporate the solvent and additionally in some cases, complete the conversion to the perovskite crystal phase.

Depending on the precursor solution used, it is often found that spin coated films have large surface roughness and result in devices with a poor performance. A highly successful method to overcome this problem uses a mixed solvent system and a gas quenching or gas-assisted method, shown in Figure 3.7 [35, 146, 150]. With the mixed solvent system of DMSO and DMF for example, PbI_2 forms complexes with the DMSO upon evaporation of the DMF, producing an intermediate crystal phase and retarding the fast reaction between precursors [147, 151]. A high pressure flow of gas ($\sim$ 6 Bar) is used to rapidly dry the parent solvent (DMF) and this consistently results in smooth, pinhole-free films [146]. Zheng and colleagues recently demonstrated this technique successfully without the need for spin coating [152]. The most widely used technique for removing the parent solvent is typically referred to as 'solvent quenching', which involves dropping an anti-solvent (such as toluene) on the film following deposition [147]. This has a similar effect to the gas-assisted method but is well known to produce far less consistent results and is less robust.

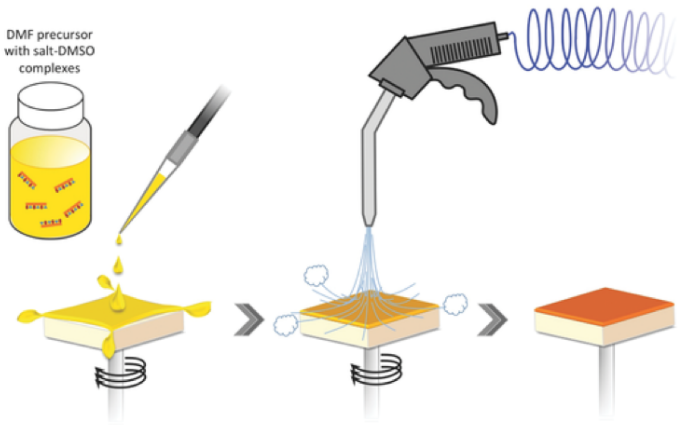

Figure 3.7: Gas-assisted spin coating method. The process for spin coating the DMSO-complex based precursors via the gas-assisted method. Figure taken from [146].

3.2.3.3 Upscaling

One potential route for up-scaling the fabrication of perovskite PV is vapour deposition. This has been achieved by co-evaporating solid precursor materials using a multi-source

evaporation system. It is found that the resulting films are smoother, with far superior uniformity and controllability in thickness [153–155]. Other explored pathways to large area devices include spray-coating [156–158], slot-die coating [159, 160] and inkjet printing [161, 162].

3.2.4 Applications

3.2.4.1 Semi-Transparent Solar Cells and Building Integrated Photovoltaics

One major potential application of perovskite materials is for semi-transparent solar cells. In this case, high visible transmittance is valued alongside high PCEs. Such devices are prime candidates for structural integration with buildings, e.g. for use as window panes where light is harvested predominantly at non-visible wavelengths. This is known as building-integrated photovoltaics or BIPV. Perovskite solar cells have the ability to be fabricated as semi-transparent devices owing to their high absorption coefficients, allowing ultra-thin active layers to be used. The major challenged faced when designing such devices is that all layers must be transparent, including the electrical contacts. As a result of this plus optical losses, semi-transparent devices are always less efficient than their non-transparent counterparts.

Another challenge presented by BIPV is due to the importance of aesthetics in building design. Neutral-coloured modules are the most highly desired, since they have little impact on the appearance of the building, being indistinguishable from tinted windows. There have been many different approaches to designing a neutral-coloured semi-transparent perovskite solar cell. One method reported by Eperon *et al.* is to use a microstructured perovskite layer, comprised of small islands of solid material. This resulted in the most efficient devices with $\sim$ 8 % PCE and $\sim$ 7 % average visible transmittance (AVT) and the most transparent devices at $\sim$ 3.5 % PCE, $\sim$ 30% AVT [39]. Later Ramírez Quiroz fabricated devices having $\sim$ 37% AVT with 7.8 % PCE, and also $\sim$ 46% AVT and 3.6 % PCE using a 'solvent-solvent extraction' method (Figure 3.8) [35]. The choice of contacts for semi-transparent perovskite cells include an ultra-thin metallic layer [34], silver nanowires [28, 35, 37], dielectric–metal multilayers [36], sputtered

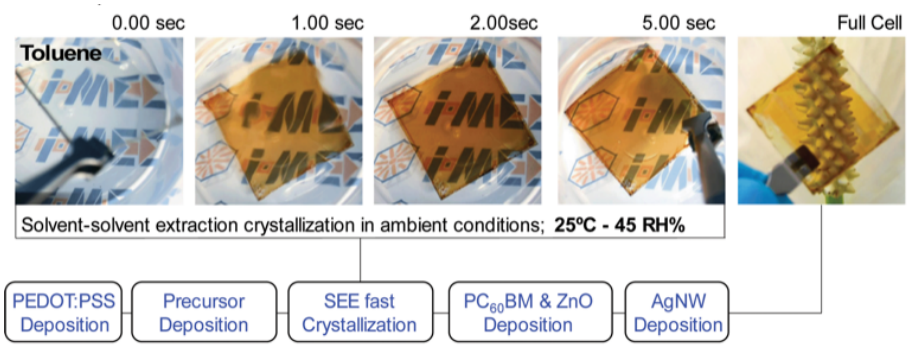

Figure 3.8: Transparent perovskite solar cell fabricated using the 'solvent-solvent' extraction method. After spin-coating the perovskite precursor solution (GBL solvent), the film is submerged in toluene (an antisolvent for the precursors), resulting in improved transmittance. Figure taken from [35].

ITO [25, 27, 29, 38, 163, 163], ZnO:Al [40] and a polymer-embedded metallic grid [164]. Since transparent conducting oxides (TCOs) are already typically used as front electrodes, they seem an obvious route for rear transparent contacts. The ideal deposition method for most TCOs is magnetron sputtering as it allows for control over the composition of the deposited film. As a result, sputtering procedures have been developed over a long time and optimised for TCOs with both high transparency and conductivity. However, this presents a problem for compatibility with the main established perovskite solar cell architectures; since the rear contact is usually the last to be deposited, the layer beneath should be mechanically stable enough to withstand the high impact force that it is subjected to during sputtering. For the most efficient devices, this layer is an organic material that is easily damaged by sputtering. One method that has been adopted to overcome this problem is the deposition of a buffer layer, such as MoO_3 [40] or AZO nanoparticles [163] before the final TCO layer (ITO) is deposited. Bush *et al.* demonstrated that the perovskite cell benefits greatly from using ITO as a transparent electrode as it acts as encapsulation, protecting the device from degradation. A T_{80} lifetime of 124 hours is measured with the device subjected to 100 °C. This method is now the most widely used for semi-transparent perovskite solar cells, particularly in cases where they are used for a sub-cell for a perovskite tandem device.

3.2.4.2 Tandems

Arguably the most viable application of perovskite as a material for PV is in tandem solar cells. Solar cells made from materials that benefit from a wealth of research and engineering spanning decades could be improved by adding a perovskite sub-cell. Such 'tandem solar cells' have been realised with crystalline silicon and CIGS. Since perovskite typically absorbs visible and ultraviolet wavelengths ($\lambda_G \sim 800$ nm), it is optimally used as front cell to collect higher energy photons. Devices can be made to be transparent for longer wavelengths, so that they can be harvested by the cell beneath which are optimised for infrared energy conversion.

Individual cells can be mechanically stacked following the separate fabrication of each device. In this method, they may be connected in series to form a two-terminal tandem cell or simply retain their individual contacts (four-terminal tandem). Alternatively, a two-terminal tandem can be fabricated by integrating both sub-cells monolithically. This requires that the current output is matched between each sub-cell. Four-terminal tandem modules would require separate control systems (maximum power-point tracking) and electrical connections for each sub-cell, which is an advantage for efficiency but would increase the initial costs of a PV system.

Currently the most successful tandem devices have been fabricated with crystalline-silicon bottom cell. Mailoa and colleagues fabricated the first two-terminal tandem based on amorphous silicon with a relatively low efficiency of 13.7 % due to parasitic absorption of light in the HTM of the perovskite sub-cell [28]. Werner *et al.* also fabricated a monolithic device with a silicon heterojunction bottom cell, reaching a maximum of 21.2 % PCE on an area of 0.17 cm^2 and 19.2 % PCE on a device with area 1.22 cm^2 [27]. Recently Bush and co-workers also fabricated a monolithic device with a mixed caesium-formamidinium perovskite and a tin oxide buffer layer, deposited using atomic layer deposition. A record efficiency of 23.6 % was achieved [30]. Recently a PCE of 20.7 % has been achieved with a four-terminal perovskite-CIGS tandem device. Here, Guchhait *et al.* investigated different buffer layers for the ITO deposition, finding that a thin layer of silver was the most effective [32]. Finally, recent progress towards large area tandems have been made by Paetzold and co-workers. They recently achieved

a PCE of 17.8 % by stacking a perovskite module on a CIGS bottom module with an area of 3.76 cm^2 [165].

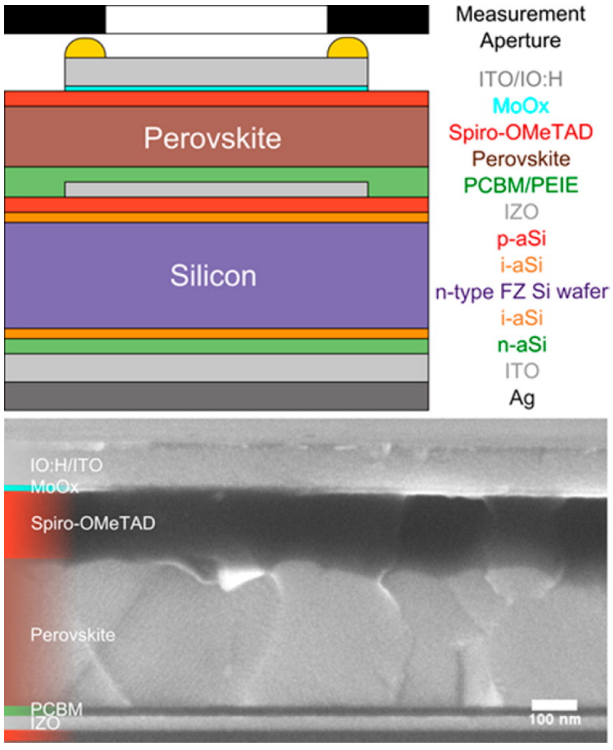

Figure 3.9: Monolithic perovskite-silicon tandem solar cell. Schematic of a monolithic two-terminal perovskite-silicon tandem solar cell. The SEM images shows the perovskite top-cell. Figure taken from [27].

All-perovskite tandems can also be realised owing to the ability to tune the bandgap. Hence tandems have been fabricated by using multilayers of differently composed perovskite [24–26].

3.3 Nanocrystals for Perovskite Solar Cells

Perovskite nanocrystals similarly to their bulk material counterparts have attracted a large amount of attention in recent literature. Since the first report of a perovskite solar cell with nanocrystal sensitisers grown on TiO_2-based solar cells [11], colloidal perovskite nanocrystals have been developed with high reported PL quantum yield (up to 90 %) [141]. These materials have been successfully applied as light emitters for infrared and visible LEDs [166–168] and absorbers in solar cells [169]. Although perovskite nanocrystals lead in the field of perovskite-based LEDs, they fall short of the PCE

produced by solar cells based on bulk-perovskite by more than a factor of two. The likely reason for this is that the high efficiency of bulk-perovskite solar cells is largely owed to its excellent ambipolar charge-transport properties; a trait that nanocrystals do no not typically exploit.

The combination of inorganic nanocrystals and bulk perovskite has also been explored, mainly for the application of light emitting materials. Ning *et al.* introduced 'quantum-dot-in-perovskite solids' as a hybrid material for light emission, using PbS quantum dots dispersed in a bulk MAPI matrix [170]. This configuration utilises the charge transport properties of bulk perovskite and the high radiative efficiency of the PbS quantum dots. Charge is transfered from the bulk perovskite to the lower-bandgap PbS quantum dots, where infrared light is emitted. In this case, the bulk perovskite crystals are reported to be grown epitaxially on the surface of PbS quantum dots. It is proposed that the process of heteroepitaxy occurs due to the compatibility between the two crystal structures (both are related to the cubic system) and each have a six-coordinated Pb atom, with Pb-Pb distances within 4.6% of each other [148].

One issue that is presented by incorporating colloidal QDs to a crystalline film is the organic ligands needed to prevent QD aggregation and allow them to be dispersed in solution. This introduces long-chained dielectric species to the bulk film and thus increases the likelihood of the formation of crystalline defects, recombination centres, trap-states etc. This issue is overcome by a ligand-exchange strategy based on previous work involving the replacement of organic ligands with iodide [171, 172]. This allows for atomic-level coherence between the QDs and MAPI and also allows the inorganically-terminated QDs to be dispersed in a solution with PbI_2. The QDs become passivated by the perovskite film that grows on their surface, demonstrated by a 100x increase in photoluminescence quantum efficiency (PLQE) compared to when NaI (an incompatible lattice) is grown on the surface of the QDS [170]. This work was continued to produce infrared field-emission photodiodes using the same approach with resulting detectivities of $> 10^{12}$ Jones [173]. This represents an important step towards optoelectronic devices such as solar cells and LEDs using QD-in-perovskite materials.

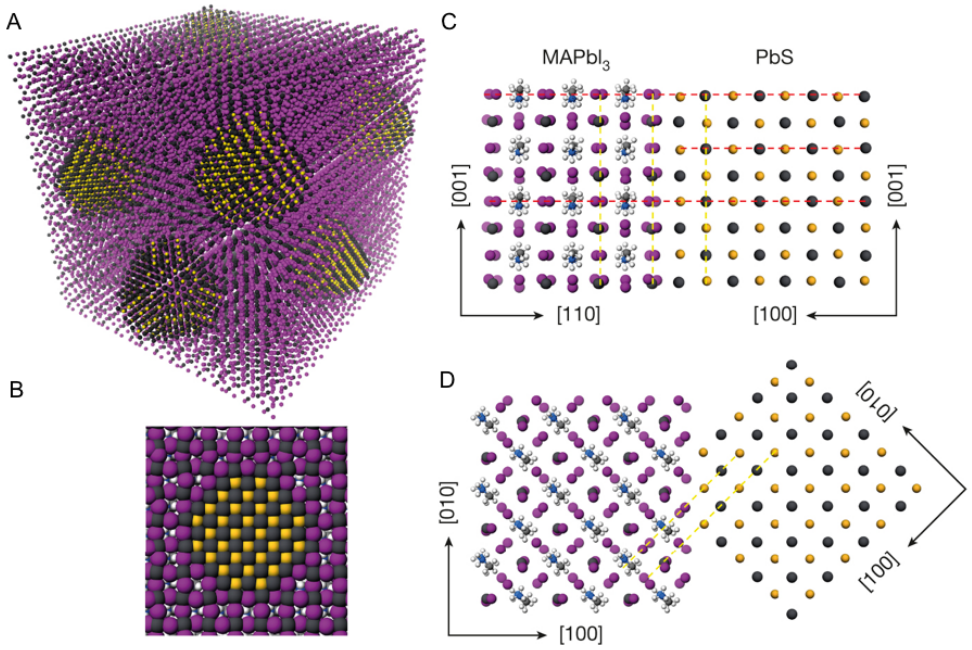

Figure 3.10: Theoretical model of MAPI grown on PbS QDs. (A) Atomistic model of PbS QDs embedded in a perovskite matrix. **(B)** Cross-section of a single QD in MAPI crystal. **(C)** Modelling of PbS and MAPI crystal structure and their interface, showing the XZ plane and **(D)** the X-Y plane. Grey represents lead; purple, iodine and yellow, sulfur. Figure taken from [170].

PbS QDs have also been used in perovskite solar cells as a HTM and also an intermediate layer. Inorganic HTMs are preferred over their organic counterparts due to the host of issues harboured by organic charge transport layers such as PEDOT:PSS and spiro-OMeTAD. Hu *et al* use PbS QDs as the HTM in planar inverted perovskite solar cells, extending the photon-to-electron conversion to infrared wavelengths [174]. In this study, QDs with various bandgaps are investigated, with the optimum found to be 1.4 eV, yielding a 7.5 % efficient device. Li and co-workers adopted a similar approach, demonstrating devices with 8 % PCE using PbS quantum dots as an inorganic HTM in place of spiro-OMeTAD for the standard architecture mesoscopic devices [175]. An increase in J_{sc} is attributed to the additional absorption provided by the PbS QDs and is reported to result in a relative efficiency increase of 70 %. $CuInS_2$ and NiO QDs have also been used as a HTM in perovskite solar cells, further demonstrating the applicability of inorganic nanomaterials for charge transport layers in the research field [176, 177].

Yang and Wang fabricated perovskite solar cells with a layer or PbS QDs between the

bulk perovskite and TiO_2 in mesostructured devices [178]. The PbS quantum dots are produced using a successive ionic later adsorption and reaction method on the surface of TiO_2. The hybrid devices showed both enhanced efficiency and stability, which are proposed to be due to the PbS layer improving the crystallisation of the perovskite. Graphene QDs have also been used as an interlayer in a similar manner, increasing the speed of electron extraction by more than double [179].

Another application of nanocrystals has been the replacement of mesoporous TiO_2 as the charge collection layer with ZnO nanorods in perovskite solar cells [180]. Here, Son *et al.* create devices with > 11 % PCE by infiltrating ZnO nanorods (ETM) with perovskite. The solar cells have almost ideal EQE spectral shapes and a high J_{sc} (20.08 $mAcm^{-2}$) but a relatively low fill factor (56 %).

3.4 Conclusion

A multitude of unique physical characteristics have been observed in metal halide perovskites, rendering the crystal family difficult to classify within the existing framework of material science. Understanding of the material is evolving rapidly due to the exponential rate of research. The development of field is known to be hindered by contradictory reports, fuelled by oversights of external factors such as sample variation and experiment conditions. The fundamental material properties should be decoupled from observations that can be largely affected by sample quality, sample history or environmental factors. Properties that are coherently identified throughout literature should be attributed to the material and those that vary widely should be assigned to factors related to sample preparation. In spite of these factors, it appears that perovskite materials are strong candidates for solution-processed optoelectronic technology, close to the point of commercialisation, given that the issue of material stability is overcome. Most of the device fabrication research is focused on improving efficiency using only perovskite as the absorbing material. Little has been explored in combining perovskite with nanomaterials within the same device, despite the fact that technology based on multiple materials is predicted to have a large presence in the future PV market.

The most promising application of perovskite materials to photovoltaics is tandem solar cells, employing both perovskite and traditional semiconductor materials. Directly competing with well-established technologies is difficult and to some extent non-productive when the combination of new and old generation materials holds the greatest potential in terms of device performance. "*If you can't beat them, join them*", literally, in this case.

Chapter 4

Experimental Methods

This chapter describes the experimental procedures and materials corresponding to later chapters. Each section or subsection typically begins by introducing the apparatus, technique or material by providing some background principles. Following this, the specific details of the methods used for this work are stated.

4.1 Thin Film and Device Fabrication

4.1.1 Spin Coating

Spin coating is a technique commonly used for deposition of thin films from liquid solution. It is mostly used in research applications, where small prototype samples are required. It is not a particularly scalable technique and generally yields a relatively poor uniformity of layers on larger scales. It is however very useful as a simple, tunable deposition technique for small-scale depositions. It is used extensively for the application of photoresists for example, used for lithography. During the process of spin coating, the precursor solution is dispensed on to the substrate which is rotated at some given angular speed, ω. The dispensing of solution can either be carried out *in situ* while the substrate is spinning or alternatively before the spinning begins. These methods are referred to as 'dynamic' and 'static' dispensing, respectively. In most cases, the final

film thickness is inversely proportional to the rotational speed, i.e. $d \propto \frac{1}{\sqrt{\omega}}$, where d is the film thickness.

The process of spin coating is outlined in Figure 4.1. Typical rotational speeds are on

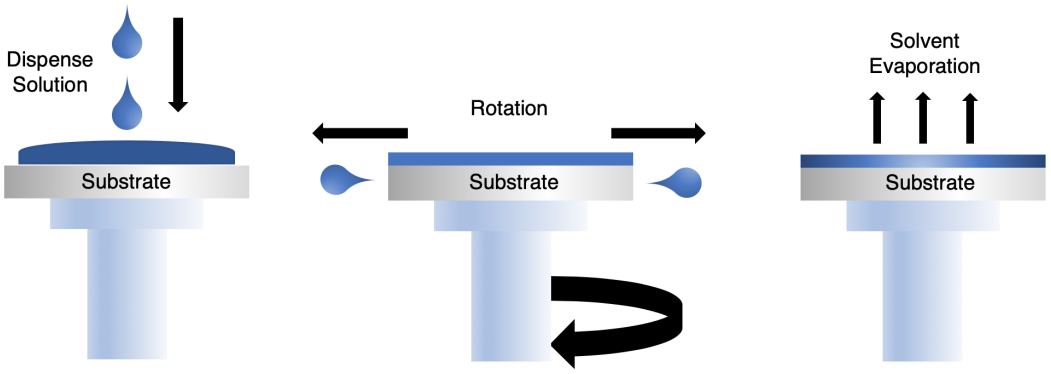

Figure 4.1: Spin coating process. The solution is dispensed on to a substrate which rotates. The rotation causes the solution to be spread outwards, with most of it leaving the substrate. The solvent begins to evaporate, leaving a solid film remaining.

the order of 1000 RPM. When the sample is spinning at this rate, the rotational forces exerted on the liquid causes the majority to be expelled from the edges. This is one major disadvantage of spin coating, since much material is wasted during the deposition process. When the thickness of the liquid layer becomes thin enough, it will rotate with the spinning substrate. The solvent evaporates, leaving behind the solutes of the solution, which may then undergo further chemical reactions or crystallisation processes.

In Chapters 5, 6, 7 and 8 spin coating used used to produce the samples (detailed in the sections below). The spin coater used is a Laurell WS-400-6NPP-LITE Spin Processor, which is installed inside a glovebox.

4.1.2 Thermal Evaporation

Thermal evaporation is another technique that can be used for the deposition of thin films. Thermal evaporation is a form of physical vapour deposition (PVD), since it involves the evaporation of a material to form a vapour, which is directed towards the substrate. The schematic for a thermal evaporator is shown in figure Figure 4.2. High vacuums are required for coating materials via thermal evaporation in order to remove

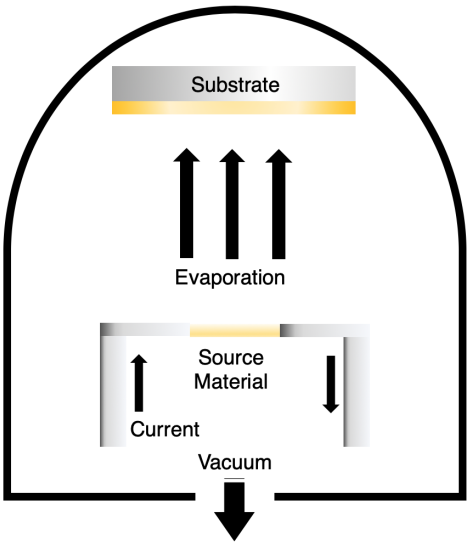

Figure 4.2: A thermal evaporator. The substrate is held an an inverted position in a vacuum chamber. The source material is connected to a transformer filament, which provides a high current through the source material. As the source heats up, it begins to evaporate and the vapour travels upwards towards the substrate. A layer of material is gradually deposited on the substrate.

any vapour in the chamber, providing a large mean free path for the desired vapour to travel.

When used in combination with a deposition mask, the deposited thin film may be patterned. This is particularly used for microfabrication and patterning electrodes for optoelectronics. The source material can be many different kinds of solids but metals are the most common materials used. Typically, the material is placed in a crucible which is heated via a surrounding coil through which electrical current is passed. Alternatively, the material may be placed directly on the current-carrying coil. The deposition rate can be controlled by the amount of current supplied to the coil, with higher currents producing more heat and hence higher rates of evaporation. Very thin layers may be achieved via thermal evaporation (several nm) with a reasonable level of control. To monitor the thickness, a piezoelectric crystal is typically used, which can detect small variations in the oscillating frequency as material is deposited.

4.1.3 Lead Halide Perovskite Thin Films

Precursor solutions for LHPs typically use a polar aprotic solvents such as dimethylformamide (DMF), dimethylsulfoxide (DMSO) and acetonitrile (MeCN). The solutes are ionic compounds containing the components to be incorporated in the resulting perovskite crystal. For $MAPbI_3$, these are usually lead iodide (PbI_2) and methylammonium iodide (CH_3NH_3). These are dissolved to form an ionic solution which to be deposited on the substrate.

For the studies in this thesis, two different precursor solutions are created in order to form either $MAPbI_3$ or $MAPbI_{3-x}Cl_x$. Glass substrates were cleaned by sonicating in Helmanex III solution with dionised water, and subsequently sonicating in isopropyl alcohol. They are then treated with oxygen plasma for 10 minutes before being transferred to an inert environment for deposition. For the $MAPbI_3$ solution, a mixed solvent system is used with DMF and dimethylsulfoxide (DMSO). PbI_2 and MAI is combined with a molar ratio of 1:1 in a DMF:DMSO ($\sim$ 9:1) solvent to form a PbI_2–DMSO complex. The $MAPbI_3$ solution was dispensed on the glass substrate and spin coated at 3000 RPM and $\sim 10s$ after the the procedure is initiated, a flow of nitrogen gas is applied to the film to dry the parent solvent and produce smooth films. The $MAPbI_3$ films are then annealed for 10 mins at 100 in a nitrogen atmosphere. For the $MAPbI_{3-x}Cl_x$ films, a precursor solution of methylammonium iodide (MAI): PbI_2 : $PbCl_2$ with a molar ratio of 4:1:1 is prepared in dimethylformamide (DMF) with a weight ratio of 40 wt %. The $MAPbI_{3-x}Cl_x$ solutions are dispensed on the glass substrates at a speed of 4000 RPM for 30 s in a nitrogen atmosphere, yielding an active layer of $\sim$ 300 nm thickness. Smooth, highly specular films are achieved, without the need for a quenching technique. The $MAPbI_{3-x}Cl_x$ films are then placed on a hotplate at 80 for 2 hours in a nitrogen atmosphere to anneal.

4.1.4 Inverted Planar Perovskite Solar Cells

In the field of perovskite photovoltaics, 'Inverted' solar cells refer to device architectures that have the hole-transporting layer in the 'front' of the device, i.e. the side of the device

which faces the illumination. This is in contrast to 'standard' architecture devices, which are fabricated with the electron-transport layer at the front. 'Planar' means that the device layers are flat and arranged sequentially. This is opposed to a common standard device architecture which uses an absorber deposited on a mesoporous scaffold (such as TiO_2), reminiscent of dye-sensitised solar cells. Usually the fabrication procedure starts with a transparent substrate (such as glass), coated with a transparent contact. This contact is typically a transparent conducting oxide (TCO) such as indium tin oxide (ITO) or flourine-doped tin oxide (FTO). The next layer to be deposited is a charge-transport layer, which needs to be transparent in order for light to reach the absorber layer sandwiched between charge-selective contacts. The final layer is another contact, which is typically a conductive metal such as gold, silver or aluminium. This layer may also be transparent, especially if the devices are to be used for applications such as tandem solar cells (see Chapter 3).

The solar cells fabricated in this thesis use poly(3,4–ethylenedioxythiophene) polystyrene sulfonate (PEDOT:PSS) as the hole transporting layer and [6,6]–phenyl-C_{71}–butyric acid methyl ester ($PC_{70}BM$) as the electron transporting layer. To fabricate the solar cells, firstly glass substrates coated with a 100 nm layer of indium tin oxide (ITO) (Osilla) are cleaned by sonicating for 10 minutes using a solution of Hellma Analytics Hellmanex III and deionised (DI) water. The substrates are then rinsed twice with DI water before being sonicated in isopropanol for a further 10 minutes. The substrates are dried and placed on a hotplate at 120 °C before depositing the hole transporting layer by dispensing PEDOT:PSS (Osilla) while the substrate is spinning at 6000 RPM for 30 s, giving a film of $\sim$ 40 nm thickness. The substrates are then placed on a hotplate at 120 °C for 30 minutes in a nitrogen atmosphere to ensure that any remaining water is evaporated. The substrates are cooled to room temperature before depositing the active layer as described in section 4.1.3. Subsequently, a layer of $PC_{70}BM$ is spin-coated on the sample at a speed of 1000 RPM using a solution of 50 mg/ml in chlorobenzene. The metallic contact is formed using an Edwards E306 vacuum coating system housed inside a nitrogen glovebox. A $\sim$ 100 nm thick layer of aluminium is deposited at a rate of 0.1 nm/s. The final devices are encapsulated with epoxy (Ossila) and a glass coverslip. The MAI is purchased from Ossila and the PbI_2, $PbCl_2$ and all solvents are from Sigma

Aldrich. The devices are outlined in Figure 4.3, showing a photograph of a perovskite thin film (a) and pixelated solar cell (b), a cross-sectional SEM image (c), and schematic of the device (d).

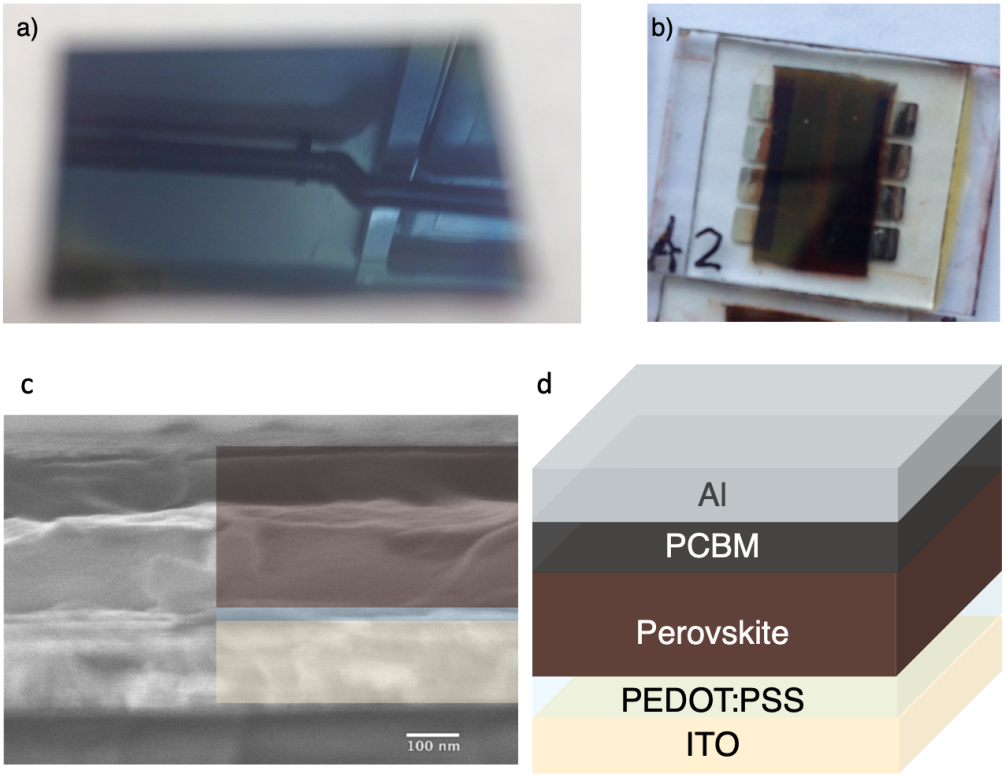

Figure 4.3: Inverted-planar perovskite solar cells. a) Photograph of a smooth mirror-like $MAPbI_3$ thin film. b) Photograph of inverted planar perovskite solar cells with a pixelated architecture. There are eight pixels, which comprise individual solar cells with an active area of 0.026 cm^2. c) Cross-sectional SEM image of the device. d) Device architecture for the inverted planar perovskite solar cells.

In Chapter 8, blends of PEDOT:PSS and CdTe quantum dots (QDs) are fabricated. For this work the QDs were purchased from Plasmachem. The film thickness of all layers were determined using profilometry.

4.1.5 Optimisation of Devices

When attempting to fabricate solar cells, there exists an essentially infinite parameter space to be explored, as with the development of any technology. Within this parameter space, there are well-known parameters that are commonly investigated to comprise the first iterations of device design. For thin-film solar cells, some examples include the

thickness of the layers, composition of layers, deposition rates and annealing temperatures. Even when fabricating solar cells by following a known 'optimised' process for the first time in a particular laboratory, several parameters often need to be re-tuned in order to achieve the same performance. This is due to differences in the conditions that arise naturally between laboratories. It is extremely difficult to record the conditions in a laboratory where a process is documented to an extent that ensures reproducibility of results within experimental error. Moreover, often such information is not recorded or supplied when reporting a process.

For the reference devices fabricated in this thesis, a fabrication process was followed according to a known recipe. However, the author was unable to reproduce the typical performance of reported devices and hence optimisation processes was carried out. A clear example can be observed in the device parameters shown in Figure 4.4. Here,

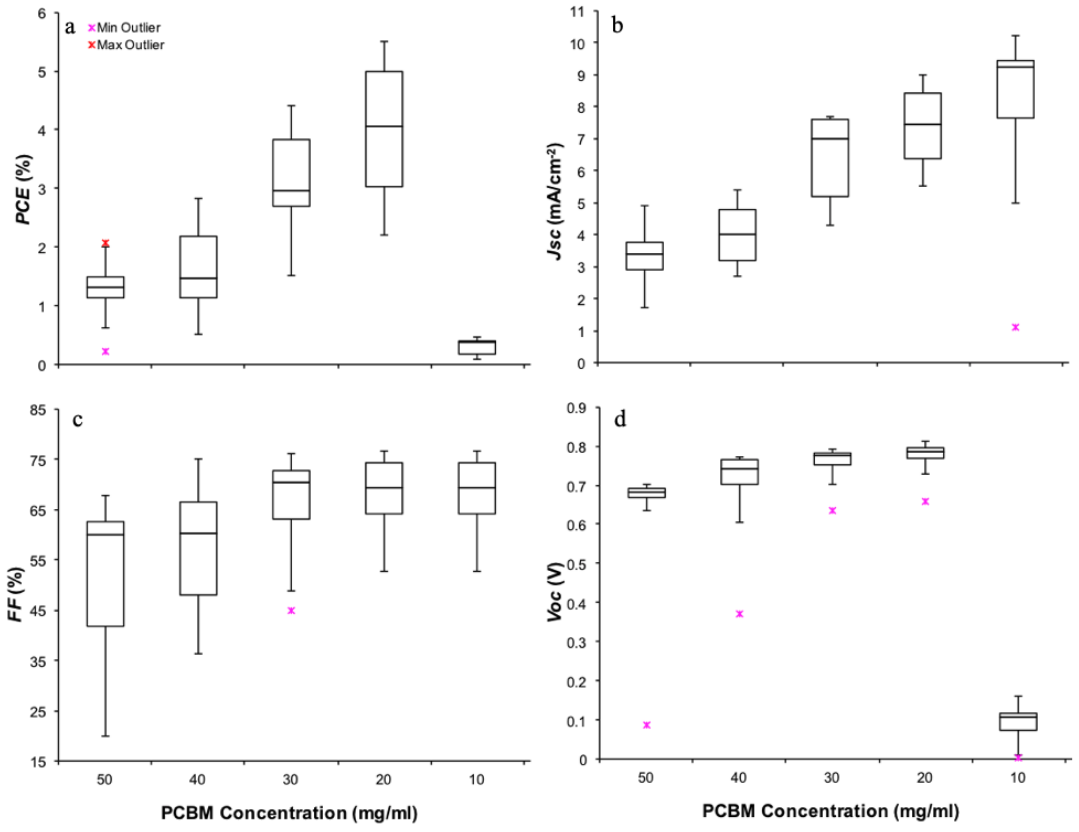

Figure 4.4: Optimisation of inverted planar perovskite solar cells. a) PCE, b) short-circuit current density, c) fill factor, d) open-circuit voltage of devices as a function of PCBM concentration.

devices were fabricated according to the process described in the previous subsection but

with $MAPbI_3$ replacing $MAPbI_{3-x}Cl_x$. Due to the enhanced smoothness of the layer as described in Chapter 7 and Chapter 5, the thickness PCBM layer that is deposited subsequently should can be reduced while still maintaining a planar layer. The thickness of the PCBM layer can be controlled by changing the concentration of the solution for spin coating, with lower concentrations resulting in thinner films. An increase in the short-circuit current density is observed as the concentration is reduced from 50 mg/ml (Figure 4.4b), likely due to enhanced charge extraction. However, at a concentration of 10 mg/ml, the open circuit voltage is reduced by almost a factor of ten (Figure (Figure 4.4d). This is likely caused by the formation of short-circuit pathways which effectively reduce the shunt resistance to almost zero.

4.2 Thin-film Characterisation Techniques

In order to understand the characteristics of perovskite thin films, several experimental techniques are used in this thesis. This section describes the main methods used.

4.2.1 Scanning Electron Microscopy and X-Ray Diffraction

Scanning electron microscopy (SEM) uses a type of electron microscope that scans the surface of a sample with a focused beam of electrons. The electrons interact with atoms in the material studied, producing different types of signals which can be used to obtain information regarding the surface being subjected to the beam. Scanning electron micrographs are shown in Chapters 7 and 8. For these images, a Zeiss (LEO) 1450VP Scanning Electron Microscope is used with an accelerating voltage of 20 kV.

Nonconductive samples typically collect charges if they are subjected to an electron beam, which can cause issues for imaging. Samples should therefore be electrically conductive at the surface. The samples used in this thesis are therefore coated with an thin layer of gold, deposited on the sample by sputtering. The type of signal mode used for the work in this thesis is the secondary electron mode. In this case, electrons are ejected from the sample following exposure to the beam via inelastic scattering. The electrons are collected via a detector and an image is produced based on the number of

electrons detected. The brightness of the image (number of electrons detected) at each point depends on the angle of incidence, with steeper angles being brighter due to an increased interaction volume.

An X-Ray diffraction pattern is shown in Chapter 5 to identify the Bragg reflections of the crystalline structure. For these measurements, the samples were characterised using a Rigaku SmartLab X-ray diffractometer with a Cu K-alpha 9 kW anode.

4.2.2 Absorption Spectroscopy

Absorption spectroscopy measures the absorption of light by a material for a range of photon energies, E. This has obvious applications for optoelectronics such as solar cells. It can be used to determine the bandgap of a semiconductor and also its absorption coefficient, $\alpha(E)$, for example. The absorption coefficient is an important parameter, giving the absorption per unit depth of a material, as a function of photon energy. Absorption of a sample is usually inferred by calculation, using the optical transmission and reflectance spectra for the material. The processes of absorption, transmission and reflectance are shown in Figure 4.5.

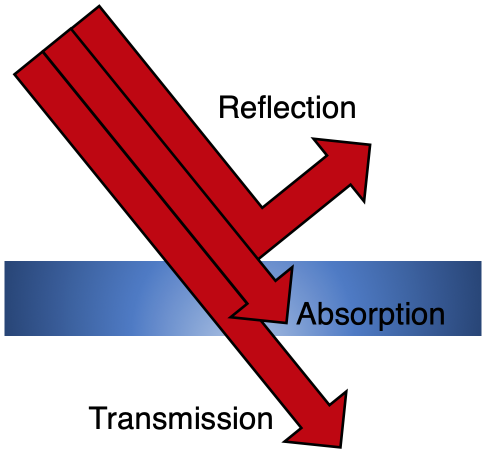

Figure 4.5: Processes of light absorption, transmission and reflection. The time delay between the arrival of the excitation pulse and photon emitted from the sample is recorded using 'reverse mode'. A histogram of time events is developed over many pulses.

In this thesis, two different methods are used to measure the absorption of light in lead halide perovskites. In Chapter 5, a Jasco V-570 UV/Vis/NIR spectrophotometer is

used. A spectrophotometer contains several light sources and other optical components for measuring the optical transmission and specular reflection of a material. Different light sources provide illumination for different parts of the electromagnetic spectrum, ranging from ultraviolet (UV) to near-infrared (NIR). The light source is monochromated to provide a narrow-bandwidth illumination beam incident on the sample, which scans a through a range of wavelengths. At each wavelength, the detector records a value for either the transmitted light or reflected light.

In Chapter 6, a custom setup is used instead so that the absorption can be measured while the sample is contained in a cryostat, in order to perform low-temperature measurements. This setup uses a white light source (Thorlabs), incident on the sample, providing illumination across the spectral range of the source. The transmitted light can be collected from the other side of the sample and focused on to a spectrometer, so that the entire transmitted spectrum can be acquired in one measurement without the need for scanning the wavelength of the illumination beam. Both specular and diffuse reflection can be measured using an integrating sphere, positioned on the front surface of the sample. This allows for a more accurate determination of the absorption spectrum, since all reflected light is accounted for. Figure 4.6 shows a schematic of the setup to measure the optical transmission.

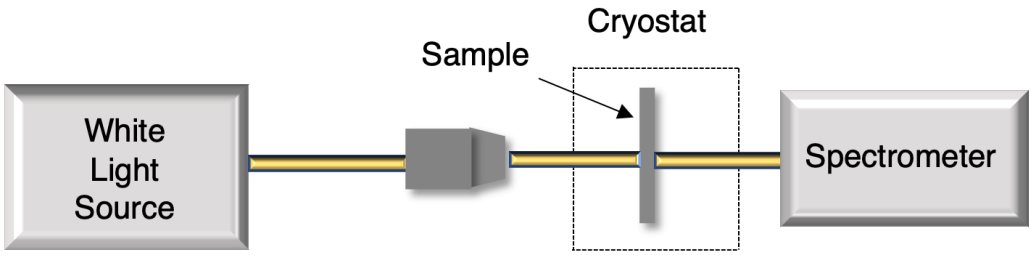

Figure 4.6: Absorption spectroscopy setup in transmission configuration. The sample is illuminated with a white light source. The transmitted light is collected by a spectrometer.

To calculate the absorption coefficient, a reference measurement for the sample is obtained by first measuring the light transmitted by the glass substrate on which the thin film is successively deposited. In this work, transmission and reflectance spectra are

measured for lead halide perovskite thin-films. This data, along with the thickness of the film is used to calculate the absorption coefficient by using the equation:

$$\alpha(E) = \frac{1}{d} \ln \left(\frac{(1 - R(E))^2}{T(E)} \right) \tag{4.1}$$

where d is the thickness of the film, and $R(E)$ and $T(E)$ are the reflectance and transmission spectra respectively.

4.2.3 Photoluminescence Spectroscopy

As discussed in Chapter 2, photoluminescence is a process of photon emission following photo-excitation. To study photoluminescence, a laser is typically used as a source of photons with energy greater than the bandgap of the semiconductor being probed. This laser excitation may be either continuous wave (CW) or pulsed, and the beam is directed at the sample in order to produce photoluminescence. The photons emitted from the sample are collected and may be analysed by simply counting (intensity measurements) or by spectrally resolving the photoluminescence to observe the energy of the photons emitted by the sample. These time-integrated (steady-state) experiments, are useful for identifying and characterising the electronic transition responsible for photon emission, and also determining the ratio of photons incident and photons emitted (photoluminescence quantum efficiency or PLQE). If a pulsed laser is used, the emitted photons can be time-resolved, allowing observations of photoluminescence transients following an excitation pulse. Time-resolved photoluminescence is an extremely useful characterisation tool for semiconductors, and particularly relevant for photovoltaics for several reasons: a) It can be used to measure the lifetime of charges in the excited state; a characteristic that should be maximised in order to efficiently extract charges. b) By modelling photoluminescence transients, the nature of recombination and charge-carrier dynamics in a semiconductor or device can be investigated. c) The effect of non-radiative recombination, which is usually detrimental in photovoltaic materials can be be characterised by analysis of the time-resolved photoluminescence.

4.2.4 Time-Correlated Single-Photon Counting

For time-resolved photoluminescence in general, a pulsed laser is typically used with a time period between pulses that is longer than the decay of photons from the excited state being investigated. One technique that can be used for time-resolved photoluminescence measurements is time-correlated single-photon counting (TCSPC). The principles are represented in Figure 4.7. A TCSPC setup uses a pulsed laser source which is directed

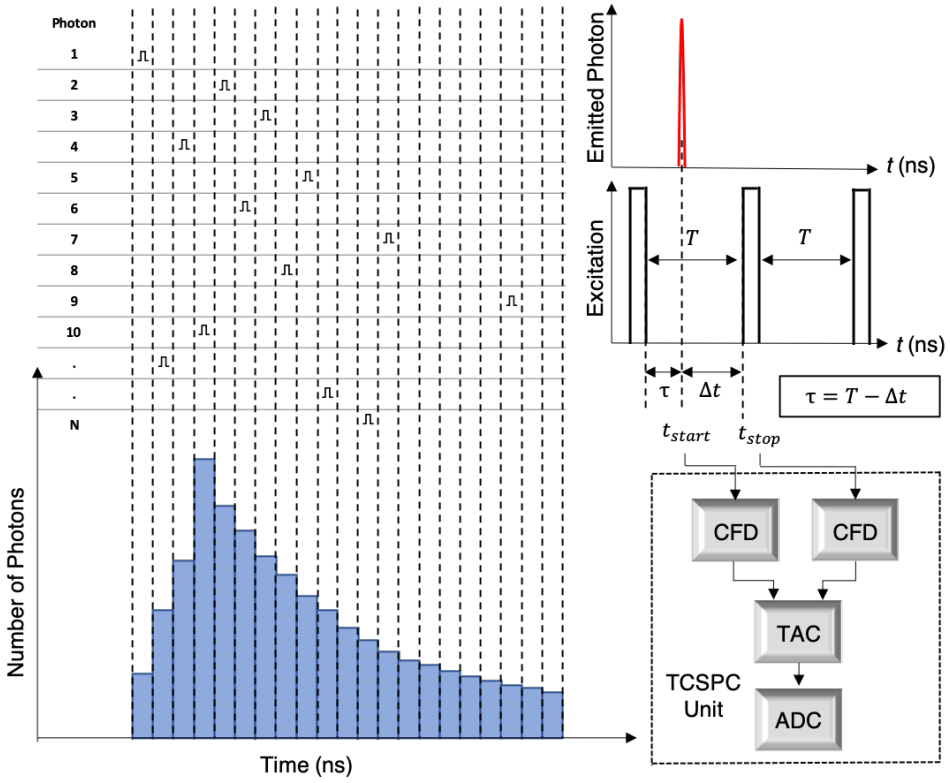

Figure 4.7: Time-correlated single-photon counting principle. The time delay between the arrival of the excitation pulse and photon emitted from the sample is recorded using 'reverse mode'. A histogram of time events is developed over many pulses.

at the sample. After a pulse excites the sample with many photons, the sample will emit many photons at different times following the pulse, which are directed towards a detector such as an avalanche photodiode (APD) or a photomultiplier tube (PMT). An example of a typical signal emitted by a sample is shown if Figure 4.7. Since the timescale of this signal is in nanoseconds, a problem arises if the emitted photons are to be received and processed by electronic detection equipment; there no possibility

to detect and time-resolve every photon following a single pulse. In fact, for typical repetition rates of pulsed lasers used for TCSPC (kHz-MHz), not even one photon from every pulse can be detected and registered. Instead, the emitted light from the sample must be filtered so that the rate of detection is less than one photon per pulse. Typically 1 photon per 100 pulses are detected [181]. The detector receives a photon from the sample, which is emitted via a random process. The signal is received by a constant fraction discriminator (CFD), measuring the relative time of the signal. This signal is then sent to a time-to-amplitude converter (TAC), producing a voltage ramp that is proportional to the time elapsed. The TAC essentially waits for another signal to be received and follows a similar process, except now the signal is the synchronisation signal of the excitation source (pulsed laser). The voltage stored by the TAC is proportional to the time difference between the detected emitted photon and the start of the next pulse from the excitation. By subtracting this time-difference value from the period of the laser pulses, the time delay between the excitation and emission is obtained. This delay time is recorded, and a histogram of time events is constructed over many recordings. This configuration is known as 'reverse mode' and is utilised by all TCSPC measurement systems [181]. This process overcomes the issue of the high repetition rate of the laser, compared to the response time of the electronics. Once the 'stop' signal has been received, the TAC has to reset and await the next signal from an emitted photon. If the TCSPC setup were instead to use the opposite approach and time between the excitation pulse and received photon, the TAC would not have time to register emitted photons due to the finite response time of the electronics. The time needed for the TAC to reset to zero is much greater than the time period of the laser pulses. Hence, by instead detecting emitted photons, which are filtered to arrive ~ 1 in every 100 laser pulses, the TAC has time to reset and initialise between each timing sequence. Under these conditions, the histogram faithfully reproduces the shape of the decay. However, if the rate of detection is increased too much, the histogram will become biased to shorter times [181] since only the first photon is observed.

For the studies in this thesis, a setup capable of performing both time-integrated and time-resolved photoluminescence measurements was used, shown in Figure 4.8. The optical excitation at 400 nm is provided by a tunable titanium:sapphire laser (Coherent

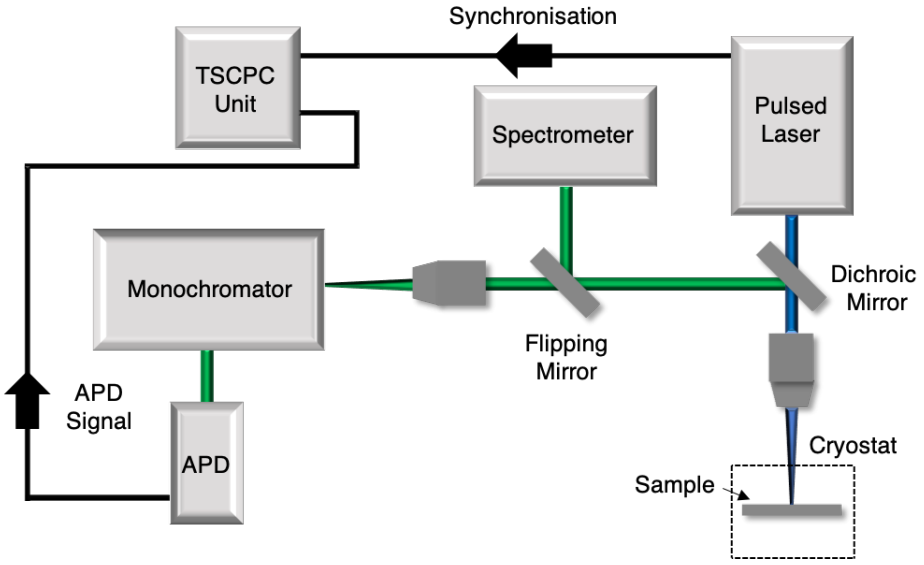

Figure 4.8: Experimental setup for photoluminescence measurements. A pulsed laser provides excitation source and the beam is directed through a dichroic mirror, then on focused on to the sample through an objective lens. The same objective lens collects the emitted light from the sample, after which the beam is reflected by the dichroic mirror. The beam can then be directed to a spectrometer (time-integrated measurements) or alternatively focused in to a monochromator for time-resolved measurements using the avalanche photodiode (APD). The APD signal and the synchronisation signal from the laser is connected to the time-correlated single-photon counting unit.

Chameleon Ultra II), in combination with a Coherent second-harmonic generator. A pulse picker is used to modulate the repetition rate lowering the pulses frequency down to 1 kHz. The temperature of the sample in the cryostat is controlled through an Oxford Instruments ITC503 unit and capable of cooling the sample to $\sim$ 11 K. The PL is collected through the objective and directed towards an APD for time-resolved photoluminescence. Alternatively, the collected beam can be directed towards a spectrometer (BWTek Glacier X) for time-intregrated studies. For the time-resolved measurements, the signal from the APD is sent to a Becker Hickl GmbH SP-140 TCSPC card, which time-resolves the measurements with a 40 ps resolution. The spectral window of the emission is selected using a Bentham M300 monochromator.

4.2.5 Combined Atomic Force Microscopy and Scanning Near-Field Optical Microscopy

In Chapter 7, apparatus is used that simultaneously performs atomic force microscopy (AFM) and scanning near-field optical microscopy (SNOM). Both these methods are categorised under scanning probe microscopy (SPM), since they utilise a 'probe' tip that scans the surface of the sample, recording data at different points. With SPM, nano-scale features can be resolved due to the high sensitivity and unique principles invoked. This section introduces the principles of both experimental techniques and describes how the combined system is utilised.

A schematic for an AFM system is shown in Figure 4.9. A probe tip is used to scan the

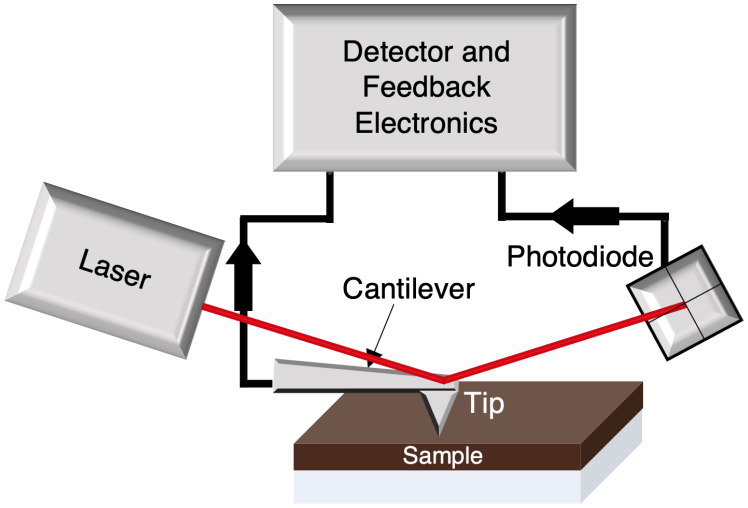

Figure 4.9: Atomic force microscopy. A scanning probe is used to scan the surface of the sample and is deflected by topological features. A laser is reflected from the top surface of the probe tip to a quadrant photodiode. Changes in the deflection of the tip can be recorded by the position of the laser beam on the photodiode.

surface of the sample, which is deflected as it passes over features of the surface topology. A laser beam is directed towards the tip and the reflection from the top surface of the tip is positioned on a segmented photodiode. Deflections of the tip are translated to deflections of the beam from the centre of the photodiode and can be recorded. An AFM system can operate in several different modes. In the case of 'contact' mode, the separation between the sample and the tip is minimal and the repulsive force between

the tip and the sample is essentially measured. In 'tapping', also called 'intermittent-contact' mode, an AC electrical signal is supplied to the tip, causing it to oscillate at a given frequency. The tip periodically contacts the sample and changes in the oscillating frequency can be measured. AFM can also be performed in 'non-contact' mode, where the tip only experiences the attractive force due to van der Waals forces. A graph of force against sample-probe distance is shown in Figure 4.10, including the regimes of contact, tapping and non-contact AFM modes [182].

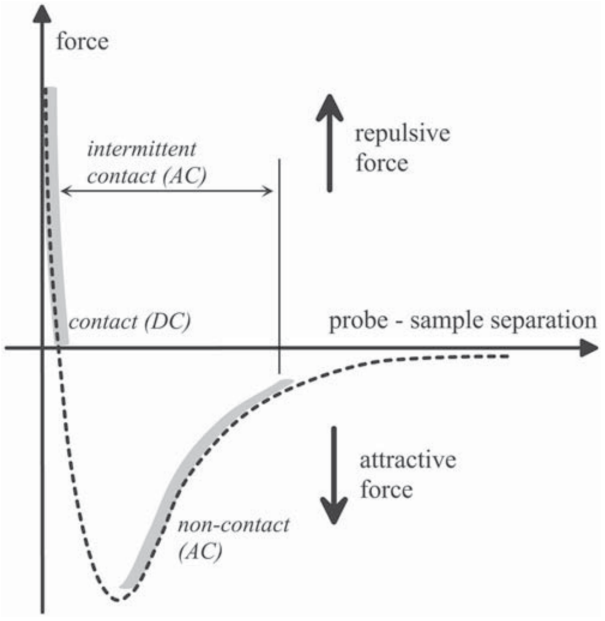

Figure 4.10: Atomic force versus sample-probe distance. Graph of forces between tip and sample as a function of sample-tip distance. Image taken from Ref. [182].

SNOM is another SPM technique that provides sub-diffraction limit resolution optical imaging. In this thesis, it is used for imaging photoluminescence intensity (see Chapter 2) of perovskite thin films on a nano-scale. When using SNOM, the resolution limit for far field microscopy can be overcome by utilising the detection of evanescent waves. In the SNOM measurements in this thesis, the excitation light source (a laser) is guided through an optical fibre and focused through an aperture integrated with the AFM tip with dimensions smaller than the wavelength of the laser, resulting in an evanescent field (or near-field) on the outgoing side of the aperture. The sample is scanned during the AFM measurement and the photoluminescence is simultaneously collected by a microscope

objective lens. A schematic of the combined AFM and SNOM system is shown in Figure 4.11.

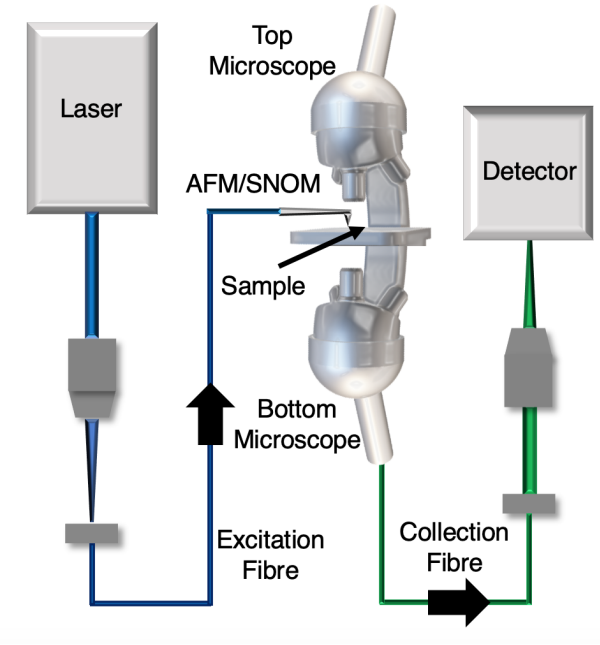

Figure 4.11: Combined atomic force and scanning near-field optical microscopy system. Schematic of the combined AFM and SNOM setup. Topology is recorded with the AFM electronics while the photoluminescence is collected with the microscope objective lens.

In Chapter 7, the system used for the combined AFM and SNOM measurments is a Nanonics Hydra Bio AFM system, used in tapping mode. The excitation beam is provided at 420 nm by a Coherent Chameleon Ultra II titanium:sapphire laser, coupled to the tip via an optical fibre. The photoluminescence is collected in near field configuration with a cantilevered optical fibre probe that scans the surface of the sample.

In Chapter 8, bright–field confocal photoluminescence microscopy is used to image PEDOT:PSS films. For this study, a Zeiss LSM 510 confocal laser-scanning microscope is used with a Coherent Enterprise II argon ion laser as an excitation source for the micro-scale PL mapping.

4.2.6 Spectroscopic Ellipsometry

Spectroscopic ellipsometry is a powerful technique used for characterising optical properties of materials. It is applicable to many different types of materials, and can be used

to determine properties such as the complex dielectric constant (or complex index of refraction), thickness and surface roughness of a material. From the dielectric function, the transmission and reflectance spectra of a sample can also be derived without the requirement of absorption spectroscopy. With the correct optical dispersion model for the dielectric function, these parameters can be determined with very high accuracy, due to the sensitivity of the technique.

The principle of ellipsometry is to use a linearly polarised light source, incident at an angle to the sample. As the electromagnetic radiation interacts with the material of the sample, the electric field component undergoes a phase shift and the wave becomes circularly polarised on reflection from the surface. Figure 4.12 shows the principle of ellipsometry.

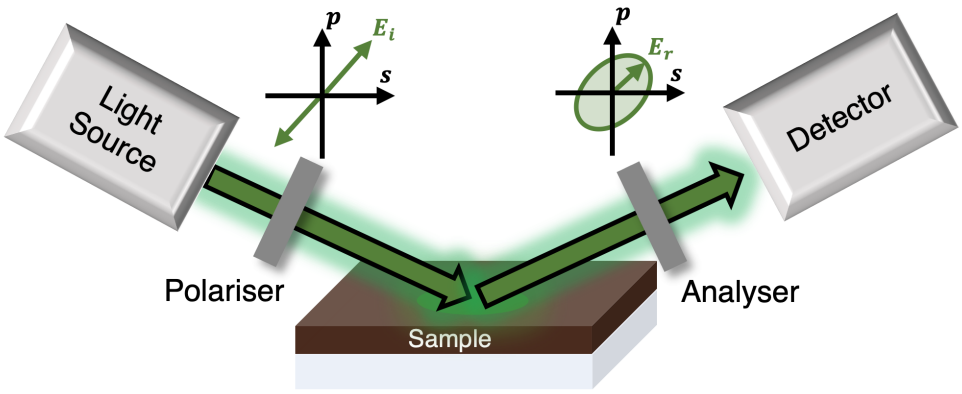

Figure 4.12: Spectroscopic ellipsometry. Light incident on the sample is linearly polarised by a polariser. The reflected light is circularly polarised and the degree of polarisation is measured by the detector, with use of an analyser. E_i and E_r denote the incident and reflected electric field, respectively.

The axes denoted with p and s in Figure 4.12 represent the perpendicular and parallel polarisation planes, respectively. The parameters obtained in ellipsometry measurements are usually denoted Δ and Ψ. The incident p-waves and s-waves may have a phase difference, δ between them. Following reflection of the incident beam on the sample, this phase difference will change, depending on the material properties. The parameter Δ is the difference between the phase difference before reflection from the sample, δ_1

and the phase difference after the reflection, δ_2. Hence,

$$\Delta = \delta_1 - \delta_2. \tag{4.2}$$

The value of Δ ranges from -180°to +180 °. In addition to the phase change between the p and s polarised light, the amplitudes of each wave will change upon reflection. The reflection coefficients R_p and R_s for the p-waves and s-waves are the ratio of outgoing wave amplitude to incoming wave amplitude. The parameter Ψ is the angle whose tangent is the magnitudes of the reflection coefficients, given by,

$$\tan \Psi = \frac{|R_p|}{|R_s|}. \tag{4.3}$$

Since the reflection coefficients are complex numbers (the p-waves and s-waves are electromagnetic plane waves), a complex number, ρ can be defined as,

$$\rho = \frac{R_p}{R_s}. \tag{4.4}$$

The complex parameter ρ can be written in terms of Ψ and Δ as

$$\rho = \tan \Psi e^{i\Delta} = \frac{R_p}{R_s}, \tag{4.5}$$

which represents the fundamental equation of ellipsometry [183]. If multiple measurements are made, the pseudodielectric constant can be obtained directly from the equation,

$$\langle \tilde{\varepsilon} \rangle = \sin^2 \theta_i \left[1 + \tan^2 \theta_i \left(\frac{1-\rho}{1+\rho} \right)^2 \right], \tag{4.6}$$

via mathematical inversion, where θ_i is the angle of incidence. However, typically a dispersion model that describes the dielectric constant is used to fit the data.

In Chapter 5, an oscillator model is used to fit the ellipsometry data from perovskite thin films. Oscillator models are particularly useful when there are relatively few features in the absorption spectrum of a sample. In the absorption spectrum of a material, there will be maxima at resonant frequencies where the material has higher probability to absorb the incident light at a given frequency. This is analogous to the resonance of

mechanical systems such as a mass on a spring, which absorbs energy from the driving force when it is close the resonant frequency of the vibrating system [183]. For an optical system, the incident light provides the driving force and the material experiences a resonant oscillation that absorbs this energy. There are several oscillator models which can describe the absorption of materials, and in Chapter 5 the Tauc-Lorentz oscillator model is used. In the Tauc-Lorentz oscillator model, the imaginary part of the dielectric constant is given by

$$\varepsilon_2 = \begin{cases} \sum_{i=1}^{N} \frac{1}{E} \cdot \frac{A_i E_i B_i (E-E_G)^2}{\left(E^2-E_i^2\right)^2+B_i^2 E^2} & \text{for } E > E_G \\ 0 & \text{for } E \leq E_G \end{cases} \tag{4.7}$$

Here, E_G is the bandgap, used as a coupled fitting parameter across all oscillators. The parameter A_i is the amplitude and B_i is the broadening of each oscillator peak centred at the energy E_i. The shape of the obtained function is shown in Figure 4.13.

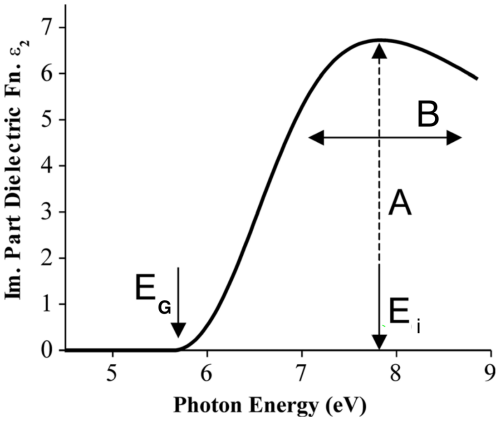

Figure 4.13: Tauc-Lorentz model. The imaginary part of the dielectric constant given by the Tauc-Lorentz model. Adapted from reference [184].

Once the parameters for ε_2 are obtained, ε_1 is found using the analytic solution of the Kramers-Kronig integration, given by, [185]

$$\begin{aligned}\varepsilon_1(E) =&\varepsilon_1(\infty) + \frac{AB}{\pi\xi^4}\frac{a_{\ln}}{2\beta E_i}\ln\left(\frac{E_i^2+E_g^2+\beta E_g}{E_i^2+E_g^2-\beta E_g}\right)\\ &- \frac{A}{\pi\xi^4}\frac{a_{\tan}}{E_i}\left[\pi - \tan^{-1}\left(\frac{2E_g+\beta}{B}\right) + \tan^{-1}\left(\frac{-2E_g+\beta}{B}\right)\right]\\ &+ 2\frac{AE_i}{\pi\xi^4\beta}E_g\left(E^2-\gamma^2\right)\left[\pi + 2\tan^{-1}\left(2\frac{\gamma^2-E_g^2}{\beta B}\right)\right]\\ &- \frac{AE_iBE^2+E_g^2}{E}\ln\left(\frac{|E-E_g|}{E+E_g}\right)\\ &+ \frac{2AE_iB}{\pi\xi^4}E_g\ln\left[\frac{|E-E_g|\left(E+E_g\right)}{\sqrt{\left(E_i^2-E_g^2\right)^2+E_g^2B^2}}\right]\end{aligned} \tag{4.8}$$

where,

$$\begin{aligned}a_{\ln} &= \left(E_g^2-E_i^2\right)E^2 + E_g^2B^2 - E_i^2\left(E_i^2+3E_g^2\right)\\ a_{\tan} &= \left(E^2-E_i^2\right)\left(E_i^2+E_g^2\right) + E_g^2B^2\\ \xi^4 &= \left(E^2-\gamma^2\right)^2 + \beta^2B^2/4\\ \beta &= \sqrt{4E_i^2-B^2}\\ \gamma &= \sqrt{E_i^2-B^2/2}\end{aligned} \tag{4.9}$$

The complex dielectric constant obtained by the model can then be compared with equation 4.6 from the ellipsometry data, and the difference between the modelled parameters and experimental data is minimised using a fitting procedure.

For the ellipsometry experiments in Chapter 5 a J.A. Woolam M-2000 spectroscopic ellipsometer was used to measure the induced polarisation change in the $MAPbI_3$ thin films for incident angles of 65°, 70°and 75°. The samples were packaged in an inert environment and measured immediately after opening to ambient conditions. CompleteEase (J.A. Woolam) software is then used for the data analysis and dispersion model fitting, as described above. The root mean squared error is calculated using the equation:

$$MSE = \sqrt{\frac{1}{3n-m}\sum_{i=1}^{n}\left[\left(N_{Exp_i}-N_{Mod_i}\right)^2 + \left(C_{Exp_i}-C_{Mod_i}\right)^2 + \left(S_{Exp_i}-S_{Mod_i}\right)^2\right]}, \tag{4.10}$$

where n is the number of wavelengths, m is the number of fitting parameters. The subscripts Exp and Mod denote the experimental data and the modelled data, respectively. The MSE is multiplied by 1000 so that an ideal value is equal to one. The parameters N, C and S are given by,

$$\mathrm{N} = \mathrm{Cos}(2\Psi) \tag{4.11}$$

$$\mathrm{C} = \mathrm{Sin}(2\Psi)\,\mathrm{Cos}(\Delta) \tag{4.12}$$

$$\mathrm{S} = \mathrm{Sin}(2\Psi)\,\mathrm{Sin}(\Delta). \tag{4.13}$$

4.3 Device Characterisation Techniques

This chapter describes the two electrical characterisation techniques used for the perovskite solar cells examined in Chapter 8. These methods serve as the standard methods for characterising solar cells and data data from such measurements is usually the subject of literature describing the design of new photovoltaic technology and also documentation for commercial photovoltaic products.

4.3.1 Current-Voltage Measurements Under Simulated Sunlight

Current–voltage measurements are typically used to determine the four major metrics of solar cells: the power conversion efficiency (PCE), the open-circuit voltage (V_{OC}), the short-circuit current density (J_{SC}), and the fill factor (FF). These parameters and the data obtained from these measurements are described in Chapter 2 and hence this section only describes the experimental setup. The apparatus is shown in Figure 4.14. To measure a current–voltage scan of a solar cell, the device is connected to a source–measure unit (SMU). The SMU provides a voltage (bias) to the device and simultaneously measures the current through the circuit. If the measurement is carried out in the dark, a regular diode response is obtained. For measuring the power generating capability of a solar cell, a light source that replicates the solar spectrum (AM1.5G) is used and the beam is directed towards the sample during the voltage scan.

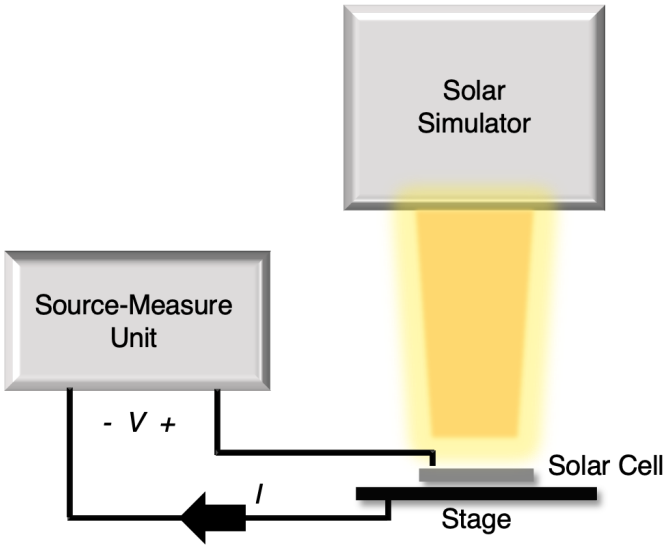

Figure 4.14: Apparatus for current–voltage measurements with a solar simulator. The postive and negative electrodes of the sample are connected to the source–measure unit. A solar simulator provides a light source that replicates the solar AM1.5G spectrum. A voltage bias is applied to the sample and the current through the device is recorded as a function of bias voltage.

For the work in this thesis, an Abet Technologies Sun 3000 Solar Simulator is used with a Keithley 2400 source-measure unit. A forward scan is used (short-circuit to forward-bias) from -1 V to +1 V with scan rate of $\sim$ 100 mV/s and an illumination of $\sim$ 1000 W/m^2.

It should be noted that the field of perovskite photovoltaics has moved away from using current–voltage scans as a means of determining the PCE, mainly due to hysteresis (see Chapter 3). To more accurately determine the efficiency of perovskite solar cells that exhibit hysteresis, a constant voltage is applied that approximately corresponds to the voltage of the maximum power point. The current output of the device is then read over the course of minutes in order to obtain a 'stabilised PCE' value. To determine the maximum voltage however, a current–voltage scan is required which reduces the accuracy of determining the value. A more accurate method is to employ a maximum-power point tracking system which uses an algorithm to update the voltage so that the maximum current is obtained over the course of the measurement.

4.3.2 External Quantum Efficiency

In addition to the four metrics PCE, V_{OC}, J_{SC} and FF, it is also useful to know the spectral response of the solar cell. This is evaluated by measuring the current output of the device in short-circuit conditions (J_{SC}) as a function of photon energy. This information is usually described in terms of external quantum efficiency (EQE), detailed in Chapter 2.

The experimental setup for EQE measurements is similar to that shown in the schematic in 4.14, except the solar spectrum light source is replaced with a monochromatic light source. The beam is directed towards the sample while scanning a range of wavelengths. The current output of the device is measured at each wavelength step and recorded. The EQE is then calculated using equation 2.23.

The EQE spectra in this thesis are acquired using a Bentham PVE300 QE system calibrated with a silicon reference detector.

Chapter 5

High-Energy Optical Transitions and Optical Constants of $CH_3NH_3PbI_3$ Measured by Spectroscopic Ellipsometry and Spectrophotometry

5.1 Introduction

Metal halide perovskites (MHPs) are a propitious group of materials for thin-film optoelectronics, with the research field still thriving and record solar cell efficiencies now reaching greater than 25% [12]. As photovoltaic devices begin to approach the theoretical efficiency limit for a single junction [54, 186–188], fine-tuning of the device structure is required for further optimisation. This can only be feasible with the assistance of optical simulations, which require accurate knowledge of the optical properties of device layers. Moreover, one of the most promising applications for commercialisation of MHPs are tandem solar cells, where the design also requires extensive optical modelling [29, 165, 189, 190]. The archetypal material for studying the properties of

MHPs is $CH_3NH_3PbI_3$ ($MAPbI_3$), which has been characterised scrupulously, revealing remarkable fundamental features for optoelectronics including high absorption coefficients ($\sim 10^4$–10^5 cm^{-1} at 2 eV) [108, 128, 191, 192], low exciton binding energies [68, 71, 79, 193], and small charge-carrier effective masses [71, 194, 195]. As a result, many other optoelectronic applications of MHPs have been developed, including lasers [196–201], light emitting diodes (LEDs) [202–205] and photodetectors [206–208].

Many studies have also been made to characterise the optical constants of $MAPbI_3$ thin films [191, 209–222], and also other MHPs [223–229] with varying results and analysis protocols. Optical constants are typically determined by fitting data from spectroscopic ellipsometry (SE) measurements to a dispersion model, which can then be compared with results from spectrophotometry (reflectance and transmission spectroscopy). With spectrophotometry measurements on MHPs, data for wavelengths of $\lambda < 300$ nm (photon energies of $E > 4$ eV) is usually omitted. This may be due to a) limitations of the measurement range of the equipment used, b) strong absorption of glass substrates and/or c) strong absorption of the material (for thicker films and single crystals), with the latter two resulting in a weak (noisy) signal for optical transmission. Hence, optical transitions at these photon energies are seldom discussed. Nevertheless, studies of this part of the spectrum are important for validating theoretical work regarding the band structure and ultimately understanding the fundamental properties of MHPs. Often the focus of band-structure calculations is to reproduce the bandgap energy of MHPs, however an accurate model should predict spectral features at all photon energies observable by experiment.

Here we use variable angle SE to determine the optical constants of a $MAPbI_3$ thin film over a wide spectral range. The ellipsometric data is modelled using Tauc-Lorentz oscillators for measurements from three different incident angles. We report on several optical transitions which are observed at ultraviolet photon energies in both SE data and spectrophotometry measurements. We present a simple step-by-step approach that can be used for utilising SE as a method for accurately determining the optical constants, thickness and surface roughness of MHP thin films.

5.2 Ellipsometry Measurements

We prepare $MAPbI_3$ via a one-step, gas-assisted spin coating method to achieve smooth uniform thin films [146]. This technique utilises the high pressure flow of inert gas on the surface of the film during the coating process, bypassing the need for anti-solvent quenching [147, 230, 231]. We use a precursor of PbI_2 and methylammonium iodide (MAI) (1:1) in a mixed solvent solution of DMF and DMSO at a concentration of 1M. Figure 5.1 shows the sample morphology from atomic force microscopy (AFM) and scanning electron microscopy (SEM). The film has a relatively uniform surface with grain size of $\sim$ 100 to 200 nm. We performed SE measurements on thin films of $MAPbI_3$ to

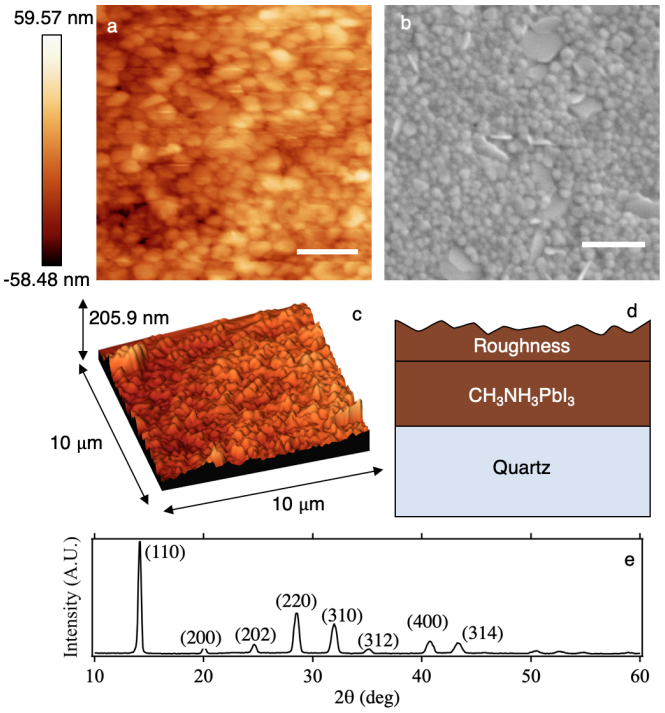

Figure 5.1: Characterisation of the $MAPbI_3$ thin films: a) AFM image. b) Top-view SEM image. c) 3D AFM topography. d) Schematic representation of the optical model. e) X-ray diffraction pattern. Scale bars are 1 µm.

obtain the Ψ and Δ values over the spectral range of 192 to 1696 nm, for three angles of incidence (65°, 70°, and 75°). The parameter Δ is the induced phase difference between the *s*- and *p*- polarised light and Ψ is the angle whose tangent is given by the ratio of the magnitudes of the reflection coefficients, $|R_s|$ and $|R_p|$ for the s and p polarisation planes, respectively, i.e. $\tan\Psi = |R_p|/|R_s|$ (see chapter 4). We ensure that the sample is measured immediately following exposure to ambient conditions, after being packaged in

an inert environment so that minimal degradation occurs prior to measurement. Figure 5.1e shows the X-ray diffraction pattern of the film in this condition, displaying a high degree of crystallinity and absence of peaks that indicate degradation.

5.3 Tauc-Lorentz Oscillator Model

To model the ellipsometry results, we firstly use a Cauchy film model to fit the data in the transparent region (> 800 nm), where oscillations due to interference are observed. The refractive index from the Cauchy dispersion model is given by:

$$n(\lambda) = A + \frac{B}{\lambda^2} + \frac{C}{\lambda^4}, \tag{5.1}$$

where A, B and C are the Cauchy coefficients to be fitted, and λ is the wavelength. This gives a good estimate for the thickness of the film, which is not fitted during the next phase. Subsequently, the Cauchy film model is parameterized to convert it to a basis-spline (b-spline) model which is used to fit the transparent region of the spectrum. The fit is then expanded to wavelengths below the bandgap, where the film is absorbing. The b-Spline model is then forced to be consistent with Kramers-Kronigs relations and fit to the data once again with updated parameters. Finally, the b-Spline model is parameterized to build an oscillator model with six Tauc-Lorentz oscillators. In the Tauc-Lorentz model, the imaginary part of the dielectric constant is given by equation 4.7. In the equation, E_G is the bandgap, used as a coupled fitting parameter across all oscillators. The parameter A_i is the amplitude and C_i is the broadening of each oscillator peak centred at the energy E_i. Once the parameters for ε_2 are obtained, ε_1 is found using the analytic solution of the Kramers-Kronig integration (equation 4.8) [185]. The resulting model for pseudo-optical constants can be fitted to the data for Ψ and Δ using equation 4.6 where θ_i is the angle of incidence and ρ is the induced polarisation change ($\rho = \tan(\Psi)e^{i\Delta}$). The parameters are fitted globally for three angles of incidence (65°, 70°, and 75°) over the wavelength range of 192 to 1696 nm. We incorporated the film thickness and surface roughness in the model (Figure 5.1d) and all parameters are updated to obtain the lowest possible MSE (mean squared error).

The Ψ and Δ data is shown in Figure 5.2, along with the fit from the Tauc-Lorentz oscillator model. A MSE value of 6.458 is achieved, indicating excellent agreement

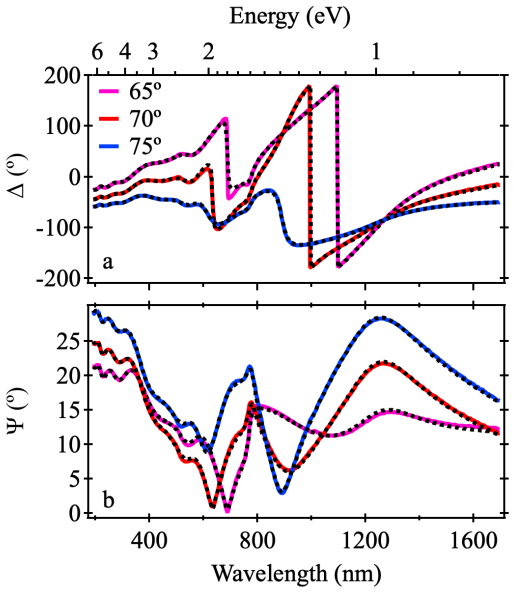

Figure 5.2: Polarisation data obtained from variable angle SE measurements. The dashed lines show the fits from the Tauc-Lorentz model.

between the model and data.We obtain a thickness value of 302.33 ± 0.086 nm, which is in agreement of the thickness obtained using profilometry (299 ± 7 nm). The roughness of the film is found to be ∼ 6.40 ± 0.036 nm, which is slighly lower than the RMS (root mean square) roughness value of 13 nm obtained by AFM (Figure 5.1a and c). It is important to factor the surface roughness, since it has a substantial impact on the determination of optical characteristics of the film, with larger values causing erroneous interpretation [232]. The fitting parameters obtained from the Tauc-Lorentz model are outlined in Table 1.

Table 5.1: Fitting parameters of the Tauc-Lorentz oscillators

Oscillator	Centre (eV)	B_i (eV)	A_i
E_0 (E_G)	1.574 ± 0.001	0.113 ± 0.0035	85.6887 ± 1.4232
E_1	2.540 ± 0.0054	0.905 ± 0.0260	15.2272 ± 1.2160
E_2	3.361 ± 0.0033	1.031 ± 0.0179	16.4492 ± 0.3863
E_3	4.651 ± 0.0089	1.375 ± 0.0496	5.5714 ± 0.2945
E_4	5.693 ± 0.0196	0.895 ± 0.0933	2.0886 ± 0.5220
E_5	6.601 ± 0.0921	1.360 ± 0.4059	3.5829 ± 1.3693
E_{UV}	8.312 ± 0.3858		44.4681 ± 8.0397

We find that six oscillators are required to minimize the MSE of the fit and reproduce

the data accurately. If fewer than six oscillators are used (four or five, for example), the fit does not capture all of the features of the Δ and Ψ curves (Figure 5.2a and b, respectively) and instead converges to oscillator parameters that provide an average value to account for several transitions. Only very slight reductions in the MSE can be obtained if more oscillators are used, and the amplitude of the additional oscillators have to be very low to achieve this. Therefore, we can conclude that any more or fewer than six main oscillators appears to create a non-physical model. A value of $\epsilon_\infty = 1.272 \pm 0.09$ is fitted to provide a dielectric constant at high energies, in order to prevent ε_1 from becoming zero following the application of the Kramers-Kronig transformation. The element E_{UV} is also included as an unbroadened oscillator to account for high-energy absorption, which effectively provides a 'tilt' to the dielectric constant. The bandgap value of $E_G = 1.574$ eV is determined as a coupled fitting parameter for all oscillators.

The optical constants determined from the analysis are presented in Figure 5.3. The

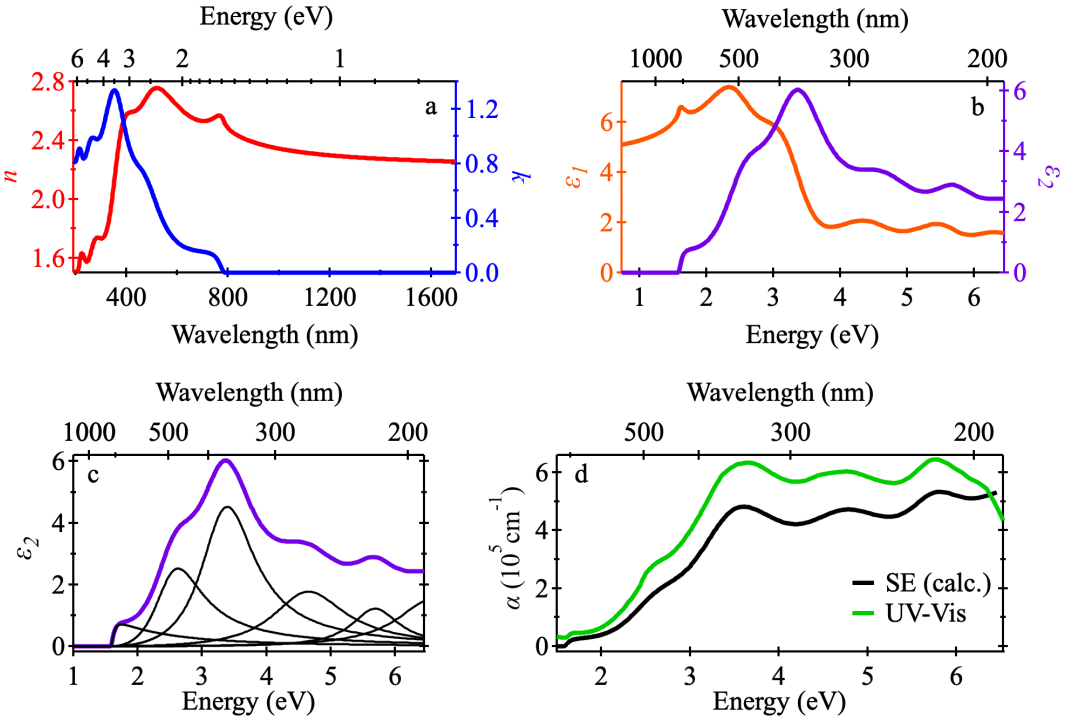

Figure 5.3: Optical constants determined from the SE data analysis: a) Refractive index (n) and extinction coefficient (k). b) Real (ϵ_1) and imaginary (ϵ_2) components of the dielectric constant. c) Tauc-Lorentz oscillators (black curves) used to model ϵ_2 (purple curve). d) Absorption coefficient calculated from SE data (black) and estimated from spectrophotometry data (green).

black curves in Figure 5.3c show the individual contribution from the Tauc-Lorentz oscillators to ε_2. Figure 5.3d shows the absorption coefficient, α derived from the extinction coefficient, k, calculated using the relation $\alpha = 4\pi k/\lambda$. We performed spectrophotometry measurements on a different $MAPbI_3$ thin film deposited on quartz to obtain an estimate for the absorption coefficient, which is overlaid with the calculated absorption coefficient in Figure 5.3d. For these measurements, a thinner film was deposited using a 0.5M solution to obtain a thickness of $\sim$ 110 nm, to ensure the transmission signal was strong enough to be detected at highly absorbing wavelengths.

The observed transitions in the absorbing region of the experimental α spectrum appear to corroborate with the modelled data from the ellipsometry measurements. For the SE-calculated absorption coefficient, the value at 2 eV is $\sim$ 4.6 x 10^4 cm^{-1}, which is in good agreement with previous work [108, 211, 217]. The absolute amplitude of the absorption coefficient obtained from spectrophotometry should not be considered as an accurate value for comparison, since scattered light from the sample is not accounted for. Instead, we use the data to compare the shape and position of the optical transitions. One major difference between the two absorption coefficients is position and relative amplitude of the highest energy peak. In the spectrophotometry data, it appears that the two highest energy peaks coincide, creating a high energy shoulder at $\sim$ 6.3 eV in the peak observed with a maximum at $\sim$ 5.8 eV. In the SE data however, it appears that the highest energy peak is blueshifted in comparison, with the maximum lying outside of the measurement range, with the Tauc Lorentz oscillator associated with this peak centered at 6.52 eV (Table 1).

5.4 Critical-Point Analysis

To investigate the optical transitions in $MAPbI_3$, we used critical-point (CP) analysis to accurately determine the transition energies. The CP model gives the following expression for the second derivative of the complex dielectric constant for any given excitonic transition, j:

$$\frac{\mathrm{d}^2\varepsilon}{\mathrm{d}E^2} = 2A_j \mathrm{e}^{i\varphi_j} \left(E - E_{Cj} + i\Gamma_j\right)^{-3}. \tag{5.2}$$

The energy of the transition is given by E_{Cj}, the broadening is Γ_j, the amplitude is A_j, the phase is φ_j, and i is the imaginary unit. This equation is used to fit the real and imaginary parts of the dielectric function, as shown in Figure 5.4. The transition energies

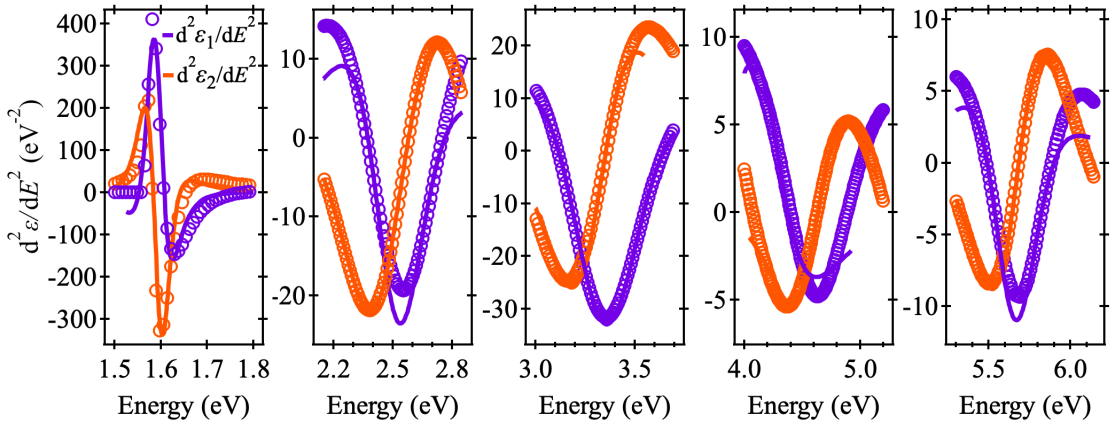

Figure 5.4: Critical-point analysis of the dielectric constant. The solid lines show the fitting of equation 5.2.

obtained from this analysis are $E_{C0}(E_G) = 1.592 \pm 0.001$ eV, $E_{C1} = 2.49 \pm 0.072$ eV, $E_{C2} = 3.31 \pm 0.03$ eV, $E_{C3} = 4.39 \pm 0.46$ eV $E_{C4} = 5.645 \pm 0.01$ eV. We could not extract an energy associated with the transition at the high energy limit of the dispersion, since it is not fully captured by the measurement range.

The three transitions E_{C0}, E_{C1} and E_{C2} are commonly identified [189, 213, 217], however, E_{C3} and E_{C4} are not often observed or remarked on. Our obtained value for the bandgap is similar to those previously determined [191, 192, 217, 222], which has been attributed to a direct transition at the R symmetry point of the Brillouin zone [191, 216]. Shirayama *et al.* reported the analysis of SE measurements over a wide spectral range, where several weak transitions are observed at high energies [191]. In their work, critical points are identified at 2.53 and 3.24 eV in the dielectric function for $MAPbI_3$ and are assigned to the direct optical transitions at the M and X points in the pseudocubic Brillouin zone, respectively. Our values for E_{C1} and E_{C2} lie reasonably close to these transition energies and hence, are also likely to have the same origin.

The spectral features at higher energies indicate either transitions between energy bands deeper than the first conduction and valence band or transitions occurring at points other than the M and X points of the Brillouin zone. Leguy *et al.* performed SE

measurements for photon energies up to 5.5 eV and fitted the data to determine critical-point energies of 1.62, 2.55, 3.31, 4.55, and 10 eV for single crystals of $MAPbI_3$ but slightly different values of 1.61, 2.5, 2.85, 3.38, and 6.97 eV for thin films.[216] In the study, the authors use quasi-particle self-consistent GW (QS-GW) calculations to derive optical constants up to photon energies of 10 eV, which are in good agreement with experimental data within in the spectral range of the measurements. In the calculated extinction coefficient spectrum, peaks are also predicted at $\sim$ 5.5 and 6.7 eV, which are not captured in their ellipsometry experiments, but are relatively close to the transitions observed in our experiments here [216]. Ndione and colleagues observed the transitions at $\sim$ 4.6 and 5.8 eV in the dielectric constant from SE measurements, but only included the transition at 4.6 eV in the critical-point analysis.[221] Demchenko *et al.* performed SE measurements on $MAPbI_3$ and extracted a dielectric constant that closely matches our obtained function, including the high energy features, likely originating from Γ point transitions [220]. As a result, we suggest that the transitions associated with E_{C3} and E_{C4} are associated with transitions at the Γ point of the Brillioun zone. Guerra and colleagues also observed the transitions at $\sim$ 4.6 and 5.8 eV via SE but did not measure spectrophotometry data beyond 5 eV [222]. In all the above studies, the highest energy optical transition is not investigated via spectrophotometry measurements in addition to SE.

5.5 Conclusions

In conclusion, we have used spectroscopic ellipsometry (SE) and spectrophotometry to identify optical transitions in $MAPbI_3$ thin films and have determined the optical constants over a wide spectral range. We have shown how the SE data can be fitted with a Tauc-Lorentz dispersion model with six oscillators, using parameters that can be physically justified. These analyses are critical for constructing optical models for use in designing structures such as tandem solar cells. We have used critical-point analysis to show transitions at 1.59, 2.49, 3.31, 4.39 and 5.65 eV from the SE data, which is in excellent agreement with results from spectrophotometry. The transitions at 4.63 and 5.88 eV are not usually investigated due to experimental limitations and provide important

information relating to the band structure of $MAPbI_3$ and the potential applications of the material. Although their origin remains unclear, previous studies allude to Γ-point transitions and further theoretical work should be carried out to fully understand the nature of these transitions and assist in accurately determining the fundamental physical characteristics of metal halide perovskites.

5.6 Contributions

The author fabricated the samples and performed the ellipsometry measurements and analysis. Giacomo Piana assisted with the AFM imaging. The content of this chapter has been accepted for publication, and parts of the text have been included verbatim.

Chapter 6

Disorder-Induced Trapping of Free Carriers and Excitons in Lead Halide Perovskites

6.1 Introduction

Photovoltaics based on lead halide perovskites (LHPs) are a promising technology for solar energy generation, with record efficiencies exceeding 24 % [12]. As a result, a vast array of methods have been employed to investigate the optoelectronic properties of the materials. Studies have revealed highly desirable properties such as long charge-carrier diffusion lengths (> 1 μm) [17, 100, 108], owed to slow electron-hole recombination and high carrier mobilities [107, 109–112, 233]. Despite this, there still exists a number of varying perspectives regarding the fundamental physical properties of LHPs. Specific examples include the contribution of excitons to the photoexcited states at different temperatures [87, 234–236], the nature of the band structure [78, 237], transitions during generation and recombination processes, the effect of trap states and defects [101, 238], and the understanding of device operating principles [239, 240]. Many studies have been carried out from which the binding energy of excitons in LHPs can be inferred, with values ranging from 2 meV to $>$ 60 meV [71, 72, 79–81] at room temperature for

$CH_3NH_3PbI_3$ ($MAPbI_3$) or similar materials. Reports of intermediate values for the exciton binding energy describe a picture of photogeneration of both excitons and free carriers at room temperature, with a ratio of $\sim 1 : 10$, respectively [70]. Drude-like terahertz photoconductivity spectra [15, 75] and microwave photoconductance [16, 80] at room temperature confirms the presence of free carriers in LHPs. Hence, free charge carriers are well agreed to be the primary photoexcited species in these materials at typical operating conditions for PV [69–72], allowing for successful use of perovskites such as $MAPbI_3$ for the planar solar cell architecture. In contrast, recent studies have suggested that excitons play a significant role in the recombination dynamics, with evidence of localisation and trapping of excitons [87, 234–236]. Many schemes have been proposed that describe the slow photoluminescence decay dynamics in terms of trap-assisted recombination [76, 100, 101]. However, there currently remains a lack of agreement among different models concerning the recombination mechanisms present in LHPs. Deeper trap states (> 50 meV) can originate from defects, likely related to lead and iodine [241, 242]. Iodine ions are known to be mobile within $MAPbI_3$ and the associated defects can be annihilated [114] or dispersed [116] by light irradiation. Therefore, following exposure of the film to laser excitation for several minutes in vacuum, shallow trap states become the principal cause of charge trapping, produced by spatial and temporal variations of the bandgap [192, 243–245] or shallow defect states [238, 246].

6.2 Temperature-Dependent Electronic Bandgap and Exciton Binding Energy

We prepare polycrystalline $MAPbI_{3-x}Cl_x$ thin films and measure the absorption coefficient as a function of temperature (see chapter 4), shown in Figure 6.1. We model the optical absorption using Elliott's theory for near band-edge optical absorption in direct-bandgap semiconductors [51]. Elliott's theory describes the intensity of optical absorption of semiconductors as a contribution from both exciton and band-to-band transitions (equation 2.9). This allows us to extract the exciton binding energy E_B and the bandgap energy E_G across the entire temperature range. The absorption at 290 K (Figure 6.1a) shows a smooth absorption onset around 1.55–1.65 eV, which is the

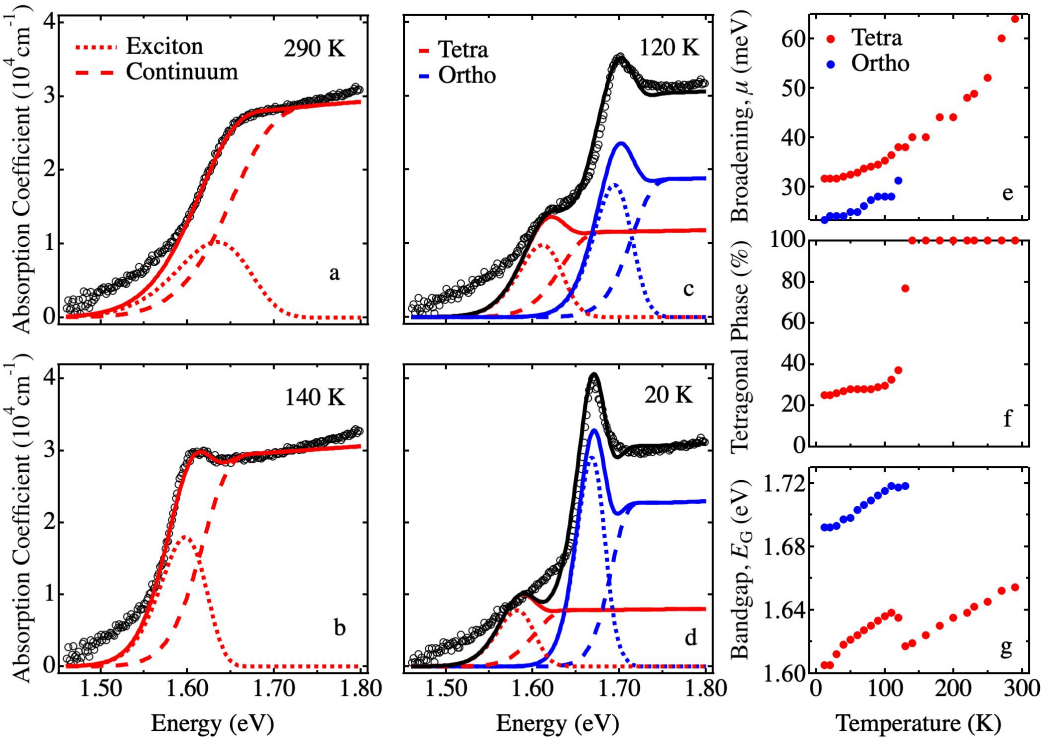

Figure 6.1: Absorption coefficient for $MAPbI_{3-x}Cl_x$ and results from Elliott's theory. (a-d) Absorption coefficient for $MAPbI_{3-x}Cl_x$ for different temperatures. Elliotts theory reveals the respective contributions from exciton and free-carrier transitions. **(e)** Broadening parameter, μ used in the absorption modelling as a function of temperature. **(f)** Percentage of total absorption from tetragonal phase $MAPbI_{3-x}Cl_x$. **(g)** The electronic bandgap, E_G, as a function of temperature.

expected optical bandgap for $MAPbI_{3-x}Cl_x$. At this temperature, the absorption reduces exponentially with decreasing photon energy. To account for this disorder-induced band-tail and also the homogenous broadening, we convolve the function from Elliott's theory with the lognormal distribution [247]:

$$f(E,\sigma,\theta,\mu) = \frac{1}{\sigma\sqrt{2\pi}}\frac{1}{E-\theta}\exp\left(\frac{-\left(\ln\left(\frac{E-\theta}{\mu}\right)\right)^2}{2\sigma^2}\right) \tag{6.1}$$

where σ is the shape parameter that accounts for the low energy tail introduced by structural disorder and μ is the broadening parameter, representing temperature-dependent electron-phonon coupling. We choose σ as a constant for all temperatures to simplify the model and μ is varied for each temperature. To represent the delta function for exciton transitions, a single point is created that is scaled by the products terms in the equation

and convolved with the function mentioned below. The step function for continuum absorption is implemented algorithmically by setting the value equal to $\sqrt{(E - E_G)}$ for energies above the bandgap and zero elsewhere.

As the temperature is reduced, a maximum in absorption close to the band-edge emerges, indicative of exciton transitions (Figure 6.1b). The absorption maximum becomes narrower and more intense relative to the free-carrier absorption, following a decrease in the homogeneous broadening, $\mu(T)$, caused by electron–phonon coupling, as shown in Figure 6.1e. The bandgap is found to increase linearly with temperature between 140 and 290 K, also in agreement with prior studies [96, 247]. This is not typical of crystalline inorganic semiconductors such as Ge, Si, and GaAs that follow the opposite trend [248]. Previous theoretical work has indicated that this is due to the stabilisation of band-edge states, following thermal expansion of the lattice [249]. A value of ∼20 meV is obtained for the exciton binding energy in the temperature range wherein only the tetragonal phase is present, which is consistent with several values previously found from fitting of the Elliott theory to absorption data [81, 107]. This value is constant across the temperature range of the tetragonal phase (∼140–290 K), except for 290 K where it is found to decrease slightly. At temperatures below 140 K, evidence for a coexistence of tetragonal and orthorhombic structural phases has been shown by several previous studies [67, 69] We find that the observed spectra at lower temperatures are a superposition of absorption from the two phases, as shown in Figures 6.1c–d. Even at 20 K, the model is unable to reproduce the experimental data if only absorption from the orthorhombic phase is considered. At this temperature, we find that ∼25 % of the relative signal intensity appears to originate from the tetragonal phase to account for the shape of the absorption (Figure 6.1f). Results from the model show that upon decreasing temperature, the exciton binding energy changes abruptly for both phases around 120–140 K, to a value of ∼23 meV for the temperature range of 20–120 K. It is therefore concluded that the exciton binding energy is almost temperature-independent, except for changes due to the structural phase transitions. The small difference in the exciton binding energy between the orthorhombic and tetragonal phases is in agreement with previous reports [107, 128, 250]. Similar to the exciton binding energy, the bandgap for

both phases increases rapidly during the phase transition (120–140 K) before gradually decreasing as the temperature is further reduced.

6.3 Electron–Phonon Coupling

This trend is also observed clearly in the photoluminescence versus temperature, shown in Figure 6.2a. The shape and energy of the photoluminescence as a function of tem-

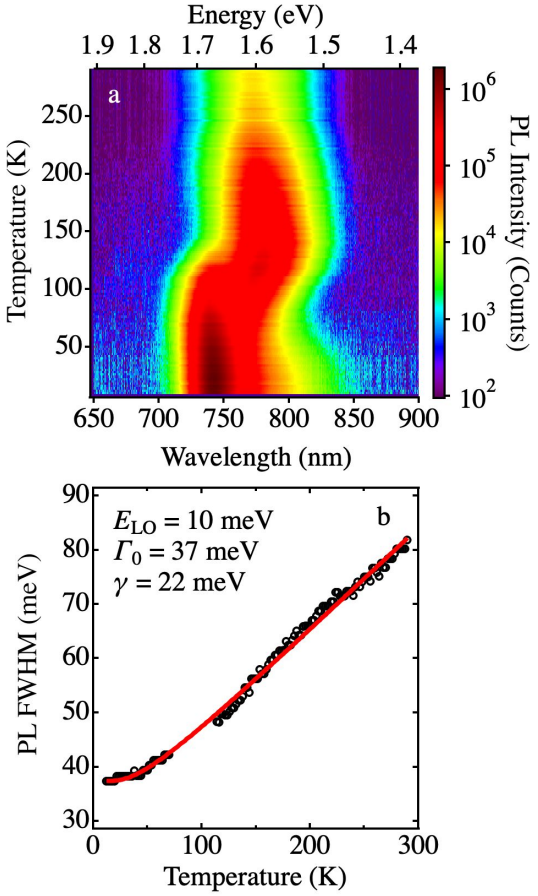

Figure 6.2: Steady-state photoluminescence of $MAPbI_{3-x}Cl_x$. **(a)** Steady-state photoluminescence spectra of $MAPbI_{3-x}Cl_x$ between 20 and 290 K. The photoluminescence intensity is in log-scale and shows emission from two transitions at the lower temperature range, attributed to the two different crystalline phases. **(b)** The linewidth of the steady-state photoluminescence as a function of temperature. The red line shows the fit of equation 6.2 to the data.

perature is similar to that previously reported [75, 243, 251]. The maximum of the photoluminescence redshifts with decreasing temperature, following the trend of the

absorption due to the non-Varshni behaviour of the bandgap (Fig 1g). Below the temperature of the phase transition (< 140 K) the orthorhombic phase photoluminescence maximum begins to emerge, and dual emission is observed even at temperatures below 100 K. At 20 K, the orthorhombic photoluminescence appears as a tail at longer wavelengths due to the lower intensity emission. This corroborates with the evidence of a phase coexistence at low temperatures from the absorption modelling. The linewidth of the photoluminescence measured at full width at half maximum (FWHM) increases with temperature for the $MAPbI_{3-x}Cl_x$ as shown in Figure 6.2a. The broadening for the tetragonal phase appears to be homogeneous, due to the scattering of charge carriers by phonons that increase the linewidth of the photoluminescence. Electron–phonon coupling in perovskites such as $MAPbI_{3-x}Cl_x$ has been previously studied, with differing conclusions drawn about the nature of the interactions [82, 252–254]. It was previously shown that due to the polar nature of LHPs such as $MAPbI_3$, the dominant mode is the longitudinal optical (LO) phonon via Fröhlich interactions with electrons [253, 255]. As a result, the linewidth broadening as a function of temperature $\Gamma(T)$ can be fitted with the equation,

$$\Gamma(T) = \Gamma_0 \frac{\gamma}{e^{\frac{E_{LO}}{k_B T}} - 1} \tag{6.2}$$

where Γ_0 is the linewidth at 0 K, γ is the strength of the Fröhlich coupling and E_{LO} is the energy of the LO phonon. Since $MAPbI_{3-x}Cl_x$ undergoes a phase transition around 140 K, we observe emission from two transition lines around this temperature and hence cannot accurately determine the linewidth for the tetragonal phase below this temperature. However, at low temperatures we can consider the approximate value of the linewidth of the orthorhombic phase photoluminescence maximum, assuming that the same phonon mode is dominant in both phases. The expected trend with temperature for the linewidth broadening via Fröhlich interactions is observed, as shown in Figure 6.2b, yielding a value of 10 meV for E_{LO}, which is similar to those previously found experimentally and from results of calculations [251–253]. The inhomogeneous broadening Γ_0 is found to be 37 meV, which again is similar to previously obtained values [251–253]. The Fröhlich coupling strength, γ is found to be 22 meV, which is slightly lower than

typically stated values for $MAPbI_{3-x}Cl_x$, indicative of weaker electron–phonon coupling in our sample. The Bose–Einstein dependence of the photoluminescence linewidth on temperature is similar to that of the broadening parameter, $\mu(T)$ in Figure 6.1e, used in the model for the absorption coefficient, suggesting that the same electron–phonon interactions are responsible for broadening of both emission and absorption.

6.4 Model for Trapping and Re-excitation

In order to interpret the time dependence of the photoluminescence, we construct a model to account for the carrier kinetics based on a system of coupled differential equations. Under non-resonant laser excitation of intensity L, a density $N(0)$ of photogenerated species is produced. This total concentration of species consists of the sum of free electrons in the conduction band, having density n and free excitons, with density x, so that the relation $N(0) = n + x$ holds. We postulate the presence of an intraband trap state for electrons and excitons at energy $E_T = E_G - \Delta E$, where ΔE is the difference in energy between the bandgap and energy level of the trap state. An electron from the conduction band or an electron bound in an exciton can then be trapped into these states that have a density N_T, contributing to the total concentration of trapped electrons that we indicate by $n_T + x_T$. Since charge neutrality must be conserved, the number of total photogenerated free holes in the valence band will be at any time $h = n + n_T$. A detailed kinetic model accounts for all the processes that we assume to govern the recombination in $MAPbI_{3-x}Cl_x$ and we describe such a model with the series of ordinary differential equations presented below:

$$\frac{dn}{dt} = -k_f n^2 + k_d x - k_{eh} n h - k_1^n \left(N_T - n_T - x_T\right) n + k_2^n n_T \tag{6.3}$$

$$\frac{dn_T}{dt} = k_1^n \left(N_T - n_T - x_T\right) n - k_2^n n_T - k_3^n n_T h \tag{6.4}$$

$$\frac{dx}{dt} = k_f n^2 - k_d x - k_x x - k_1^x \left(N_T - n_T - x_T\right) x + k_2^\chi x_T \tag{6.5}$$

$$\frac{dx_T}{dt} = k_1^x \left(N_T - n_T - x_T\right) x - k_2^x x_T - k_3^x x_T \tag{6.6}$$

The electron–hole recombination is described by $k_{eh}n^2$, where k_{eh} is the bimolecular recombination rate, and the free-exciton recombination is given by $k_x x$, where k_x is the radiative rate for excitons. The term $k_f n^2$ represents the exciton formation and $k_d x$ represents the exciton dissociation, both appearing in equations 6.3 and 6.5. The parameters k_1^n, k_2^n and k_3^n determine the electron trapping, re-excitation into the conduction band and depopulation into the valence band, respectively. The values k_1^x, k_2^x and k_3^x represent the analogous rates for excitons. The transitions between excited and trap states are mediated by phonon absorption and emission, with the rates of the processes determined by a Bose–Einstein distribution with temperature. Firstly, excitons and free-carriers can non-radiatively relax to trapped states by phonon emission. This is described by decay rate k_1:

$$k_1 = r_1 \left(e^{\left(\frac{E_{\mathrm{ph}}}{k_{\mathrm{B}}T}\right)} - 1 \right)^{-\frac{E_{\mathrm{bar}}}{E_{\mathrm{ph}}}} \left(\frac{e^{\left(\frac{E_{\mathrm{ph}}}{k_{\mathrm{B}}T}\right)}}{e^{\left(\frac{E_{\mathrm{ph}}}{k_{\mathrm{B}}T}\right)} - 1} \right)^{\frac{E_{\mathrm{bar}}+\Delta E}{E_{\mathrm{ph}}}} \tag{6.7}$$

where k_B is the Boltzmann constant, r_1 is a rate constant that relates to the efficiency of the process, $\left(e^{\left(\frac{E_{\mathrm{ph}}}{k_{\mathrm{B}}T}\right)} - 1 \right)^n$ is the probability of an carrier to absorb n phonons of energy E_{ph} to firstly overcome the barrier energy E_{bar} and $\left(\frac{e^{\left(\frac{E_{\mathrm{ph}}}{k_{\mathrm{B}}T}\right)}}{e^{\left(\frac{E_{\mathrm{ph}}}{k_{\mathrm{B}}T}\right)}-1} \right)^m$ gives the probability of an carrier to emit m phonons of energy E_{ph} and non-radiatively relax to the trap with a depth of ΔE. Furthermore, the opposite process can occur by excitation from the trap state to a bright state with a rate k_2 given by:

$$k_2 = r_2 \left(e^{\left(\frac{E_{\mathrm{ph}}}{k_{\mathrm{B}}T}\right)} - 1 \right)^{-\frac{E_{\mathrm{bar}}+\Delta E}{E_{\mathrm{ph}}}} \left(\frac{e^{\left(\frac{E_{\mathrm{ph}}}{k_{\mathrm{B}}T}\right)}}{e^{\left(\frac{E_{\mathrm{ph}}}{k_{\mathrm{B}}T}\right)} - 1} \right)^{\frac{E_{\mathrm{bar}}}{E_{\mathrm{ph}}}} \tag{6.8}$$

where r_2 is the rate constant that characterises the efficiency of the process. For the case of excitons, ΔE is replaced with $(\Delta E - E_B)$ to correctly represent the energy difference between the exciton state and the trap state. Finally, we also take into account non-radiative relaxation from the trapped states with decay rate k_3. A constant value for k_3 is used across the temperature range, since this value is very low in comparison to the other processes shown in Scheme 1. In these equations, the temperature dependence of

the rates is a function of the depth of the trap, ΔE and the energy required by carriers to become trapped, E_{bar}. In order to describe the observed photoluminescence decay, it is necessary to introduce one additional rate equation for the emitted photons p. This has the form:

$$\frac{dp}{dt} = k_{eh}n^2 + k_x x \tag{6.9}$$

For these calculations we use the Runga–Kutta numerical method to solve the system of coupled rate equations. The equilibrium values of the exciton and free electron–hole pair densities, x, n and h depend on the thermodynamic equilibrium conditions dictated by the Saha equation. Using the expression for the total photo-generated carriers N it is possible to write the generalisation of the Saha equation of p-doped semiconductors [256, 257]:

$$(n_e + n_T) \cdot n_e = An_x \tag{6.10}$$

where $A = \frac{v_x}{v_h v_e} e^{\left(\frac{E_B}{k_B T}\right)}$. Here, v_x, v_e and v_h represent the thermal frequency (related to the thermal wavelength) for excitons, electrons and holes respectively. If the density of trap states is zero, this expression reduces to the canonical form of the Saha equation $An_x = n_e^2$. In equations 6.3–6.6, two mechanisms are represented by the term $k_f n^2$ for the combination of free carriers into excitons and $k_d x$ for their dissociation. It has been proven that the static solution of these equations are the equilibrium values given by the Saha equation itself. For simplicity we consider the trap densities for our system to be zero, leading to a simplified version of the rate equations:

$$\frac{dn}{dt} = -k_f n^2 + k_d x - k_{eh} nh \tag{6.11}$$

$$\frac{dx}{dt} = k_f n^2 - k_d x - k_x x \tag{6.12}$$

It is possible to write the equilibrium condition in this case as:

$$(n + n_T)\, n = Ax \xrightarrow{\text{yields}} \frac{n_{\text{eq}}^2}{x_{\text{eq}}} = A \tag{6.13}$$

where we have used the condition $n_T = 0$ and the subscript indicates that the concentrations of electrons and holes reached the thermodynamic equilibrium. This will allow us to further simplify the rate equations as:

$$\frac{dn}{dt} = -r^0 n^2 + r^0 Ax - k_{eh} nh \tag{6.14}$$

$$\frac{dx}{dt} = r^0 n^2 - r^0 Ax - k_x x \tag{6.15}$$

We are then finally able to describe the formation and ionisation of excitons via a single rate r^0. The equilibrium condition is satisfied as long as the values for n and x given by the solution of the system of two rate equations satisfy the equation for n_{eq} and x_{eq} at any given time. This means that we can simply solve this system of two rate equations for different values of r^0 and then find the appropriate value of r^0 that accounts for the condition that the solutions for n and x satisfy equation 6.14. We find this value to be $r^0 = 10^{-4}$ cm^3 s^{-1}. These processes, along with all the other possible carrier transitions are outlined in Figure 6.3. For the bimolecular recombination rate in direct-bandgap semiconductors, the proportionality relation between the value of the recombination rate k_{eh}, the bandgap energy E_G and the temperature T is given by:

$$k_{eh} = k_{eh}^0 \frac{E_{\text{G}}^2}{\left(k_{\text{B}} T^{3/2}\right)} \tag{6.16}$$

where k_{eh}^0 is the proportionality factor and a global parameter in the model [258]. The radiative rate for excitons, k_x is also a global parameter and the trap-state density, N_T is a local free parameter for each temperature.

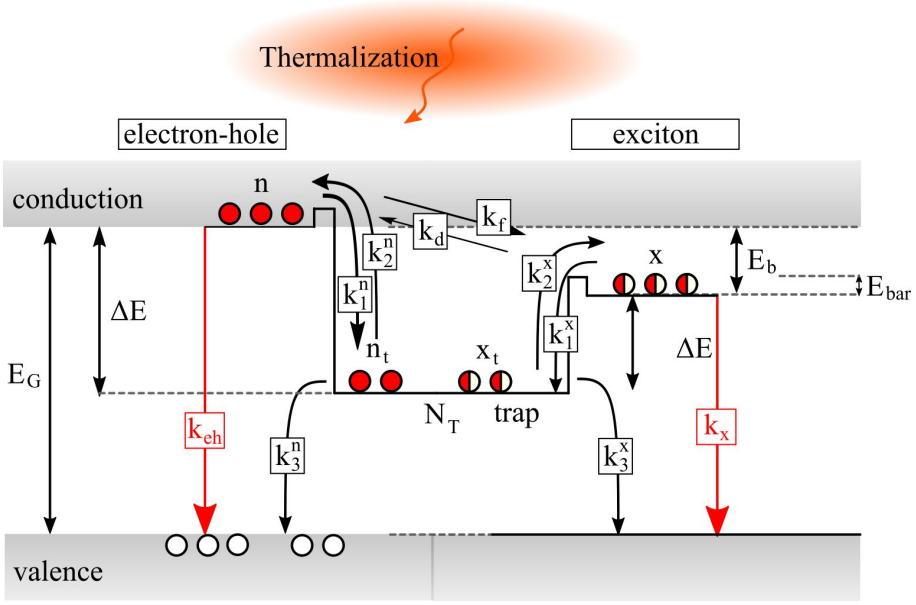

Figure 6.3: Excitation and recombination mechanisms in $MAPbI_{3-x}Cl_x$. Excitons can be formed and dissociated, with initial populations dictated by the Saha model. Free carriers and excitons can be trapped and re-excited from shallow traps via interactions with phonons, with rates depending on temperature.

6.5 Global Fits to Time-resolved Photoluminescence

We perform time-resolved photoluminescence measurements on $MAPbI_{3-x}Cl_x$ thin films for a range of temperatures and excitation fluences. The sample is placed in a cryostat under vacuum and illuminated with a 400 nm, 200 fs pulsed laser with a repetition rate of 2 MHz. At room temperature, the intensity and lifetime of the photoluminescence varies over the time period of the measurements due to light exposure of the sample at higher fluences, even under high vacuum. This effect has been previously attributed to defect motion in the sample due to mobile halide ions [114, 116]. Therefore, only temperatures between 20–260 K are considered, since for these temperatures the photoluminescence was found to be far more stable during several minutes of exposure due to lower thermal energy of ions.

For each temperature, after waiting for the photoluminescence to stabilise, the fluence of the laser is varied in order to generate photoexcited carrier densities $N(0)$ of 10^{15} and 10^{16} cm^{-3}. For the temperatures that show multiple maxima in the photoluminescence spectra, the time-resolved photoluminescence decays are recorded within a 20 nm window

centred on each spectral maximum separately. We solve our set of differential equations using iterative numerical methods to fit the normalised $\frac{dp}{dt}$ obtained from equation 6.9 to the corresponding experimental decays. The values of E_B and E_G obtained from the absorption modelling are used to calculate the Saha parameter A and the dependence of k_{eh} on both T and E_G (equation 6.16). We use the value of 10 meV obtained from the FWHM of the steady-state photoluminescence for the LO phonon energy to use in the expression for the phonon-assisted rates (equations 6.7 and 6.7).

Figure 6.4 shows the time-resolved photoluminescence data obtained from experiments along with the decays produced by the model. In order to understand the shape of the

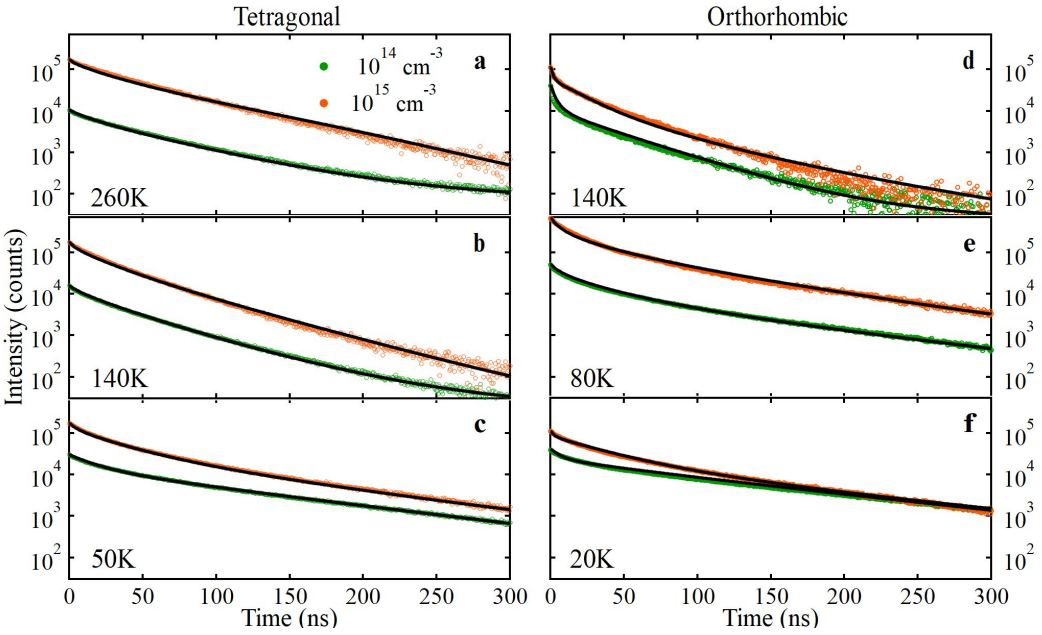

Figure 6.4: Time-resolved photoluminescence of $MAPbI_{3-x}Cl_x$ and modelled decays. **(a–c)** Time-resolved photoluminescence decays for the tetragonal phase. **(d-f)** Time-resolved photoluminescence decays for the orthorhombic phase.

observed decays, one must consider the interactions between free charges, excitons and trap states. Figures 6.5a and 6.5b show, as an example, individually the populations of both excited and trapped electrons (n, n_T) and excitons (x, x_T) at 140 K in the tetragonal phase. The decay pathways responsible for free-carrier and exciton trapping are responsible for a decrease in the overall lifetime of the luminescence. Decay of photogenerated charges into the trap states have rates proportional to $(N_T - n_T - x_T)$ for both free carriers and excitons and therefore will decrease when the trap states become

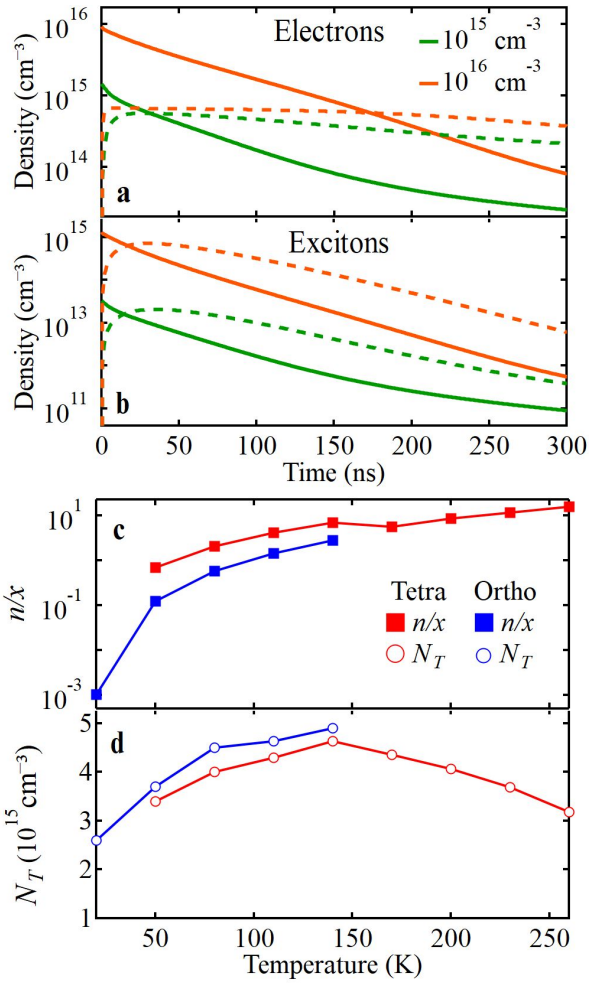

Figure 6.5: Results from the kinetic model of $MAPbI_{3-x}Cl_x$. **(a)** Calculated electron concentration $n(t)$ (solid lines) and trapped electron concentration $n_T(t)$ (dashed lines) for the tetragonal phase at 140 K. **(c)** Ratio of free carriers to excitons as a function of temperature for a fluence of 1016 cm-3. **(d)** Density of trap states N_T for the orthorhombic and tetragonal phase as a function of temperature.

saturated (Figure 6.5a). Hence, the initial fast trapping that is clearly visible in the first 25–30 ns becomes less dominant for higher excitation densities (Figures 6.4a–d). The dynamics at later decay times (25–30 ns onward) can be described as an interplay between bimolecular or exciton recombination, re-excitation of the trapped species into their excited states and recombination of trapped carriers. Since re-excitation into excited states and recombination are both proportional to the trapped carrier densities n_T and x_T, lower fluences will lead to an overall slower decay compared to higher fluences, which is observed for all temperatures. For free charges, this effect is summed with the dependence of the bimolecular recombination on the product of the electron and hole

densities, nh, as is possible to observe comparing the later component of the decays in Figure 6.4. In general, the decays for temperatures above the phase transition are dominated by the bimolecular recombination and the trapping of free charges, since they comprise more than 80 % of the photogenerated species, as shown in Figure 6.5c. When reducing the temperature, the relative proportion of excitons becomes more significant (Figures 6.4b–f). Close to the phase transition at ∼140 K, notably for the orthorhombic phase, the Saha relation dictates that the free-carrier and exciton populations are comparable for $N(0) \approx 10^{15}$ cm^{-3}, given our obtained value for the exciton binding energy and trap-state density, shown in Figure 6.6. However, at 10^{16} cm^{-3} the free electron–hole

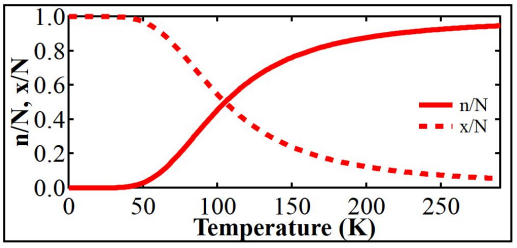

Figure 6.6: Result from the Saha equation The ratio of free carriers n and excitons x to the total photogenerated species N as a function of temperature.

pairs represent only 30% of the photogenerated charges at this temperature (Figure 6.4c). The decays for the intermediate temperatures are therefore described as a superposition of free-carrier and exciton dynamics, and the influence of the two species depends on the injected carrier density and trap-state occupancy. As the temperature is further reduced, the influence of the exciton dynamics increases, but the relatively high number of free electron–hole pairs affects the dynamics across the whole temperature range, with the notable exception of the orthorhombic phase at temperatures lower than 50 K (Figure 6.5c). At low temperatures, Phuong et al. observed evidence of charge transfer from the orthorhombic and tetragonal phase via the correlation of the photoluminescence decay time of the former to the rise time of the latter [69]. We do not observe such dynamics in $MAPbI_{3-x}Cl_x$, which is likely due to the larger grain size in our material (see Chapter 7) affecting the amount of charge transfer between phases. Figure 6.5d shows the density of trap states for free carriers and excitons in both the structural phases. We find that the trap-state density for both charge species increases with temperature from 20 K up to the phase transition. At these temperatures, there

is a coexistence of phases and an increase in disorder approaching the phase transition [255]. Within the material, traps exist as a distribution of states [243, 259] with different depths and barrier heights, resulting from a disordered energy landscape. In our model, we make a simplification by assuming a singular trap depth and barrier. The obtained values are presented in Table 6.1 and can be considered as the average values for the entire distribution of trap states.

Table 6.1: Fitting parameters from modelling the TRPL data.

Phase	k^0_{eh} ($cm^3\ s^{-1}$)	k_x (s^{-1})	ΔE (meV)	E_{bar} (meV)
Tetragonal	1.8 ± 0.1	2.8 ± 0.1	28 ± 1	1 ± 0.3
Orthorhombic	1.8 ± 0.1	2.8 ± 0.1	32 ± 1	1 ± 0.3

We find that the model requires a shallow trap energy ΔE of $\sim$ 30 meV to reproduce the experimental results accurately. Since non-radiative recombination of electrons from these states to the valence band requires a very large number of successive phonon interactions, the transition has a low probability [260]. This is accounted for in our model since the associated rates k_3^x and k_3^n for these processes are very low relative to other processes. The rates k_3^n and k_3^x are 10^{-12} $cm^3\ s^{-1}$ and 10^4 s^{-1} respectively, which are constant for all temperatures. This is in contrast to the rates for trapping (k_1^x and k_1^n), which are $\sim 10^{-9}$ $cm^3\ s^{-1}$ at low temperatures and $\sim\ 10^{-8}$ $cm^3\ s^{-1}$ at higher temperatures, and the rates for re-excitation (k_2^x and k_2^n), which are $\sim 10^5$ s^{-1} and $\sim 10^8$ s^{-1} for high and low temperatures respectively. The full temperature dependence of the rates for these phonon-mediated processes can be observed in Figure 6.7. This insight provides an explanation for the extension of the charge-carrier lifetimes, despite the presence of a direct bandgap that would otherwise provide a channel for fast radiative decay in lead halide perovskites.

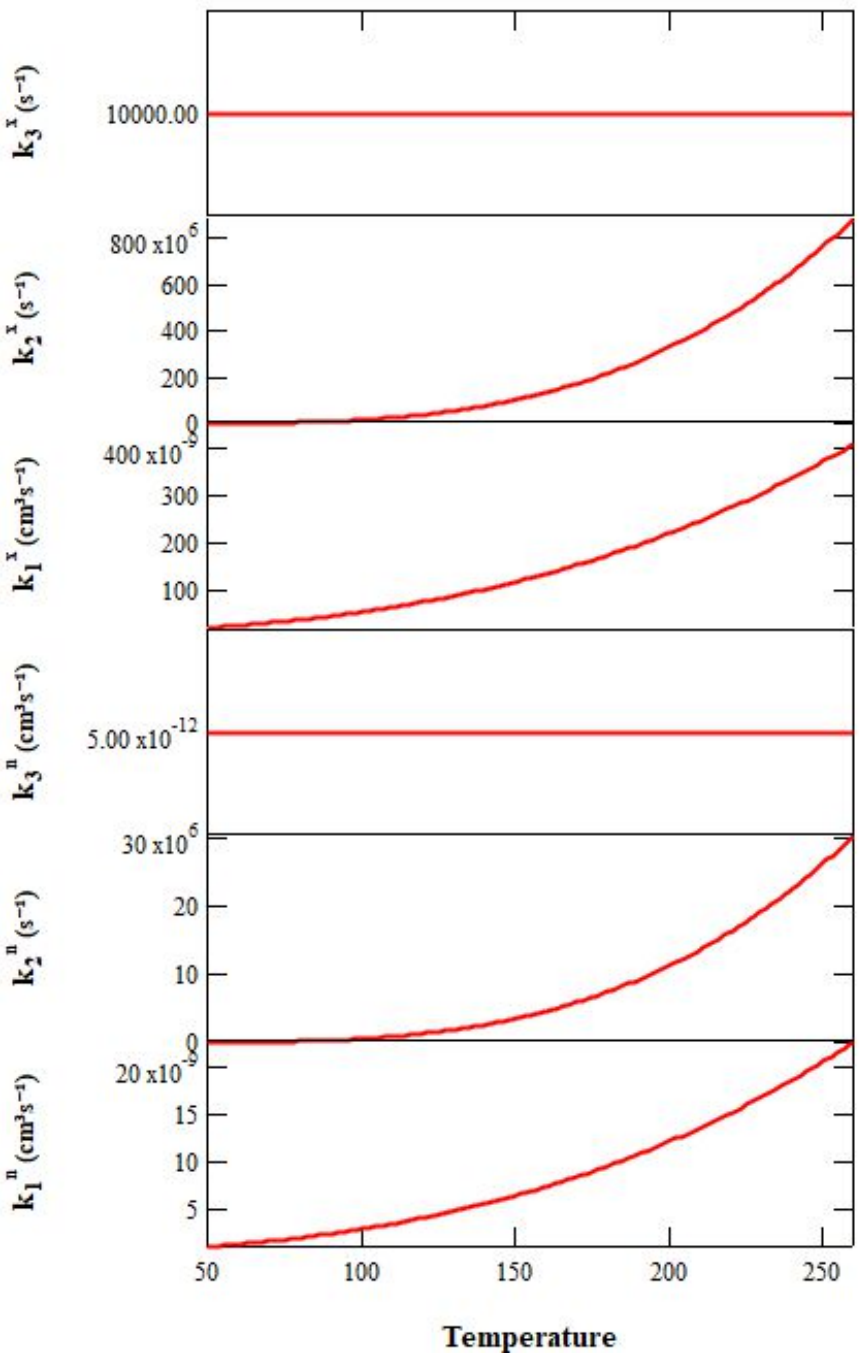

Figure 6.7: Phonon-mediated trapping rates. The rates for the phonon-mediated processes outlined in Figure 6.3 as a function of temperature.

6.6 Conclusion

In conclusion, following the use of Elliott's theory applied to absorption spectroscopy, we find that there is a coexistence of phases at low temperatures and have determined the exciton binding energy for low and high temperatures to be ∼23 and ∼20 meV, respectively. Coupling via Fröhlich interactions of electrons to LO phonons with an energy of 10 meV gives rise to broadening in the photoluminescence and absorption spectra. Applied in our kinetic model, the obtained parameters reveal that the recombination of free carriers and excitons are both subject to trapping and re-excitation via shallow traps, that when taken in to consideration allow us to qualitatively reproduce the observed excitation-dependent time-resolved photoluminescence across a wide range of temperatures. This process provides a simple, coherent explanation for unusually long lifetimes observed in lead halide perovskites. Analysis of the trap-state density versus temperature suggests that their main origin is a consequence of disorder, which is increased at temperatures close to the phase transition.

6.7 Contributions and Publications

Spectroscopy measurements were carried out by both the author and Giacomo Piana. The model for charge-carrier recombination was developed and the data was fitted by Giacomo Piana, with the assistance of the author and Pavlos Lagoudakis. The author was responsible for modelling for the absorption spectroscopy and fabricating the perovskite thin films. The content of this chapter has been published in Ref. [68], and parts of the text have been included verbatim.

Chapter 7

Influence of Grain Boundaries on Recombination Dynamics in Lead Halide Perovskites

7.1 Introduction

Lead halide perovskites (LHPs) demonstrate many optimal properties for photovoltaic (PV) technologies, with a record power conversion efficiency now greater than 25 % [12]. As a result, many studies have attempted to reveal the origin of the high performance of these materials, contributing to the understanding and further development of optoelectronic devices based on LHPs. One source of superiority of these materials is the high photoluminescence quantum efficiency [188, 261, 262], which can be drastically enhanced, for example, by simply illuminating the sample in the presence of oxygen [117, 118, 263–267] or by using other passivation techniques [112, 149, 268, 269]. This allows the efficiency of solar cells to approach the theoretical limit of the open-circuit voltage by limiting non-radiative recombination [59, 270].

Since the majority of high-efficiency perovskite solar cells and fabrication processes are associated with absorbing layers that are polycrystalline, understanding the influence of different film morphologies on the resulting devices is critical. It is well agreed that

the density and nature of trap states of LHPs vary greatly depending on the fabrication protocol and therefore their morphology likely has a substantial role to play. Investigations into the relationship between morphology and recombination properties of LHP thin films have yielded a mixture of conclusions. It is usually assumed that films which more closely resemble monocrystalline layers (larger, fused grains) are likely to result in better-performing devices due to a reduced number of non-radiative recombination centres. This assumption has been validated by several studies that show a correlation between trap states and grain boundaries [112, 271–274]. Attempts to determine the source of charge-trapping linked with grain boundaries have alluded to defects that produce deeper ($>$ 50 meV) sub-bandgap states [273], most likely associated with halide species [241, 242, 271, 275]. Furthermore, Shao and colleagues found that grain boundaries act as channels that mediate ion migration [275].

Ionic transport in LHPs is understood to have a large impact on the device performance and play a key role in the operating mechanism for solar cells based on LHPs, and also gives rise to hysteresis effects [270, 276, 277]. The mobility of ions within $MAPbI_3$ is partly responsible for the enhancement of photoluminescence following light irradiation, as deQuilettes *et al.* showed that the increase of photoluminescence intensity is caused by an order-of-magnitude reduction in trap-state density, which is correlated to iodine migrating away from the illumination spot [261]. A similar effect was also observed by Mosconi and co-workers [114]. Li *et al.* observed evidence of 'subgrain boundaries' using photoluminescence microscopy, which could not be identified using atomic force microscopy (AFM) or scanning-electron microscopy (SEM), which suggests that advanced techniques could reveal non-trivial heterogeneity of charge recombination in LHPs [278].

One approach to investigate morphological impacts on film properties is to employ nano-scale imaging techniques. Various scanning-probe microscopy techniques have been utilised to achieve nano-scale resolution for investigating properties of LHPS [279–283]. For example, Garrett *et al.* used Kelvin probe force microscopy to monitor the local open-circuit voltage in $MAPbI_3$, revealing localised time-dependent changes, likely

caused by intragrain ion migration [282]. Vrućinić and co-workers used scanning near-field optical microscopy to image the photoluminescence with ≈ 390 nm resolution, allowing them to observe localised regions of increased photoluminescence intensity [281].

Here we present results from combined atomic force microscopy (AFM) and scanning near-field optical microscopy (SNOM) measurements on $MAPbI_3$ and $MAPbI_{3-x}Cl_x$ thin films which allows us to simultaneously monitor the sample morphology and local photoluminescence properties with near-field resolution. We also present the results from spatially-averaged measurements of the time-resolved photoluminescence in a vacuum, showing how ion transport across grain boundaries is responsible for the observed long-timescale variation in the photoluminescence properties.

7.2 $MAPbI_3$ and $MAPbI_{3-x}Cl_x$ Thin Films

We prepare lead halide perovskite thin films using two different methods (see experimental). For the first method, we use a precursor of PbI_2 and methylammonium iodide (MAI). This precursor solution is commonly used for fabricating thin films of $MAPbI_3$ but requires an additional strategy to obtain smooth, uniform films. These strategies include post-deposition steps [146, 147, 150, 167], alternative solvent systems [144, 148, 284] or additives [285–287]. We use a 'gas quenching' method described previously [146] which involves using a mixed solvent system of DMF and DMSO, and the flow of inert gas on the surface of the film during the coating process. This method yields smooth mirror-like films with a grain size of ∼ 100–200 nm. For the second method, we use $PbCl_2$ as a component of the precursor solution, which enables us to obtain relatively smooth polycrystalline films of $CH_3NH_3PbI_{3-x}Cl_x$ ($MAPbI_{3-x}Cl_x$) with interconnected grains of ∼ 500 nm in diameter, using a one-step spin-coating deposition without any additional smoothening technique. The inclusion of chloride in the resulting film has previously found to be very low [136], but has an impact on the resulting structural properties of the film.

Figure 7.1a and b show the scanning-electron microscope (SEM) and atomic force microscopy (AFM) images obtained from $MAPbI_3$ and $MAPbI_{3-x}Cl_x$ samples respectively.

$MAPbI_3$ thin films show much smaller grains with a diameter $\sim$ 100-200 nm, with a high

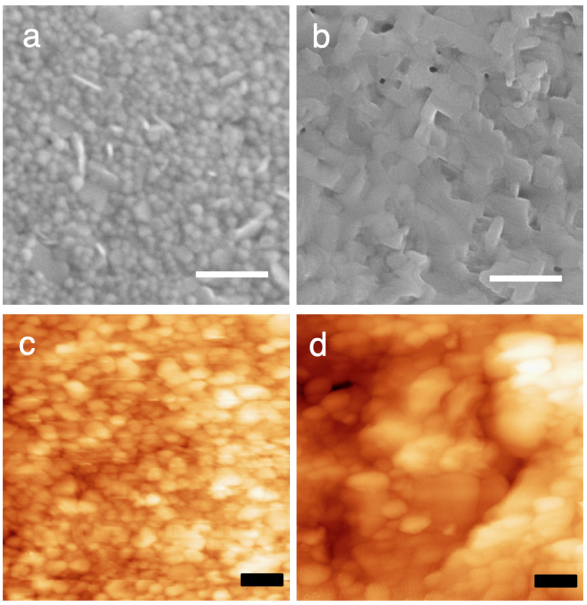

Figure 7.1: Morphology characterisation of lead halide perovskite thin films. Scanning electron microscope images of the a) $MAPbI_3$ and b) $MAPbI_{3-x}Cl_x$ thin films. Atomic force microscopy of the c) $MAPbI_3$ and d) $MAPbI_{3-x}Cl_x$ thin films.

spatial density of distinct grain boundaries. The $MAPbI_{3-x}Cl_x$ thin films however have much larger, interconnected grains ($>$ 500 nm). The difference in morphology in these films is due to the different crystallisation dynamics during the deposition and annealing stages [135, 137, 288].

7.3 Low Temperature Photoluminescence Spectra

Figure 7.2a and b show the photoluminescence spectra at low temperatures (11-120 K) for the $MAPbI_3$ and $MAPbI_{3-x}Cl_x$ thin films, respectively. At typical device operating temperatures, the photoluminescence spectra of LHPs, including $MAPbI_3$ and $MAPbI_{3-x}Cl_x$ typically have a single peak, and emission from deep sub-bandgap states is not observed [75, 107, 289]. At low temperature however, multiple peaks have been observed, with lower energy emission potentially originating from trap-assisted recombination [69].

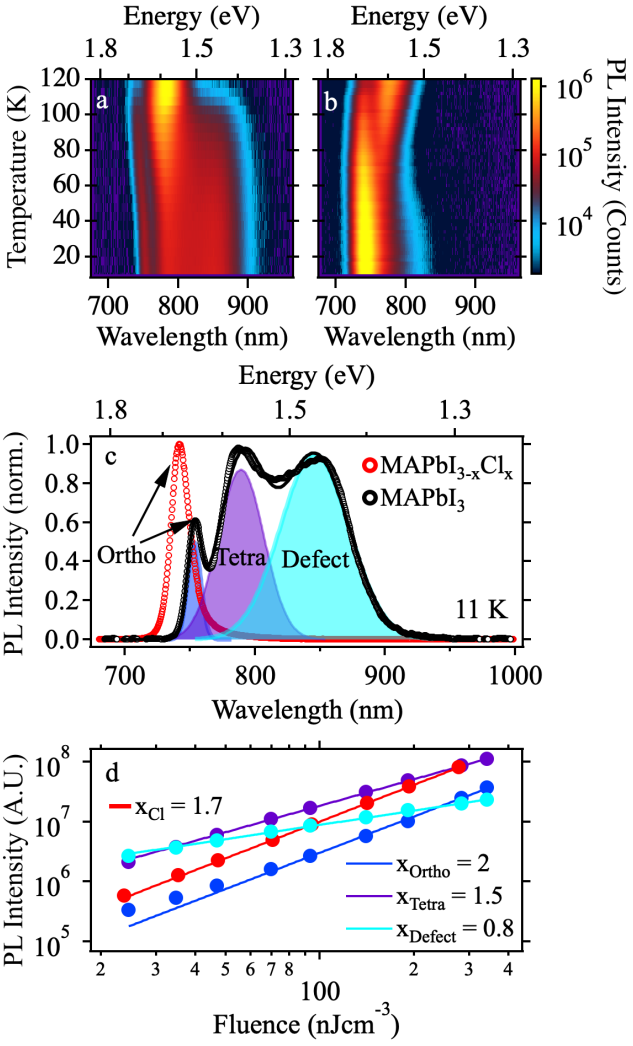

Figure 7.2: Low temperature steady-state photoluminescence spectra of a) $MAPbI_3$ and b) $MAPbI_{3-x}Cl_x$. c) Photoluminescence spectra of the perovskite thin films at 11 K. Multiple maxima observed in the $MAPbI_3$ spectrum are due to a coexistence of structural phases and defect-state emission. d) Fluence-dependence of the perovskite thin-film photoluminescence intensity at 11 K.

Observing the low temperature photoluminescence in our $MAPbI_3$ samples, there appear to be contributions from three distinct radiative recombination channels. At $\sim$ 120–140 K there is a transition from the tetragonal to the orthorhombic structural phase upon reducing temperature of $MAPbI_3$. However, inclusions of the higher temperature tetragonal phase have been observed at low temperatures, and is likely the source of the multiple photoluminescence maxima we observe for $MAPbI_3$ [67–69]. We fitted the photoluminescence at 11 K with three Gaussian functions (figure 7.2c) and we attribute the peak at $\sim$ 1.65 eV to the orthorhombic phase, the peak at $\sim$ 1.58 eV to the tetragonal phase and the peak at $\sim$ 1.46 eV to a defect state, which we believe is radiative at this

temperature [69]. Therefore, the energy of this defect state corresponds to approximately $\sim$ 210 meV below the band edge of the orthorhombic phase.

The Shibata model relates the excitation intensity, L to the observed photoluminescence intensity, I with a power law given by $I \propto L^x$, where x depends on the nature of the recombination. For free-carrier and free-exciton recombination $x = 1$–2, whereas $x \leq 1$ corresponds to trap-assisted recombination[52, 53] (see chapter 2). Figure 7.2d shows the fluence-dependence of the integrated photoluminescence intensity for the different transitions in $MAPbI_3$ and $MAPbI_{3-x}Cl_x$. The peak at $\sim$ 1.46 eV in $MAPbI_3$ has a sublinear dependence on the excitation intensity ($x = 0.8$), indicative of monomolecular (trap-state) recombination. These results are in contrast with the photoluminescence spectrum of $MAPbI_{3-x}Cl_x$ which exhibits a single peak at low temperature, at a slightly higher energy than the orthorhombic peak for $MAPbI_3$ (Figure 7.2c). This suggests that Cl has a minor impact on the band structure, in agreement with prior reports [136], however, this is unlikely to have an impact on the defect formation or charge diffusion in these materials. Instead, we propose that the trap-state emission from $MAPbI_3$ is associated with the high spatial density of grain boundaries in our samples.

7.4 Ionic Defect Transport in Time-Resolved Photoluminescence

Figure 7.3a and b show the time-resolved photoluminescence decays for $MAPbI_3$ and $MAPbI_{3-x}Cl_x$ thin films over time under pulsed-laser illumination (188 $nJcm^{-2}$). Both films show a very fast decay initially ($\sim$ 10 ns) which rapidly becomes slower over the first few 100 s. The increase in photoluminescence lifetime correlates with an increase in the photoluminescence intensity in both samples, as shown in Figure 7.3c. This rise in intensity reflects an increase in the photoluminescence quantum efficiency (PLQE), which is maximised at $\sim$200 s in the $MAPbI_3$ sample, after which it begins to decrease slowly. Conversely, in $MAPbI_{3-x}Cl_x$ the intensity continues to increase, but at a slower rate than the initial fast rise. The initial rise time is similar in both samples, suggesting

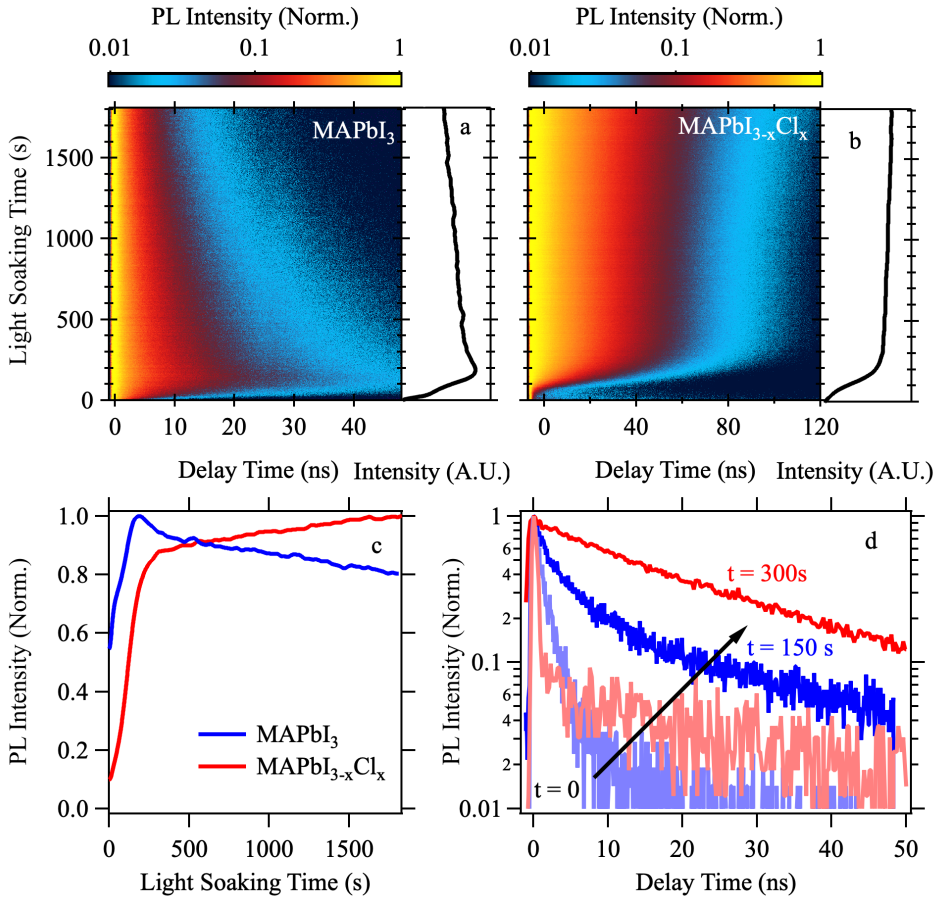

Figure 7.3: Time-resolved photoluminescence decays for different light-soaking time periods for a) $MAPbI_3$ (blue) and b) $MAPbI_{3-x}Cl_x$ (red). c) The photoluminescence intensity of the perovskite thin films as a function of light soaking time. d) Initial time-resolved photoluminescence decays (lighter curves) and decays after the photoluminescence has reached maximum intensity (darker curves).

that the mechanism responsible for the initial photoluminescence enhancement is the same in both samples.

7.5 Mechanism for Photoluminescence Enhancement

Figure 7.4 shows the proposed mechanism to describe the slow photoluminescence transients observed. Initially an equal number of electrons and holes are photoexcited. Iodide vacancies produce trap states for electrons, whereas the corresponding intersitials act as hole traps. The large amount of charge-carrier trapping is the cause of low PLQE

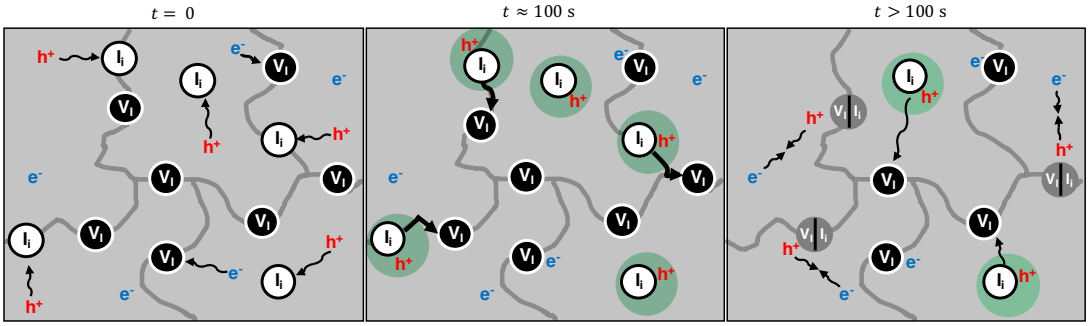

Figure 7.4: Schematic showing the processes during light soaking in a vacuum. At $t = 0$ s, an equal number of electrons and holes are photoexcited. Iodide vacancies act as electron traps and interstitials act as hole traps. At $t \approx 100$ s, interstitials initially present on grain boundaries can move along the grain boundaries and annihilate with vacancies. As defects begin to become annihilated at $t > 100$ s, the holes that were trapped by interstitials become free carriers and interstitials that originated within grains slowly diffuse to the grain boundaries.

during the first few of seconds during photoexcitaion (Figure 7.3c). This fast charge trapping is the dominant mechanism and hence produces short-lived photoluminescence decays (Figure 7.3d). Interstitials now bound to holes (neutral overall charge) are no longer pinned by the surrounding Coulombic potential and become free to diffuse, at some point filling the associated vacancies. Following this, photogenerated holes are no longer trapped upon excitation by the mobile defect states and instead are free carriers, contributing to bimolecular recombination, increasing the PLQE over $\sim$ 100 s. The reduction in charge trapping compared to radiative recombination causes the overall recombination lifetime to increase (Figure 7.3d).

Shao and colleagues previously used conductive AFM to show that grain boundaries facilitate ion transport [275]. Therefore we propose that the initial rise in photoluminescence is produced by annihilation of defects by mobile iodide initially present on the grain boundaries in both samples. However, in the $MAPbI_{3-x}Cl_x$ samples, the grains are much larger and the average distance between an iodide interstitial and the nearest grain boundary is therefore larger. Iodide ions that are initially present within grains on film formation diffuse slowly, impeded by surrounding potential of the crystal. As the ions slowly diffuse, they eventually reach a grain boundary where they can travel to a vacancy and passivate it. This process occurs over a very long time scale (> 1000 s), increasing the PLQE and carrier lifetime. This process does not occur in the $MAPbI_3$

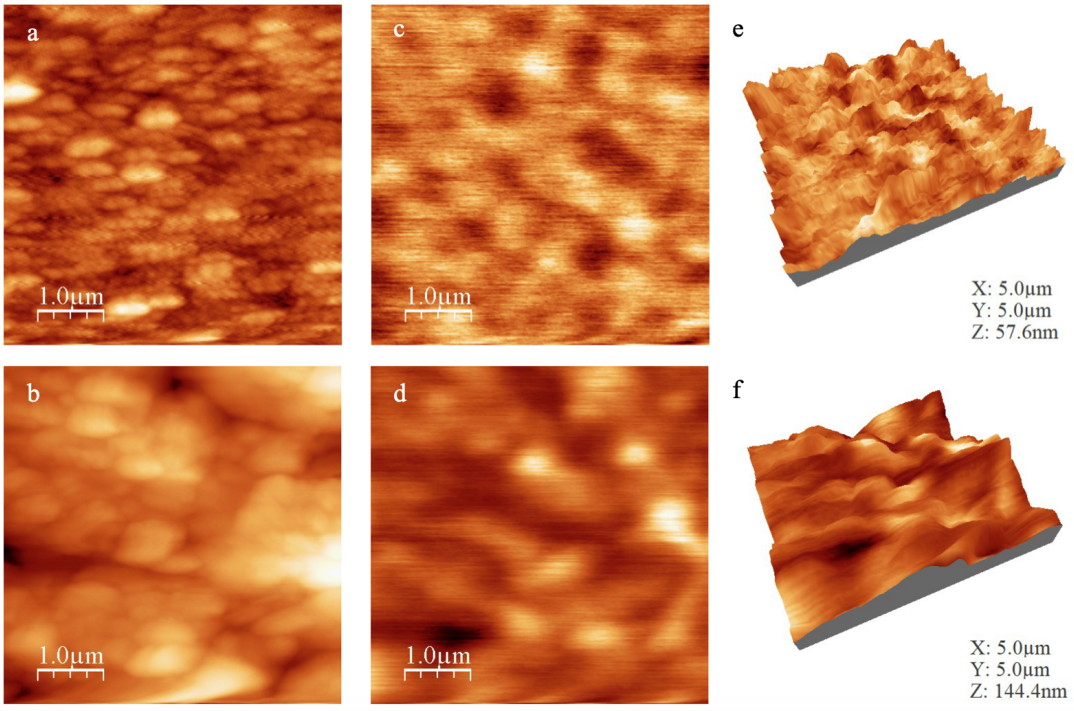

Figure 7.5: Combined AFM and SNOM images of perovskite thin films. AFM images of a) $MAPbI_3$ and b) $MAPbI_{3-x}Cl_x$ thin films. The corresponding SNOM PL maps of c) $MAPbI_3$ and d) $MAPbI_{3-x}Cl_x$. e) and f) 3D topology with the PL intensity shown by the colour scale for $MAPbI_3$ and $MAPbI_{3-x}Cl_x$, respectively.

films however, since the photoexcited carriers and intersitials diffuse easily to the grain boundaries because they will be in closer proximity on average to the nearest boundary due to the reduced grain size. In $MAPbI_3$ the PLQE and lifetime slowly decrease after reaching the maximum values, reaching around 80 % of the maxima after around 1600 s, which is the feature most commonly observed in vacuum or inert atmosphere [261, 265].

7.6 Scanning Near-Field Optical Microscopy

We performed simultaneous SNOM and AFM measurements on the thin films of $MAPbI_3$ and $MAPbI_{3-x}Cl_x$. The resulting images are shown in Figure 7.5. The SNOM PL maps (Figure 7.5c and d) show regions of higher and lower intensity PL that relate to the size of the grains (smaller regions for $MAPbI_3$, larger regions for $MAPbI_{3-x}Cl_x$). However, the regions appear to span several grains for both the samples and the location of the regions does not correlate with the morphology in any clear way. For example, in the

SNOM image for $MAPbI_{3-x}Cl_x$ (Figure 7.5d), there is a region of very low intensity PL in the bottom-left corner that does not appear to correlate to any particular feature in the AFM image (Figure 7.5d).

The smaller localised regions of PL in the $MAPbI_3$ thin film suggest that photogenerated charges do not diffuse easily between grains in these samples. Darker regions may originate from grains that are richer in defects associated with iodide and hence have a higher trap-state density. Interestingly, there are several regions in the PL maps for both samples where emission appears to originate from grain boundaries. Although this seems counter-intuitive, it may be an effect of the highly localised nature of the excitation in the SNOM experiment, but further investigation is required to understand this phenomenon.

7.7 Conclusion

In conclusion, we have investigated the role of grain boundaries on the photoluminescence properties of lead halide perovskite thin films. Low-temperature photoluminescence emission at lower photon energies suggests the presence of defects situated at $\sim$ 200 meV below the band edge in $MAPbI_3$ samples, which are likely associated with grain boundaries. We have shown how long time-scale changes of the time-resolved photoluminescence decays can be explained by the interaction of free carriers and iodide defects. Preliminary studies of nano-scale photoluminescence appear to show a correlation between the size of grains and localised photoluminescence regions. Further studies using this technique should elucidate the findings we have obtained thus far.

7.8 Contributions and Notice

The spectroscopy measurements were performed by both the author and Giacomo Piana. The SEM and AFM images in Figure 7.1 were acquired by the author. The combined SNOM and AFM images were taken by Katarzyna Rechcińska from the university of

Warsaw, with the assistance of the author and Giacomo Piana. The author fabricated the samples.

The experiments in this section are currently ongoing and should be therefore considered as work-in-progress. The discussion and conclusions of the results may be subject to change following the acquisition of new data.

Chapter 8

Perovskite Solar Cells Hybridised with CdTe Quantum Dots

8.1 Introduction

The past few decades have seen a rapid rise in the development of nanomaterials, such as colloidal nanocrystals [290, 291]. These materials exhibit highly desirable properties for optoelectronic devices (such as strong, spectrally tunable absorption and emission of light, for example), and can be processed from solution using wet chemistry techniques. Similarly, research of perovskite materials has lead to outstanding developments in solution-processable optoelectronics. For example, perovskite solar cells now lead the field of solution-processed photovoltaics in terms of power conversion efficiency (PCE) [12]. Nanomaterials can be used directly as the active layers in light-emitting diodes (LEDs)[292–295] and solar cells [296–299], but also their properties been utilised in well established technologies such as III-V semiconductor solar cells [42–44] and GaN LEDs [45, 46]. In the latter examples, energy may be transferred non-radiatively through resonance energy transfer (RET), or, charges can be directly transferred between nanostructures and the active layers [300, 301].

In the field of perovskite photovoltaics, most of the research is focused on improving device efficiencies and the study of the physical properties of the materials. Comparatively-little effort has been made to explore the potential use of nanomaterials for improving bulk-perovskite solar cells. Successful attempts have been made to combine colloidal quantum dots (QDs) with bulk perovskites for LED [170], solar cell [302–304] and photodetector [173] applications. Ning *et al.* for example developed quantum-dot-in-perovskite solids, showing that bulk $CH_3NH_3PbI_3$ can be grown heteroepitaxially on PbS QDs, allowing the formation of layers that can utilise both the superior charge transport properties of the $CH_3NH_3PbI_3$ and the light emitting properties of the QDs [170].

In this section, we investigate the feasibility and effects of integrating colloidal QDs with inverted planar perovskite solar cells with an active layer of $CH_3NH_3PbI_{3-x}Cl_x$ ($MAPbI_{3-x}Cl_x$). By combining QDs with PEDOT:PSS as a hybrid hole-transporting layer (HTL), we are able to demonstrate enhancements in the photocurrent produced by the devices. We characterise the hybrid HTL films using confocal laser scanning microscopy (CLSM) for PL imaging and characterise the hybrid devices using current–voltage (J–V) and external quantum efficiency (EQE) measurements.

8.2 Quantum Dot–PEDOT:PSS Blend

We produced a blend of QDs in films of PEDOT:PSS which is formed on deposition of the HTL. We used core-type water-dispersible CdTe QDs with an emission wavelength (λ_{em}) of 670 nm terminated with carboxyl groups (–COOH), which become embedded directly in to the PEDOT:PSS films. To achieve this we firstly added the QDs in dry powder form to the aqueous PEDOT:PSS solution so that the QDs were dispersed throughout the solution. We deposited films from solutions containing 1, 5 and 10 mg/ml of QDs using a dynamic spin coating method, described in section 4.

In order to investigate how the QDs are dispersed throughout the film, we used CLSM to image the PL from the QDs, showing the emission intensity on a micro-scale. The corresponding maps of PL intensity are shown in Figure 8.1. On observation of the

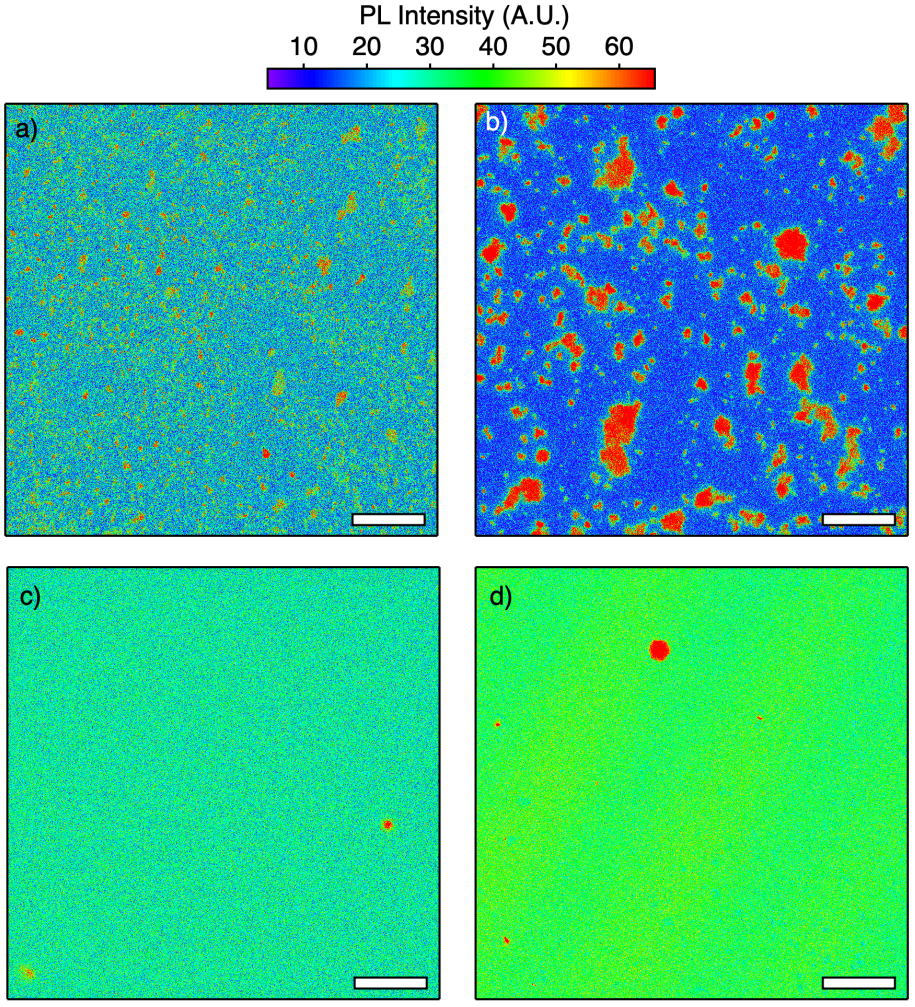

Figure 8.1: Micro PL-imaging of QD–PEDOT:PSS blend. CLSM image of QD–PEDOT:PSS blend with 10 mg/ml concentration (a) and b)), 5 mg/ml (c)) and 1 mg/ml (d)). The scale bar is 100 µm for a), c), and d). The Scale bar is 25 µm for b).

PL from the QDs, it appears that lower concentrations (5 and 1 mg/ml) of QDs in the solution yields a uniform distribution of QDs throughout the PEDOT:PSS films (Figure 8.1 c and d, respectively). Conversely, we found that that agglomerates form when higher concentrations are used, such as 10 mg/ml (Figure 8.1a and b). The concentration that leads to the best combination of uniformity and average PL intensity appears to be 1 mg/ml. This is evidenced by the PL map (Figure 8.1d), showing an increase in PL intensity of $\sim 30\%$ over the films with 5 mg/ml. This may be due to the formation of non-emissive aggregates of QDs on deposition, causing a reduction in overall emission intensity. The agglomerates that are emissive in the films using 10mg/ml may

be mixed with the same non-emissive aggregates present in the films using 5 mg/ml. Horizontal stripes are observed running from the lower-left to the upper-right of the image in Figure 8.1d, which is likely due to fluctuations in the spatial density of QDs due to spin coating. On a larger scale these stripes are likely to form concentric circles.

We fabricated inverted planar solar cells with an active layer of $MAPbI_{3-x}Cl_x$ with varying concentrations of QDs in the hybrid HTL, as described in section 4. The schematic of the device is shown in Figure 8.2. We characterised the devices using current–voltage

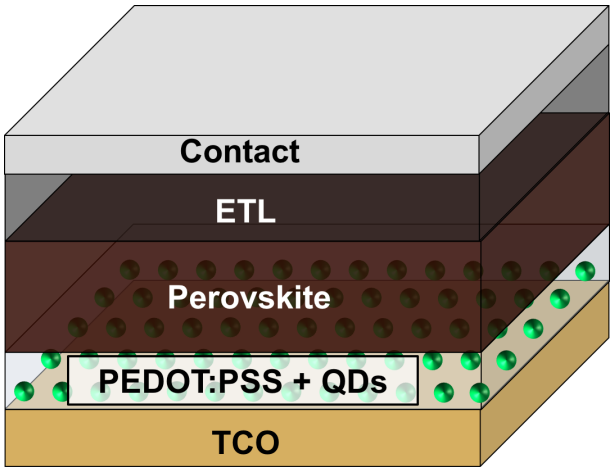

Figure 8.2: Device schematic of the perovskite solar cell with a QD–PEDOT:PSS HTL. Schematic of the inverted planar architecture used for the devices. The CdTe QDs are dispersed throughout the PEDOT:PSS HTL.

scans (J–V) under simulated sunlight and the resulting parameters obtained are shown in Figure 8.3. The devices with 0.1 mg/ml and 1 mg/ml of QDs in the QD–PEDOT:PSS blend demonstrated higher short-circuit current density (J_{sc}), with $\sim$ 1 $mAcm^{-2}$ difference in the average J_{sc} between the reference device and the device with 1 mg/ml QDs (Figure 8.3b). For the best-performing devices for each configuration, the hybrid devices with 0.1 and 1mg/ml QDs show almost 1 % increase in PCE (Figure 8.3a). This increase however is mainly due to an increase in the fill factor (Figure 8.3d). The increase in J_{sc} in the hybrid devices, suggests an increase in light absorption in the perovskite film.

To investigate the spectral responsivity of the devices, we performed external quantum efficiency (EQE) measurements. The best-performing devices were measured and their corresponding J–V and EQE responses are shown in Figure 8.4.

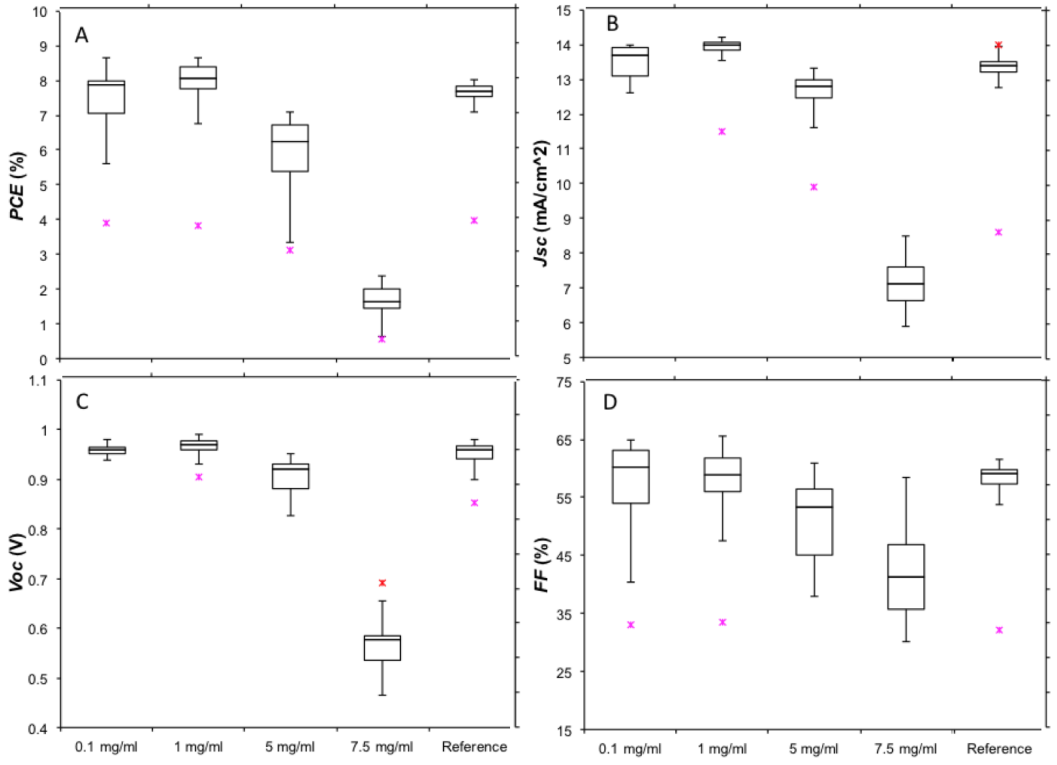

Figure 8.3: Device parameters of perovskite solar cells with a QD–PEDOT:PSS HTL Devices with a HTL with 1 mg/ml of QDs show an increase of average and maximum efficiency.

The J–V response of the best devices with 0.1 and 1 mg/ml of QDs show a very small increase in J_{sc} compared with the reference (Figure 8.4a), whereas the EQE shows a substantial improvement. We used (2.24) to calculate the J_{sc} from the EQE spectra of the devices and obtained a J_{sc} value of 14.25 mAcm^{-2} for the device with 0.1 mg/ml of QDs and 14.91 mAcm^{-2} for the reference device. The value of J_{sc} for best-performing reference device obtained by J–V measurements was 13.9 mAcm^{-2} and hence in contradiction to the value calculated from the EQE. The discrepancy in J_{sc} is likely to be due to the nature of the J–V scans and the well known hysteresis effects in lead halide perovskite solar cells [277, 305–307]. The EQE of the hybrid device containing 0.1 mg/ml of QDs is lower than the reference cell at all wavelengths except around $\sim$ 580 to 630 nm. We calculated the difference in EQE between the hybrid devices and the reference device, shown in Figure 8.4b. The curves obtained appear to correlate with absorbance spectrum of the QDs, which is plotted on the same graph (red curve). This suggests that the QDs are responsible for a change in spectral response, shown in the EQE difference spectrum for the hybrid devices. This could be due to luminescence

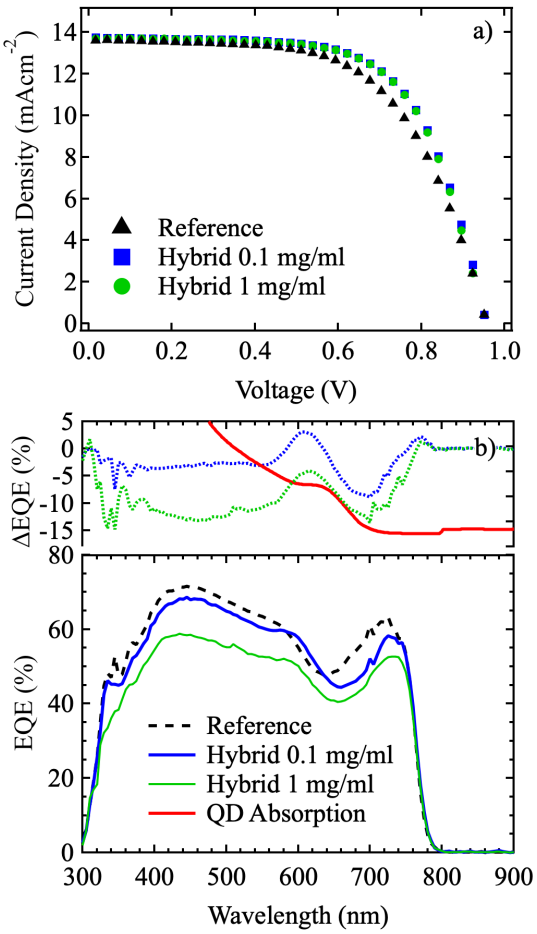

Figure 8.4: Electrical characterisation of perovskite solar cells. a) *J*–*V* curves of the hybrid and reference devices. b) EQE spectra for the hybrid and references devices, showing the EQE difference spectra in the top panel.

downshifting, scattering effects or resonance energy transfer for example, but further investigation is required to determine the cause of this effect.

8.3 Conclusion

Distribution of colloidal inorganic semiconductor QDs in PEDOT:PSS HTL films has been successfully achieved with CdTe core-type QDs. Photovoltaic devices using a PEDOT:PSS/QD HTL were fabricated, with an increase in PCE of > 1 % observed compared with reference devices without any QDs. The cause of this enhancement is not fully clear but is likely due luminescence downshifting, resonance energy transfer or scattering effects. Thin films of $MAPbI_{3-x}Cl_x$ hybridised with CdTe QDs were found to have enhanced PL, revealed by confocal laser-scanning microscopy. A large mass of organic functional groups present in the film are likely causes of reduced device performance for higher concentrations of QDs. Nanocrystals with smaller surface molecules should be prioritised as these are likely to have a less detrimental impact on the electrical properties.

8.4 Contributions

Fabrication and characterisation of thin films and devices was carried out by the Author, with useful inputs from Phillip Hank, Kevin Danneker, Abinash Poudel and Nick Klokkou.

Chapter 9

Conclusions

Research on lead halide perovskites for optoelectronics has produced remarkable outcomes, with tandem perovskite–silicon solar cells now outperforming devices based on silicon alone, for example. Despite over a decade of intense activity in this field, a complete picture of the fundamental properties of these materials has evaded the scientific community. In the process, alluring features of the unusual materials have been discovered, with some potential applications still in their infancy. The work in this thesis has contributed by providing an input to the discussion, which combined with other efforts represents a step on the journey to the understanding of lead halide perovskites.

In chapter 5, the optical properties of $MAPbI_3$ were studied. Critical-point analysis of variable-angle spectroscopic ellipsometry data was used to show transitions across a wide spectral range, which is in agreement with results from spectrophotometry. A model is developed, based on Tauc-Lorentz oscillators, using parameters that can be physically justified. The modelling process outlined in the chapter serves as a guide that may be utilised and adapted for different perovskite materials. The optical transitions at 4.63 and 5.88 eV are often overlooked due to experimental limitations and provide vital information relating to the fundamental properties of $MAPbI_3$ and the potential applications of the material.

In chapter 6, it was shown how different spectroscopies can be used to extract physical

information about semiconductor materials and used to develop a model for the recombination dynamics. Applying the model for lead halide perovskites, the experimental data is best described as the recombination of free carriers and excitons, which are both subject to trapping and re-excitation via shallow traps. This process provides a simple, coherent explanation for unusually long lifetimes observed in lead halide perovskites. It is clear that disorder plays a role in the density of shallow trap states, since an increase is observed at temperatures close to the structural phase transition.

Chapter 7 extended the study of photoluminescence in lead halide perovskites, focusing on the effect of grain boundaries on recombination. A correlation between grain boundaries and defects was extracted by using imaging techniques and photoluminescence studies. Drastic changes of the transient photoluminescence in these materials have been attributed to the interaction of free carriers and iodide defects, with the spatial-density of grain boundaries modulating this effect. Nano-scale photoluminescence imaging was used, with interpretation of initial results suggesting a link between the grain geometry and localised regions of photoluminescence.

Nanomaterials such as colloidal quantum dots have been developed over the past few decades and have become a commercialised technology for displays, for example. However, the combination of bulk-semiconductor and nano-scale semiconductor materials for photovoltaics has only been minimally explored but with promising results. This fact is particularly true for perovskite solar cells since the field is far from maturity, with device performances improving rapidly each year. In chapter 8, a particular route of integrating QDs with inverted planar perovskite solar cells was has shown. The insights gained from the subjects of the previous chapters have assisted in understanding the key optoelectronic properties, facilitating the integration of nanomaterials to perovskite solar cells. The work in this chapter is a promising advancement towards perovskite solar cells employing additional light harvesting processes.

9.1 Future Work

In chapter 5, evidence was found for optical transitions at ultraviolet photon energies in $MAPbI_3$. These higher-energy transitions are not often discussed in theoretical works, which usually aim to reproduce the band structure of $MAPbI_3$ in relation to the bandgap. Although the bandgap is a crucial feature of a semiconductor, a complete description of the band structure should account for all optical transitions, including transitions between deeper energy bands. Hence, future work should be carried out to reproduce not only the bandgap, but also the spectral features at higher photon energies, such as those observed in this thesis and the studies of other authors.

Chapter 6 presented the results of spectroscopy studies of lead halide perovskite thin films, with one conclusion being the coexistence of structural phases in $MAPbI_{3-x}Cl_x$. At lower temperatures, previous work has evidenced charge transfer from the orthorhombic to the tetragonal phase [69]. Interestingly we do not observe the same features in our results, suggesting a different behaviour due to differences in the sample. From the scanning electron microscopy images of the samples, our material has a different morphology, compared to the authors referenced, similar to the subject described in chapter 7. A further study could be to investigate the inter-phase charge transfer at low temperatures, comparing our samples of $MAPbI_3$ and $MAPbI_{3-x}Cl_x$. Ideally, simultaneous spectrally and time-resolved photoluminescence data would be required (using a streak camera for example), as in Ref. [69]. Moreover, this data would reveal the contributions of excitons and free-carriers to the the time-resolved photoluminescence, which is another main topic of this chapter.

In chapter 7, the photoluminescence properties of lead halide perovskite thin films were investigated using scanning near-field optical microscopy. At present, only preliminary results have been acquired from this technique and the author and colleagues are in the process of carrying out experiments. Future studies will be performed to investigate the effect of illuminating the films over longer time periods on the nano-scale photoluminescence properties. Furthermore, the technique will be extended to record the photoluminescence spectrum and transient decays to assist in the understanding of the

photophysical processes in lead halide perovskites. The author is currently working with colleagues to synthesise single crystals of lead halide perovskites, in order to provide a reference of samples with the absence of grain boundaries. Observation of the nano-scale photoluminescence properties in single crystals, compared to the polycrystalline thin films should unambiguously reveal the effects of grain boundaries.

Lastly, in chapter 8, perovskite solar cells hybridised with QDs were fabricated and characterised. This only represents initial studies on this hybrid device design. Further work should be carried out to determine the effect of the QDs and investigate potential processes such as luminescent downshifting, resonance energy transfer, and light scattering. Additional experiments are required to determine the optimal concentrations of QDs in the hole-transporting layer, and the resulting configuration should be used in highly optimised reference devices. By doing so, the full potential of the hybrid device structure can be ascertained. The use of different QDs and device architectures may also be explored and compared.

References

[1] NASA/GISS, "Global Climate Change - Vital Signs of the Planet."

[2] A. E. Raftery, A. Zimmer, D. M. W. Frierson, R. Startz, and P. Liu, "Less than 2 °C warming by 2100 unlikely," *Nature Climate Change*, 2017.

[3] G. P. Smestad, *Optoelectronics of Solar Cells*. SPIE Press monograph, Society of Photo Optical, 2002.

[4] Energytrend.com, "PV Energy Trends - Energytrend.com."

[5] M. A. Green, K. Emery, Y. Hishikawa, W. Warta, E. D. Dunlop, D. H. Levi, and A. W. Y. Ho-Baillie, "Solar cell efficiency tables (version 49)," *Progress in Photovoltaics: Research and Applications*, vol. 25, pp. 3–13, 2016.

[6] Z. K. Tan, R. S. Moghaddam, M. L. Lai, P. Docampo, R. Higler, F. Deschler, M. Price, A. Sadhanala, L. M. Pazos, D. Credgington, F. Hanusch, T. Bein, H. J. Snaith, and R. H. Friend, "Bright light-emitting diodes based on organometal halide perovskite," *Nature Nanotechnology*, vol. 9, no. August, pp. 1–6, 2014.

[7] L. Dou, Y. M. Yang, J. You, Z. Hong, W.-H. Chang, G. Li, and Y. Yang, "Solution-processed hybrid perovskite photodetectors with high detectivity," *Nature communications*, vol. 5, p. 5404, 1 2014.

[8] B. R. Sutherland and E. H. Sargent, "Perovskite photonic sources," *Nature Photonics*, vol. 10, no. 5, pp. 295–302, 2016.

[9] G. Xing, N. Mathews, S. S. Lim, N. Yantara, X. Liu, D. Sabba, M. Grätzel, S. Mhaisalkar, and T. C. Sum, "Low-temperature solution-processed wavelength-tunable perovskites for lasing.," *Nat. Mater.*, vol. 13, no. 5, pp. 476–80, 2014.

[10] D. Weber, "CH3NH3PbX3, a Pb(II)-System with Cubic Perovskite Structure," *Zeitschrift für Naturforschung B*, vol. 33b, no. August 1978, pp. 1443–1445, 1978.

[11] A. Kojima, K. Teshima, Y. Shirai, and T. Miyasaka, "Organometal Halide Perovskites as Visible-Light Sensitizers for Photovoltaic Cells," *Journal of the American Chemical Society*, vol. 131, pp. 6050–6051, 5 2009.

[12] NREL, "NREL Efficiency Chart (Acessed: 11/05/2019)," 2019.

[13] P. Docampo, J. M. Ball, M. Darwich, G. E. Eperon, and H. J. Snaith, "Efficient organometal trihalide perovskite planar-heterojunction solar cells on flexible polymer substrates.," *Nature communications*, vol. 4, p. 2761, 1 2013.

[14] Y. Li, L. Meng, Y. M. Yang, G. Xu, Z. Hong, Q. Chen, J. You, G. Li, Y. Yang, and Y. Li, "High-efficiency robust perovskite solar cells on ultrathin flexible substrates," *Nature Communications*, vol. 7, p. 10214, 2016.

[15] M. B. Johnston and L. M. Herz, "Hybrid Perovskites for Photovoltaics: Charge-Carrier Recombination, Diffusion, and Radiative Efficiencies," *Accounts of Chemical Research*, vol. 49, no. 1, pp. 146–154, 2016.

[16] C. S. Ponseca, T. J. Savenije, M. Abdellah, K. Zheng, A. Yartsev, T. Pascher, T. Harlang, P. Chabera, T. Pullerits, A. Stepanov, J.-p. Wolf, and V. Sundstro, "Organometal Halide Perovskite Solar Cell Materials Rationalized: Ultrafast Charge Generation, High and Microsecond-Long Balanced Mobilities, and Slow Recombination," *Journal of the American Chemical Society*, vol. 136, p. 51895192, 2014.

[17] S. D. Stranks, G. E. Eperon, G. Grancini, C. Menelaou, M. J. P. Alcocer, T. Leijtens, L. M. Herz, A. Petrozza, and H. J. Snaith, "Electron-Hole Diffusion Lengths Exceeding 1 Micrometer in an Organometal Trihalide Perovskite Absorber," *Science (New York, N.Y.)*, vol. 342, no. 2013, pp. 341–344, 2014.

[18] G. E. Eperon, S. D. Stranks, C. Menelaou, M. B. Johnston, L. M. Herz, and H. J. Snaith, "Formamidinium lead trihalide: a broadly tunable perovskite for efficient planar heterojunction solar cells," *Energy & Environmental Science*, vol. 7, no. 3, p. 982, 2014.

[19] G. E. Eperon, G. M. Paterno, R. J. Sutton, A. Zampetti, A. A. Haghighirad, F. Cacialli, and H. J. Snaith, "Inorganic caesium lead iodide perovskite solar cells," *J. Mater. Chem. A*, vol. 3, no. 39, pp. 19688–19695, 2015.

[20] D. P. McMeekin, G. Sadoughi, W. Rehman, G. E. Eperon, M. Saliba, M. T. Hörantner, A. Haghighirad, N. Sakai, L. Korte, B. Rech, M. B. Johnston, L. M. Herz, and H. J. Snaith, "A mixed-cation lead mixed-halide perovskite absorber for tandem solar cells," *Science*, vol. 351, pp. 151–155, 1 2016.

[21] M. Saliba, T. Matsui, J. Y. Seo, K. Domanski, J. P. Correa-Baena, M. K. Nazeeruddin, S. M. Zakeeruddin, W. Tress, A. Abate, A. Hagfeldt, and M. Grätzel, "Cesium-containing triple cation perovskite solar cells: Improved stability, reproducibility and high efficiency," *Energy and Environmental Science*, vol. 9, no. 6, pp. 1989–1997, 2016.

[22] H. S. Jung and N. G. Park, "Perovskite Solar Cells: From Materials to Devices," *Small*, vol. 11, no. 1, pp. 10–25, 2014.

[23] J. T. Jacobsson, J. P. Correa Baena, M. Pazoki, M. Saliba, K. Schenk, M. Grätzel, and A. Hagfeldt, "An exploration of the compositional space for mixed lead halogen perovskites for high efficiency devices - SI," *Energy Environ. Sci.*, vol. 41, no. 0, pp. 1–35, 2016.

[24] F. Jiang, T. Liu, B. Luo, J. Tong, F. Qin, S. Xiong, Z. Li, and Y. Zhou, "Two-terminal perovskite/perovskite tandem solar cell," *J. Mater. Chem. A*, vol. 00, pp. 1–6, 2015.

[25] G. E. Eperon, T. Leijtens, K. A. Bush, R. Prasanna, T. Green, J. T.-W. Wang, D. P. McMeekin, G. Volonakis, R. L. Milot, R. May, A. Palmstrom, D. J. Slotcavage, R. A. Belisle, J. B. Patel, E. S. Parrott, R. J. Sutton, W. Ma, F. Moghadam, B. Conings, A. Babayigit, H.-G. Boyen, S. Bent, F. Giustino, L. M. Herz, M. B. Johnston, M. D. McGehee, and H. J. Snaith, "Perovskite-perovskite tandem photovoltaics with optimized band gaps," *Science*, vol. 354, no. 6314, pp. 861–865, 2016.

[26] J. H. Heo and S. H. Im, "CH3NH3PbBr3-CH3NH3PbI3 Perovskite-Perovskite Tandem Solar Cells with Exceeding 2.2 V Open Circuit Voltage," *Advanced Materials*, pp. 5121–5125, 2016.

[27] J. Werner, C. H. Weng, A. Walter, L. Fesquet, J. P. Seif, S. De Wolf, B. Niesen, and C. Ballif, "Efficient Monolithic Perovskite/Silicon Tandem Solar Cell with Cell Area ¿1 cm2," *Journal of Physical Chemistry Letters*, vol. 7, no. 1, pp. 161–166, 2016.

[28] J. P. Mailoa, C. D. Bailie, E. C. Johlin, E. T. Hoke, A. J. Akey, W. H. Nguyen, M. D. McGehee, and T. Buonassisi, "A 2-terminal perovskite/silicon multijunction solar cell enabled by a silicon tunnel junction," *Applied Physics Letters*, vol. 106, no. 12, 2015.

[29] S. Albrecht, M. Saliba, J. P. Correa Baena, F. Lang, L. Kegelmann, M. Mews, L. Steier, A. Abate, J. Rappich, L. Korte, R. Schlatmann, M. K. Nazeeruddin, A. Hagfeldt, M. Grätzel, and B. Rech, "Monolithic perovskite/silicon-heterojunction tandem solar cells processed at low temperature," *Energy Environ. Sci.*, vol. 9, no. 1, pp. 81–88, 2016.

[30] K. A. Bush, A. F. Palmstrom, Z. J. Yu, M. Boccard, R. Cheacharoen, J. P. Mailoa, D. P. McMeekin, R. L. Hoye, C. D. Bailie, T. Leijtens, I. M. Peters, M. C. Minichetti, N. Rolston, R. Prasanna, S. Sofia, D. Harwood, W. Ma, F. Moghadam, H. J. Snaith, T. Buonassisi, Z. C. Holman, S. F. Bent, and M. D. McGehee, "23.6%-efficient monolithic perovskite/silicon tandem solar cells with improved stability," *Nature Energy*, vol. 2, no. 4, p. 17009, 2017.

[31] T. Todorov, T. Gershon, O. Gunawan, Y. S. Lee, C. Sturdevant, L.-Y. Chang, and S. Guha, "Monolithic Perovskite-CIGS Tandem Solar Cells via In Situ Band Gap Engineering," *Advanced Energy Materials*, vol. 5, no. 23, pp. n/a–n/a, 2015.

[32] A. Guchhait, H. A. Dewi, S. W. Leow, H. Wang, G. Han, F. B. Suhaimi, S. Mhaisalkar, L. H. Wong, and N. Mathews, "Over 20% Efficient CIGSPerovskite Tandem Solar Cells," *ACS Energy Letters*, vol. 2, no. 4, pp. 807–812, 2017.

[33] A. R. Uhl, Z. Yang, A. K.-Y. Jen, and H. W. Hillhouse, "Solution-processed chalcopyriteperovskite tandem solar cells in bandgap-matched two- and four-terminal architectures," *J. Mater. Chem. A*, vol. 5, no. 7, pp. 3214–3220, 2017.

[34] C. Roldán-Carmona, O. Malinkiewicz, R. Betancur, G. Longo, C. Momblona, F. Jaramillo, L. Camacho, and H. J. Bolink, "High efficiency single-junction semitransparent perovskite solar cells," *Energy & Environmental Science*, vol. 7, no. 9, p. 2968, 2014.

[35] C. O. Ramírez Quiroz, I. Levchuk, C. Bronnbauer, M. Salvador, K. Forberich, T. Heumüller, Y. Hou, P. Schweizer, E. Spiecker, and C. J. Brabec, "Pushing efficiency limits for semitransparent perovskite solar cells," *J. Mater. Chem. A*, vol. 3, no. 47, pp. 24071–24081, 2015.

[36] E. Della Gaspera, Y. Peng, Q. Hou, L. Spiccia, U. Bach, J. J. Jasieniak, and Y. B. Cheng, "Ultra-thin high efficiency semitransparent perovskite solar cells," *Nano Energy*, vol. 13, pp. 249–257, 2015.

[37] F. Guo, H. Azimi, Y. Hou, T. Przybilla, M. Hu, C. Bronnbauer, S. Langner, E. Spiecker, K. Forberich, and C. J. Brabec, "High-performance semitransparent perovskite solar cells with solution-processed silver nanowires as top electrodes," *Nanoscale*, vol. 7, pp. 1642–1649, 2014.

[38] F. Fu, T. Feurer, T. Jäger, E. Avancini, B. Bissig, S. Yoon, S. Buecheler, and A. N. Tiwari, "Low-temperature-processed efficient semi-transparent planar perovskite solar cells for bifacial and tandem applications," *Nature Communications*, vol. 6, no. November, p. 8932, 2015.

[39] G. E. Eperon, V. M. Burlakov, A. Goriely, and H. J. Snaith, "Neutral color semitransparent microstructured perovskite solar cells," *ACS Nano*, vol. 8, pp. 591–598, 1 2014.

[40] F. Fu, T. Feurer, T. P. Weiss, S. Pisoni, E. Avancini, C. Andres, S. Buecheler, and A. N. Tiwari, "High-efficiency inverted semi-transparent planar perovskite solar cells in substrate configuration," *Nature Energy*, vol. 2, no. 1, pp. 1234–1237, 2017.

[41] V. M. Agranovich, Y. N. Gartstein, and M. Litinskaya, "Hybrid resonant organic-inorganic nanostructures for optoelectronic applications," *Chemical Reviews*, vol. 111, no. 9, pp. 5179–5214, 2011.

[42] S. Chanyawadee, R. T. Harley, M. Henini, D. V. Talapin, and P. G. Lagoudakis, "Photocurrent enhancement in hybrid nanocrystal quantum-dot p-i-n photovoltaic devices," *Physical Review Letters*, vol. 102, no. 7, pp. 1–4, 2009.

[43] S. Chanyawadee, R. T. Harley, D. Taylor, M. Henini, A. S. Susha, A. L. Rogach, and P. G. Lagoudakis, "Efficient light harvesting in hybrid CdTe nanocrystal/bulk GaAs p-i-n photovoltaic devices," *Applied Physics Letters*, vol. 94, no. 23, 2009.

[44] M. Brossard, C.-Y. Hong, M. Hung, P. Yu, M. D. B. Charlton, P. G. Savvidis, and P. G. Lagoudakis, "Novel Non-radiative Exciton Harvesting Scheme Yields a 15% Efficiency Improvement in High-Efficiency III-V Solar Cells," *Advanced Optical Materials*, vol. 3, pp. 263–269, 2 2015.

[45] S. Chanyawadee, P. G. Lagoudakis, R. T. Harley, M. D. B. Charlton, D. V. Talapin, H. W. Huang, and C. H. Lin, "Increased color-conversion efficiency in hybrid light-emitting diodes utilizing non-radiative energy transfer," *Advanced Materials*, vol. 22, no. 5, pp. 602–606, 2010.

[46] C. Krishnan, M. Brossard, K.-Y. Lee, J.-K. Huang, C.-H. Lin, H.-C. Kuo, M. D. B. Charlton, and P. G. Lagoudakis, "Hybrid photonic crystal light-emitting diode renders 123% color conversion effective quantum yield," *Optica*, vol. 3, no. 5, p. 503, 2016.

[47] T. Trupke, M. A. Green, and P. Würfel, "Improving solar cell efficiencies by up-conversion of sub-band-gap light," *Journal of Applied Physics*, vol. 92, no. 7, pp. 4117–4122, 2002.

[48] K. R. Catchpole and A. Polman, "Plasmonic solar cells.," *Optics express*, vol. 16, no. 26, pp. 21793–800, 2008.

[49] P. Y. Yu and M. Cardona, *Fundamentals of Semiconductors*. Springer, 2005.

[50] C. Kittel, *Introduction to solid state physics*. Wiley, sixth ed., 1986.

[51] R. J. Elliott, "Intensity of optical absorption by excitons," *Physical Review*, vol. 108, no. 6, pp. 1384–1389, 1957.

[52] Schmidt, Lischka, and Zulehner, "Excitation-power dependence of the near-band-edge photoluminescence of semiconductors.," *Physical review. B, Condensed matter*, vol. 45, no. 16, pp. 8989–8994, 1992.

[53] H. Shibata, M. Sakai, A. Yamada, K. Matsubara, K. Sakurai, H. Tampo, S. Ishizuka, K. K. Kim, and S. Niki, "Excitation-power dependence of free exciton photoluminescence of semiconductors," *Japanese Journal of Applied Physics*, vol. 44, pp. 6113–6114, 8 2005.

[54] A. Polman, M. Knight, E. C. Garnett, B. Ehrler, and W. C. Sinke, "Photovoltaic materials: Present efficiencies and future challenges," *Science*, vol. 352, pp. aad4424–aad4424, 4 2016.

[55] J. Nelson, *The Physics of Solar Cells*. Series on Properties of Semiconductor Materials, Imperial College Press, 2003.

[56] A. R. Beattie and P. T. Landsberg, "Auger Effect in Semiconductors," *Proceedings of the Royal Society A: Mathematical, Physical and Engineering Sciences*, vol. 249, no. 1256, pp. 16–29, 1959.

[57] L. M. Herz, "Charge-Carrier Dynamics in Organic-Inorganic Metal Halide Perovskites," *Annual Review of Physical Chemistry*, vol. 67, no. 1, pp. 65–89, 2016.

[58] O. D. Miller and E. Yablonovitch, "Photon extraction: the key physics for approaching solar cell efficiency limits," *SPIE Active Photonics V*, vol. 8808, pp. 1–10, 2013.

[59] O. D. Miller, E. Yablonovitch, and S. R. Kurtz, "Strong internal and external luminescence as solar cells approach the Shockley-Queisser limit," *IEEE Journal of Photovoltaics*, vol. 2, no. 3, pp. 303–311, 2012.

[60] R. T. Ross, "Some thermodynamics of photochemical systems," *The Journal of Chemical Physics*, vol. 46, pp. 4590–4593, 6 1967.

[61] V. M. Goldschmidt, "Die Gesetze der Krystallochemie," *Die Naturwissenschaften*, vol. 14, pp. 477–485, 5 1926.

[62] M. a. Green, A. Ho-Baillie, and H. J. Snaith, "The emergence of perovskite solar cells," *Nature Photonics*, vol. 8, no. 7, pp. 506–514, 2014.

[63] E. T. Hoke, D. J. Slotcavage, E. R. Dohner, A. R. Bowring, H. I. Karunadasa, and M. D. McGehee, "Reversible photo-induced trap formation in mixed-halide hybrid perovskites for photovoltaics," *Chemical Science*, vol. 6, no. 1, pp. 613–617, 2015.

[64] T. Baikie, Y. Fang, J. M. Kadro, M. Schreyer, F. Wei, S. G. Mhaisalkar, M. Graetzel, and T. J. White, "Synthesis and crystal chemistry of the hybrid perovskite (CH3NH3)PbI3 for solid-state sensitised solar cell applications," *Journal of Materials Chemistry A*, vol. 1, no. 18, pp. 5628–5641, 2013.

[65] Y. Kawamura, H. Mashiyama, and K. Hasebe, "Structural Study on CubicTetragonal Transition of CH 3 NH 3 PbI 3," *Journal of the Physical Society of Japan*, vol. 71, no. 7, pp. 1694–1697, 2002.

[66] A. Poglitsch and D. Weber, "Dynamic disorder in methylammoniumtrihalogenoplumbates (II) observed by millimeter-wave spectroscopy," *The Journal of Chemical Physics*, vol. 87, no. 11, p. 6373, 1987.

[67] W. Kong, Z. Ye, Z. Qi, B. Zhang, M. Wang, A. Rahimi-Iman, and H. Wu, "Characterization of an abnormal photoluminescence behavior upon crystal-phase transition of perovskite CH3NH3PbI3," *Phys. Chem. Chem. Phys.*, 5 2015.

[68] G. M. Piana, C. G. Bailey, and P. G. Lagoudakis, "Phonon-assisted Trapping and Re-excitation of Free Carriers and Excitons in Lead Halide Perovskites," *The Journal of Physical Chemistry C*, vol. 37, p. acs.jpcc.9b06712, 2019.

[69] L. Q. Phuong, Y. Yamada, M. Nagai, N. Maruyama, A. Wakamiya, and Y. Kanemitsu, "Free Carriers Versus Excitons in CH3NH3PbI3 Perovskite Thin Films at Low Temperatures: Charge Transfer From the Orthorhombic Phase to the Tetragonal Phase," *The Journal of Physical Chemistry Letters*, p. acs.jpclett.6b00781, 6 2016.

[70] C. Sheng, C. Zhang, Y. Zhai, K. Mielczarek, W. Wang, W. Ma, A. Zakhidov, and Z. V. Vardeny, "Exciton versus Free Carrier Photogeneration in Organometal Trihalide Perovskites Probed by Broadband Ultrafast Polarization Memory Dynamics," *Physical Review Letters*, vol. 114, p. 116601, 3 2015.

[71] A. Miyata, A. Mitioglu, P. Plochocka, O. Portugall, J. T.-W. Wang, S. D. Stranks, H. J. Snaith, and R. J. Nicholas, "Direct measurement of the exciton binding energy and effective masses for charge carriers in organic-inorganic tri-halide perovskites," *Nature Physics*, vol. 11, no. 7, pp. 582–587, 2015.

[72] V. D'Innocenzo, G. Grancini, M. J. P. Alcocer, A. R. S. Kandada, S. D. Stranks, M. M. Lee, G. Lanzani, H. J. Snaith, and A. Petrozza, "Excitons versus free charges in organo-lead tri-halide perovskites," *Nature communications*, vol. 5, p. 3586, 4 2014.

[73] T. C. Sum, N. Mathews, G. Xing, S. S. Lim, W. K. Chong, D. Giovanni, and H. A. Dewi, "Spectral Features and Charge Dynamics of Lead Halide Perovskites: Origins and Interpretations," *Accounts of chemical research*, vol. 49, p. 294302, 1 2016.

[74] J. S. Manser and P. V. Kamat, "Band filling with free charge carriers in organometal halide perovskites," *Nat. Photonics*, vol. 8, no. August, p. Ahead of Print, 2014.

[75] R. L. Milot, G. E. Eperon, H. J. Snaith, M. B. Johnston, and L. M. Herz, "Temperature-Dependent Charge-Carrier Dynamics in CH3NH3PbI3 Perovskite Thin Films," *Advanced Functional Materials*, vol. 25, p. 62186227, 9 2015.

[76] S. D. Stranks, V. M. Burlakov, T. Leijtens, J. M. Ball, A. Goriely, and H. J. Snaith, "Recombination Kinetics in Organic-Inorganic Perovskites: Excitons, Free Charge, and Subgap States," *Physical Review Applied*, vol. 2, p. 034007, 9 2014.

[77] K. T. Munson, C. Grieco, E. Kennehan, R. J. Stewart, and J. B. Asbury, "Time-Resolved Infrared Spectroscopy Directly Probes Free and Trapped Carriers in Organo-Halide Perovskites," *ACS Energy Letters*, p. acsenergylett.7b00033, 2017.

[78] E. M. Hutter, M. C. Gélvez-Rueda, A. Osherov, V. Bulović, F. C. Grozema, S. D. Stranks, and T. J. Savenije, "Directindirect character of the bandgap in methylammonium lead iodide perovskite," *Nature Materials*, vol. 16, no. October 2016, p. In press, 2016.

[79] Y. Yang, M. Yang, Z. Li, R. Crisp, K. Zhu, and M. C. Beard, "Comparison of Recombination Dynamics in CH3NH3PbBr3 and CH3NH3PbI3 Perovskite Films: Influence of Exciton Binding Energy," *Journal of Physical Chemistry Letters*, vol. 6, no. 23, pp. 4688–4692, 2015.

[80] T. J. Savenije, C. S. Ponseca, L. Kunneman, M. Abdellah, K. Zheng, Y. Tian, Q. Zhu, S. E. Canton, I. G. Scheblykin, T. Pullerits, A. Yartsev, and V. Sundström, "Thermally activated exciton dissociation and recombination control the carrier dynamics in organometal halide perovskite," *Journal of Physical Chemistry Letters*, vol. 5, pp. 2189–2194, 6 2014.

[81] Y. Yamada, T. Nakamura, M. Endo, A. Wakamiya, and Y. Kanemitsu, "Photoelectronic responses in solution-processed perovskite CH3NH3PbI3 solar cells studied by photoluminescence and photoabsorption spectroscopy," *IEEE Journal of Photovoltaics*, vol. 5, pp. 401–405, 1 2015.

[82] Y. Yang, D. P. Ostrowski, R. M. France, K. Zhu, J. van de Lagemaat, J. M. Luther, and M. C. Beard, "Observation of a hot-phonon bottleneck in lead-iodide perovskites," *Nature Photonics*, vol. advance on, no. October, pp. 1–7, 2015.

[83] Q. Lin, A. Armin, R. Chandra, R. R. C. R. Nagiri, P. L. Burn, and P. Meredith, "Electro-optics of perovskite solar cells," *Nature Photonics*, vol. 9, p. 106112, 12 2014.

[84] E. Menéndez-Proupin, P. Palacios, P. Wahnón, and J. C. Conesa, "Self-consistent relativistic band structure of the CH3NH3PbI3 perovskite," *Physical Review B*, vol. 90, p. 045207, 7 2014.

[85] K. Tanaka, T. Takahashi, T. Ban, T. Kondo, K. Uchida, and N. Miura, "Comparative Study in the Excitons in Lead- Halide based Perovskite-type Crystals

CH3NH3PbBr3 CH3NH3PbI3," *Solid State Communications*, vol. 127, pp. 619–623, 9 2003.

[86] M. Cadelano, M. Saba, N. Sestu, V. Sarritzu, D. Marongiu, F. Chen, R. Piras, F. Quochi, A. Mura, and G. Bongiovanni, "Photoexcitations and Emission Processes in Organometal Trihalide Perovskites," in *Perovskite Materials - Synthesis, Characterisation, Properties, and Applications*, ch. 12, InTech, 2016.

[87] H. He, Q. Yu, H. Li, J. Li, J. Si, Y. Jin, N. Wang, J. Wang, J. He, X. Wang, Y. Zhang, and Z. Ye, "Exciton localization in solution-processed organolead trihalide perovskites," *Nature Communications*, vol. 7, pp. 1–7, 2016.

[88] J. Even, L. Pedesseau, and C. Katan, "Analysis of multivalley and multibandgap absorption and enhancement of free carriers related to exciton screening in hybrid perovskites," *Journal of Physical Chemistry C*, vol. 118, no. 22, pp. 11566–11572, 2014.

[89] M. Saba, F. Quochi, A. Mura, and G. Bongiovanni, "Excited State Properties of Hybrid Perovskites," *Accounts of Chemical Research*, vol. 49, no. 1, pp. 166–173, 2016.

[90] J. M. Frost and A. Walsh, "What Is Moving in Hybrid Halide Perovskite Solar Cells?," *Accounts of Chemical Research*, vol. 49, no. 3, pp. 528–535, 2016.

[91] C. Motta, F. El-Mellouhi, S. Kais, N. Tabet, F. Alharbi, and S. Sanvito, "Revealing the role of organic cations in hybrid halide perovskite CH3NH3PbI3," *Nature Communications*, vol. 6, p. 7026, 4 2015.

[92] C. Wehrenfennig, M. Liu, H. J. Snaith, M. B. Johnston, and L. M. Herz, "Charge carrier recombination channels in the low-temperature phase of organic-inorganic lead halide perovskite thin films," *APL Materials*, vol. 2, no. 8, 2014.

[93] J. Even, L. Pedesseau, J. M. Jancu, and C. Katan, "Importance of spin-orbit coupling in hybrid organic/inorganic perovskites for photovoltaic applications," *Journal of Physical Chemistry Letters*, vol. 4, no. 17, pp. 2999–3005, 2013.

[94] J. Ma and L. W. Wang, "Nanoscale charge localization induced by random orientations of organic molecules in hybrid perovskite CH3NH3PbI3," *Nano Letters*, vol. 15, no. 1, pp. 248–253, 2015.

[95] R. E. Wasylishen, O. Knop, and J. B. Macdonald, "Cation rotation in methylammonium lead halides," *Solid State Communications*, vol. 56, pp. 581–582, 11 1985.

[96] J. Even, L. Pedesseau, C. Katan, M. Kepenekian, J. S. Lauret, D. Sapori, and E. Deleporte, "Solid-state physics perspective on hybrid perovskite semiconductors," *Journal of Physical Chemistry C*, vol. 119, no. 19, pp. 10161–10177, 2015.

[97] Y. Yamada, T. Nakamura, M. Endo, A. Wakamiya, and Y. Kanemitsu, "Near-band-edge optical responses of solution-processed organic-inorganic hybrid perovskite CH3NH3PbI3 on mesoporous Tio2 electrodes," *Applied Physics Express*, vol. 7, p. 032302, 3 2014.

[98] M. Grundman, *The Physics of Semiconductors: An Introduction Including Devices and Nanophysics*. Springer, 2006.

[99] M. Gurioli, A. Vinattieri, M. Colocci, C. Deparis, J. Massies, G. Neu, A. Bosacchi, and S. Franchi, "Temperature dependence of interface recombination and radiative recombination in (Al, Ga)As heterostructures," *Applied Physics Letters*, vol. 42, pp. 813–815, 5 1983.

[100] Y. Yamada, T. Nakamura, M. Endo, A. Wakamiya, and Y. Kanemitsu, "Photocarrier Recombination Dynamics in Perovskite CH3NH3PbI3 for Solar Cell Applications," *Journal of the American Chemical Society*, vol. 136, pp. 11610–3, 8 2014.

[101] X. Wen, Y. Feng, S. Huang, F. Huang, Y.-B. Cheng, M. Green, and A. Ho-Baillie, "Defect trapping states and charge carrier recombination in organicinorganic halide perovskites," *J. Mater. Chem. C*, vol. 4, pp. 793–800, 12 2016.

[102] D. Shi, V. Adinolfi, R. Comin, M. Yuan, E. Alarousu, A. Buin, Y. Chen, S. Hoogland, A. Rothenberger, K. Katsiev, Y. Losovyj, X. Zhang, P. A. Dowben, O. F.

Mohammed, E. H. Sargent, and O. M. Bakr, "Low trap-state density and long carrier diffusion in organolead trihalide perovskite single crystals.," *Science (New York, N.Y.)*, vol. 347, no. 6221, pp. 519–22, 2015.

[103] P. Azarhoosh, J. M. Frost, S. McKechnie, A. Walsh, and M. van Schilfgaarde, "Relativistic origin of slow electron-hole recombination in hybrid halide perovskite solar cells," *arXiv*, pp. 1–17, 2016.

[104] F. Zheng, L. Z. Tan, S. Liu, and A. M. Rappe, "Rashba spin-orbit coupling enhanced carrier lifetime in CH3NH3PbI3," *Nano Letters*, vol. 15, no. 12, pp. 7794–7800, 2015.

[105] T. Etienne, E. Mosconi, and F. De Angelis, "Dynamical Origin of the Rashba Effect in Organohalide Lead Perovskites: A Key to Suppressed Carrier Recombination in Perovskite Solar Cells?," *Journal of Physical Chemistry Letters*, vol. 7, pp. 1638–1645, 4 2016.

[106] Z. G. Yu, "Rashba Effect and Carrier Mobility in Hybrid Organic-Inorganic Perovskites," *Journal of Physical Chemistry Letters*, vol. 7, no. 16, pp. 3078–3083, 2016.

[107] M. Saba, M. Cadelano, D. Marongiu, F. Chen, V. Sarritzu, N. Sestu, C. Figus, M. Aresti, R. Piras, A. Geddo Lehmann, C. Cannas, A. Musinu, F. Quochi, A. Mura, and G. Bongiovanni, "Correlated electron-hole plasma in organometal perovskites.," *Nature communications*, vol. 5, no. May, p. 5049, 2014.

[108] G. Xing, N. Mathews, S. Sun, S. S. Lim, Y. M. Lam, M. Grätzel, S. Mhaisalkar, and T. C. Sum, "Long-Range Balanced Electron- and Hole-Transport Lengths in Organic-Inorganic CH3NH3PbI3," *Science*, vol. 342, pp. 344 LP – 347, 10 2013.

[109] W. Nie, H. Tsai, R. Asadpour, J.-C. Blancon, A. J. Neukirch, G. Gupta, J. J. Crochet, M. Chhowalla, S. Tretiak, M. A. Alam, H.-L. Wang, and A. D. Mohite, "High-efficiency solution-processed perovskite solar cells with millimeter-scale grains," *Science*, vol. 347, no. 6221, pp. 522–525, 2015.

[110] H. Zhou, Q. Chen, G. Li, S. Luo, T. B. Song, H. S. Duan, Z. Hong, J. You, Y. Liu, and Y. Yang, "Interface engineering of highly efficient perovskite solar cells," *Science*, vol. 345, no. 6196, pp. 542–546, 2014.

[111] H. Oga, A. Saeki, Y. Ogomi, S. Hayase, and S. Seki, "Improved understanding of the electronic and energetic landscapes of perovskite solar cells: High local charge carrier mobility, reduced recombination, and extremely shallow traps," *Journal of the American Chemical Society*, vol. 136, no. 39, pp. 13818–13825, 2014.

[112] D. W. de Quilettes, S. M. Vorpahl, S. D. Stranks, H. Nagaoka, G. E. Eperon, M. E. Ziffer, H. J. Snaith, and D. S. Ginger, "Impact of microstructure on local carrier lifetime in perovskite solar cells," *Science*, vol. 348, no. 6235, pp. 683–686, 2015.

[113] F. X. Xie, H. Su, J. Mao, K. S. Wong, and W. C. H. Choy, "Evolution of diffusion length and trap state induced by chloride in perovskite solar cell," *Journal of Physical Chemistry C*, vol. 120, no. 38, pp. 21248–21253, 2016.

[114] E. Mosconi, D. Meggiolaro, H. Snaith, S. D. Stranks, and F. De Angelis, "Light-induced Annihilation of Frenkel Defects in Organo-Lead Halide Perovskites," *Energy Environ. Sci.*, vol. 9, pp. 1–7, 2016.

[115] J. M. Azpiroz, E. Mosconi, J. Bisquert, and F. De Angelis, "Defect migration in methylammonium lead iodide and its role in perovskite solar cell operation," *Energy Environ. Sci.*, vol. 8, no. 7, pp. 2118–2127, 2015.

[116] D. W. deQuilettes, W. Zhang, V. M. Burlakov, D. J. Graham, T. Leijtens, A. Osherov, V. Bulović, H. J. Snaith, D. S. Ginger, and S. D. Stranks, "Photo-induced halide redistribution in organicinorganic perovskite films," *Nature Communications*, vol. 7, p. 11683, 5 2016.

[117] J. F. Galisteo-López, M. Anaya, M. E. Calvo, and H. Míguez, "Environmental effects on the photophysics of organic-inorganic halide perovskites," *Journal of Physical Chemistry Letters*, vol. 6, no. 12, pp. 2200–2205, 2015.

[118] Y. Tian, M. Peter, E. Unger, M. Abdellah, K. Zheng, T. Pullerits, A. Yartsev, V. Sundström, and I. G. Scheblykin, "Mechanistic insights into perovskite photoluminescence enhancement: light curing with oxygen can boost yield thousandfold," *Physical chemistry chemical physics : PCCP*, vol. 17, no. 38, pp. 24978–24987, 2015.

[119] S. G. Motti, M. Gandini, A. J. Barker, J. M. Ball, A. R. Srimath Kandada, and A. Petrozza, "Photoinduced Emissive Trap States in Lead Halide Perovskite Semiconductors," *ACS Energy Letters*, pp. 726–730, 2016.

[120] J. Li, Q. Yu, B. Lu, H. He, and Z. Ye, "Ambience dependent photoluminescence reveals the localization and trap filling effects in CH3NH3PbI3-xClx perovskite films," *J. Mater. Chem. C*, vol. 5, pp. 54–58, 2016.

[121] X. Feng, H. Su, Y. Wu, H. Wu, J. Xie, X. Liu, J. Fan, J. Dai, and Z. He, "Photon-generated carriers excite superoxide species inducing long-term photoluminescence enhancement of MAPbI3 perovskite single crystals," *Journal of Materials Chemistry A*, vol. 5, no. 24, pp. 12048–12053, 2017.

[122] N. Aristidou, I. Sanchez-Molina, T. Chotchuangchutchaval, M. Brown, L. Martinez, T. Rath, and S. A. Haque, "The Role of Oxygen in the Degradation of Methylammonium Lead Trihalide Perovskite Photoactive Layers," *Angewandte Chemie - International Edition*, vol. 54, pp. 8208–8212, 7 2015.

[123] D. Bryant, N. Aristidou, S. Pont, I. Sanchez-Molina, T. Chotchuangchutchaval, S. Wheeler, J. R. Durrant, and S. A. Haque, "Light and oxygen induced degradation limits the operational stability of methylammonium lead triiodide perovskite solar cells," *Energy Environ. Sci.*, vol. 9, no. 5, pp. 1850–1850, 2016.

[124] S. Draguta, S. Thakur, Y. V. Morozov, Y. Wang, J. S. Manser, P. V. Kamat, and M. Kuno, "Spatially Non-uniform Trap State Densities in Solution-Processed Hybrid Perovskite Thin Films.," *The journal of physical chemistry letters*, pp. 715–721, 2 2016.

[125] H. Gerischer, M. Michel-Beyerle, F. Rebentrost, and H. Tributsch, "Sensitization of charge injection into semiconductors with large band gap," *Electrochimica Acta*, vol. 13, pp. 1509–1515, 6 1968.

[126] B. O'Regan and M. Grätzel, "A low-cost, high-efficiency solar cell based on dye-sensitized colloidal TiO2 films," *Nature*, vol. 353, pp. 737–740, 10 1991.

[127] M. M. Lee, J. Teuscher, T. Miyasaka, T. N. Murakami, and H. J. Snaith, "Efficient hybrid solar cells based on meso-superstructured organometal halide perovskites," *Science*, vol. 338, pp. 643–647, 11 2012.

[128] S. Sun, T. Salim, N. Mathews, M. Duchamp, C. Boothroyd, G. Xing, T. C. Sum, and Y. M. Lam, "The origin of high efficiency in low-temperature solution-processable bilayer organometal halide hybrid solar cells," *Energy & Environmental Science*, vol. 7, no. 1, p. 399, 2014.

[129] Z. Song, S. C. Watthage, A. B. Phillips, and M. J. Heben, "Pathways toward high-performance perovskite solar cells: review of recent advances in organo-metal halide perovskites for photovoltaic applications," *Journal of Photonics for Energy*, vol. 6, no. 2, p. 22001, 2016.

[130] W. S. Yang, J. H. Noh, N. J. Jeon, Y. C. Kim, S. Ryu, J. Seo, and S. I. Seok, "High-performance photovoltaic perovskite layers fabricated through intramolecular exchange," *Science*, vol. 348, no. 6240, 2015.

[131] W. Chen, Y. Wu, Y. Yue, J. Liu, W. Zhang, X. Yang, H. Chen, E. Bi, I. Ashraful, M. Grätzel, and L. Han, "Efficient and stable large-area perovskite solar cells with inorganic charge extraction layers," *Science*, vol. 350, no. 6263, pp. 944–948, 2015.

[132] J. You, L. Meng, T. B. Song, T. F. Guo, W. H. Chang, Z. Hong, H. Chen, H. Zhou, Q. Chen, Y. Liu, N. De Marco, and Y. Yang, "Improved air stability of perovskite solar cells via solution-processed metal oxide transport layers," *Nature Nanotechnology*, vol. 11, no. 1, pp. 75–81, 2016.

[133] H. Yu, F. Wang, F. Xie, W. Li, J. Chen, and N. Zhao, "The role of chlorine in the formation process of "CH3NH3PbI3-xClx" perovskite," *Advanced Functional Materials*, vol. 24, no. 45, pp. 7102–7108, 2014.

[134] Q. Chen, H. Zhou, Y. Fang, A. Z. Stieg, T.-B. Song, H.-H. Wang, X. Xu, Y. Liu, S. Lu, J. You, P. Sun, J. McKay, M. S. Goorsky, and Y. Yang, "The optoelectronic role of chlorine in CH3NH3PbI3(Cl)-based perovskite solar cells," *Nature Communications*, vol. 6, p. 7269, 2015.

[135] Y. Tidhar, E. Edri, H. Weissman, D. Zohar, G. Hodes, D. Cahen, B. Rybtchinski, and S. Kirmayer, "Crystallization of methyl ammonium lead halide perovskites: Implications for photovoltaic applications," *Journal of the American Chemical Society*, vol. 136, pp. 13249–13256, 9 2014.

[136] S. Colella, E. Mosconi, P. Fedeli, A. Listorti, F. Gazza, F. Orlandi, P. Ferro, T. Besagni, A. Rizzo, G. Calestani, G. Gigli, F. De Angelis, and R. Mosca, "MAPbI3-xClx mixed halide perovskite for hybrid solar cells: The role of chloride as dopant on the transport and structural properties," *Chemistry of Materials*, vol. 25, pp. 4613–4618, 11 2013.

[137] D. T. Moore, H. Sai, K. W. Tan, L. A. Estroff, and U. Wiesner, "Impact of the organic halide salt on final perovskite composition for photovoltaic applications," *APL Materials*, vol. 2, no. 8, 2014.

[138] C. C. Stoumpos, C. D. Malliakas, and M. G. Kanatzidis, "Semiconducting tin and lead iodide perovskites with organic cations: Phase transitions, high mobilities, and near-infrared photoluminescent properties," *Inorganic Chemistry*, vol. 52, pp. 9019–9038, 8 2013.

[139] R. J. Sutton, G. E. Eperon, L. Miranda, E. S. Parrott, B. A. Kamino, J. B. Patel, M. T. Hörantner, M. B. Johnston, A. A. Haghighirad, D. T. Moore, and H. J. Snaith, "Bandgap-Tunable Cesium Lead Halide Perovskites with High Thermal Stability for Efficient Solar Cells," *Advanced Energy Materials*, pp. n/a–n/a, 1 2016.

[140] M. Kulbak, S. Gupta, N. Kedem, I. Levine, T. Bendikov, G. Hodes, and D. Cahen, "Cesium Enhances Long-Term Stability of Lead Bromide Perovskite-Based Solar Cells," *The Journal of Physical Chemistry Letters*, vol. 7, pp. 167–172, 1 2016.

[141] L. Protesescu, S. Yakunin, M. I. Bodnarchuk, F. Krieg, R. Caputo, C. H. Hendon, R. X. Yang, A. Walsh, and M. V. Kovalenko, "Nanocrystals of Cesium Lead Halide Perovskites (CsPbX3, X = Cl, Br, and I): Novel Optoelectronic Materials Showing Bright Emission with Wide Color Gamut," *Nano Letters*, vol. 15, no. 6, pp. 3692–3696, 2015.

[142] Q. A. Akkerman, V. D'Innocenzo, S. Accornero, A. Scarpellini, A. Petrozza, M. Prato, and L. Manna, "Tuning the optical properties of cesium lead halide perovskite nanocrystals by anion exchange reactions," *Journal of the American Chemical Society*, vol. 137, no. 32, pp. 10276–10281, 2015.

[143] G. Nedelcu, L. Protesescu, S. Yakunin, M. I. Bodnarchuk, M. J. Grotevent, and M. V. Kovalenko, "Fast Anion-Exchange in Highly Luminescent Nanocrystals of Cesium Lead Halide Perovskites (CsPbX¡inf¿3¡/inf¿, X = Cl, Br, I)," *Nano Letters*, vol. 15, pp. 5635–5640, 8 2015.

[144] N. K. Noel, S. N. Habisreutinger, B. Wenger, M. T. Klug, M. T. Hörantner, M. B. Johnston, R. J. Nicholas, D. T. Moore, and H. J. Snaith, "A low viscosity, low boiling point, clean solvent system for the rapid crystallisation of highly specular perovskite films," *Energy Environ. Sci.*, vol. 10, no. 1, pp. 145–152, 2017.

[145] H.-S. Kim, C.-R. Lee, J.-H. Im, K.-B. Lee, T. Moehl, A. Marchioro, S.-J. Moon, R. Humphry-Baker, J.-H. Yum, J. E. Moser, M. Grätzel, and N.-G. Park, "Lead Iodide Perovskite Sensitized All-Solid-State Submicron Thin Film Mesoscopic Solar Cell with Efficiency Exceeding 9%," *Scientific Reports*, vol. 2, p. 591, 1 2012.

[146] B. Conings, A. Babayigit, M. T. Klug, S. Bai, N. Gauquelin, N. Sakai, J. T.-W. Wang, J. Verbeeck, H.-G. Boyen, and H. J. Snaith, "A Universal Deposition Protocol for Planar Heterojunction Solar Cells with High Efficiency Based on Hybrid Lead Halide Perovskite Families," *Advanced Materials*, pp. 1–9, 2016.

[147] N. J. Jeon, J. H. Noh, Y. C. Kim, W. S. Yang, S. Ryu, and S. I. Seok, "Solvent engineering for high-performance inorganic-organic hybrid perovskite solar cells.," *Nature materials*, vol. 13, no. July, pp. 1–7, 2014.

[148] J. Burschka, N. Pellet, S.-J. Moon, R. Humphry-Baker, P. Gao, M. K. Nazeeruddin, and M. Grätzel, "Sequential deposition as a route to high-performance perovskite-sensitized solar cells.," *Nature*, vol. 499, no. 7458, pp. 316–320, 2013.

[149] Q. Chen, H. Zhou, Z. Hong, S. Luo, H. S. Duan, H. H. Wang, Y. Liu, G. Li, and Y. Yang, "Planar heterojunction perovskite solar cells via vapor-assisted solution process," *Journal of the American Chemical Society*, vol. 136, pp. 622–625, 1 2014.

[150] F. Huang, Y. Dkhissi, W. Huang, M. Xiao, I. Benesperi, S. Rubanov, Y. Zhu, X. Lin, L. Jiang, Y. Zhou, A. Gray-Weale, J. Etheridge, C. R. McNeill, R. A. Caruso, U. Bach, L. Spiccia, and Y. B. Cheng, "Gas-assisted preparation of lead iodide perovskite films consisting of a monolayer of single crystalline grains for high efficiency planar solar cells," *Nano Energy*, vol. 10, pp. 10–18, 2014.

[151] H. Miyamae, Y. Numahata, and M. Nagata, "THE CRYSTAL STRUCTURE OF LEAD(II) IODIDE-DIMETHYLSULPHOXIDE(1/2), PbI ¡sub¿2¡/sub¿ (dmso) ¡sub¿2¡/sub¿," *Chemistry Letters*, vol. 9, pp. 663–664, 6 1980.

[152] J. Zheng, M. Zhang, C. F. J. Lau, X. Deng, J. Kim, Q. Ma, C. Chen, M. A. Green, S. Huang, and A. W. Ho-Baillie, "Spin-coating free fabrication for highly efficient perovskite solar cells," *Solar Energy Materials and Solar Cells*, vol. 168, no. February, pp. 165–171, 2017.

[153] M. Liu, M. B. Johnston, and H. J. Snaith, "Efficient planar heterojunction perovskite solar cells by vapour deposition," *Nature*, vol. 501, no. 7467, pp. 395–398, 2013.

[154] H. Hu, D. Wang, Y. Zhou, J. Zhang, S. Lv, S. Pang, X. Chen, Z. Liu, N. P. Padture, and G. Cui, "Vapour-based processing of hole-conductor-free CH 3 NH 3 PbI 3 perovskite/C 60 fullerene planar solar cells," *RSC Advances*, vol. 4, p. 28964, 7 2014.

[155] M. R. Leyden, L. K. Ono, S. R. Raga, Y. Kato, S. Wang, and Y. Qi, "High performance perovskite solar cells by hybrid chemical vapor deposition," *J. Mater. Chem. A*, vol. 2, no. 44, pp. 18742–18745, 2014.

[156] A. Barrows, A. Pearson, C. Kwak, A. Dunbar, A. Buckley, and D. Lidzey, "Efficient planar heterojunction mixed-halide perovskite solar cells deposited via spray-deposition," *Energy & Environmental Science*, vol. 7, pp. 1–7, 2014.

[157] S. Das, B. Yang, G. Gu, P. C. Joshi, I. N. Ivanov, C. M. Rouleau, T. Aytug, D. B. Geohegan, and K. Xiao, "High-Performance Flexible Perovskite Solar Cells by Using a Combination of Ultrasonic Spray-Coating and Low Thermal Budget Photonic Curing," *ACS Photonics*, vol. 2, pp. 680–686, 6 2015.

[158] J. G. Tait, S. Manghooli, W. Qiu, L. Rakocevic, L. Kootstra, M. Jaysankar, C. A. Masse de la Huerta, U. W. Paetzold, R. Gehlhaar, D. Cheyns, P. Heremans, and J. Poortmans, "Rapid composition screening for perovskite photovoltaics via concurrently pumped ultrasonic spray coating," *J. Mater. Chem. A*, vol. 4, no. 10, pp. 3792–3797, 2016.

[159] K. Hwang, Y. S. Jung, Y. J. Heo, F. H. Scholes, S. E. Watkins, J. Subbiah, D. J. Jones, D. Y. Kim, and D. Vak, "Toward large scale roll-to-roll production of fully printed perovskite solar cells," *Advanced Materials*, vol. 27, no. 7, pp. 1241–1247, 2015.

[160] G. Cotella, J. Baker, D. Worsley, F. De Rossi, C. Pleydell-Pearce, M. Carnie, and T. Watson, "One-step deposition by slot-die coating of mixed lead halide perovskite for photovoltaic applications," *Solar Energy Materials and Solar Cells*, vol. 159, pp. 362–369, 2017.

[161] S.-G. Li, K.-J. Jiang, M.-J. Su, X.-P. Cui, J.-H. Huang, Q.-Q. Zhang, X.-Q. Zhou, L.-M. Yang, and Y.-L. Song, "Inkjet printing of CH 3 NH 3 PbI 3 on a mesoscopic TiO 2 film for highly efficient perovskite solar cells," *J. Mater. Chem. A*, vol. 3, no. 17, pp. 9092–9097, 2015.

[162] M. Bag, Z. Jiang, L. A. Renna, S. P. Jeong, V. M. Rotello, and D. Venkataraman, "Rapid combinatorial screening of inkjet-printed alkyl-ammonium cations in perovskite solar cells," *Materials Letters*, vol. 164, pp. 472–475, 2016.

[163] K. A. Bush, C. D. Bailie, Y. Chen, A. R. Bowring, W. Wang, W. Ma, T. Leijtens, F. Moghadam, and M. D. McGehee, "Thermal and Environmental Stability

of Semi-Transparent Perovskite Solar Cells for Tandems Enabled by a Solution-Processed Nanoparticle Buffer Layer and Sputtered ITO Electrode," *Advanced Materials*, vol. 28, no. 20, pp. 3937–3943, 2016.

[164] D. Bryant, P. Greenwood, J. Troughton, M. Wijdekop, M. Carnie, M. Davies, K. Wojciechowski, H. J. Snaith, T. Watson, and D. Worsley, "A transparent conductive adhesive laminate electrode for high-efficiency organic-inorganic lead halide perovskite solar cells," *Advanced Materials*, vol. 26, pp. 7499–7504, 11 2014.

[165] U. W. W. Paetzold, M. Jaysankar, R. Gehlhaar, E. Ahlswede, S. Paetel, W. Qiu, J. P. Bastos, L. Rakocevic, B. S. Richards, T. Aernouts, M. Powalla, and J. Poortmans, "Scalable Perovskite/CIGS Thin-Film Solar Module with Power Conversion Efficiency of 17.8%," *J. Mater. Chem. A*, vol. 5, no. 20, pp. 9897–9906, 2017.

[166] J. Song, J. Li, X. Li, L. Xu, Y. Dong, and H. Zeng, "Quantum Dot Light-Emitting Diodes Based on Inorganic Perovskite Cesium Lead Halides (CsPbX3)," *Advanced Materials*, vol. 27, no. 44, pp. 7162–7167, 2015.

[167] G. Li, F. W. R. Rivarola, N. J. Davis, S. Bai, T. C. Jellicoe, F. De La Peña, S. Hou, C. Ducati, F. Gao, R. H. Friend, N. C. Greenham, and Z. K. Tan, "Highly Efficient Perovskite Nanocrystal Light-Emitting Diodes Enabled by a Universal Crosslinking Method," *Advanced Materials*, vol. 28, pp. 3528–3534, 5 2016.

[168] X. Gong, Z. Yang, G. Walters, R. Comin, Z. Ning, E. Beauregard, V. Adinolfi, O. Voznyy, and E. H. Sargent, "Highly efficient quantum dot near-infrared light-emitting diodes," *Nature Photonics*, vol. 10, no. 4, pp. 253–257, 2016.

[169] J.-H. Im, C.-R. Lee, J.-W. Lee, S.-W. Park, and N.-G. Park, "6.5% Efficient Perovskite Quantum-Dot-Sensitized Solar Cell," *Nanoscale*, vol. 3, no. 10, p. 4088, 2011.

[170] Z. Ning, X. Gong, R. Comin, G. Walters, F. Fan, O. Voznyy, E. Yassitepe, A. Buin, S. Hoogland, and E. H. Sargent, "Quantum-dot-in-perovskite solids," *Nature*, vol. 523, pp. 324–328, 7 2015.

[171] Z. Ning, H. Dong, Q. Zhang, O. Voznyy, and E. H. Sargent, "Solar cells based on inks of n-type colloidal quantum dots," *ACS Nano*, vol. 8, no. 10, pp. 10321–10327, 2014.

[172] D. N. Dirin, S. Dreyfuss, M. I. Bodnarchuk, G. Nedelcu, P. Papagiorgis, G. Itskos, and M. V. Kovalenko, "Lead Halide Perovskites and Other Metal Halide Complexes As Inorganic Capping Ligands for Colloidal Nanocrystals," *Journal of the American Chemical Society*, vol. 136, pp. 0–3, 5 2014.

[173] F. P. García De Arquer, X. Gong, R. P. Sabatini, M. Liu, G. H. Kim, B. R. Sutherland, O. Voznyy, J. Xu, Y. Pang, S. Hoogland, D. Sinton, and E. Sargent, "Field-emission from quantum-dot-in-perovskite solids," *Nature Communications*, vol. 8, p. 14757, 2017.

[174] L. Hu, W. Wang, H. Liu, J. Peng, H. Cao, G. Shao, Z. Xia, W. Ma, and J. Tang, "PbS colloidal quantum dots as an effective hole transporter for planar heterojunction perovskite solar cells," *J. Mater. Chem. A*, vol. 3, no. 2, pp. 515–518, 2015.

[175] Y. Li, J. Zhu, Y. Huang, J. Wei, F. Liu, Z. Shao, L. Hu, S. Chen, S. Yang, J. Tang, J. Yao, and S. Dai, "Efficient inorganic solid solar cells composed of perovskite and PbS quantum dots," *Nanoscale*, vol. 7, no. 21, pp. 9902–9907, 2015.

[176] M. Lv, J. Zhu, Y. Huang, Y. Li, Z. Shao, Y. Xu, and S. Dai, "Colloidal CuInS2 Quantum Dots as Inorganic Hole-transporting Material in Perovskite Solar Cells," *ACS Applied Materials & Interfaces*, p. 150717114628002, 2015.

[177] Z. Zhu, Y. Bai, T. Zhang, Z. Liu, X. Long, Z. Wei, Z. Wang, L. Zhang, J. Wang, F. Yan, and S. Yang, "High-performance hole-extraction layer of sol-gel-processed nio nanocrystals for inverted planar perovskite solar cells," *Angewandte Chemie - International Edition*, vol. 53, pp. 12571–12575, 11 2014.

[178] Y. Yang and W. Wang, "Effects of incorporating PbS quantum dots in perovskite solar cells based on CH3NH3PbI3," *Journal of Power Sources*, vol. 293, pp. 577–584, 10 2015.

[179] Z. Zhu, J. Ma, Z. Wang, C. Mu, Z. Fan, L. Du, Y. Bai, L. Fan, H. Yan, D. L. Phillips, and S. Yang, "Efficiency enhancement of perovskite solar cells through fast electron extraction: The role of graphene quantum dots," *Journal of the American Chemical Society*, vol. 136, no. 10, pp. 3760–3763, 2014.

[180] D.-Y. Son, J.-H. Im, H.-S. Kim, and N.-G. Park, "11% Efficient Perovskite Solar Cell Based on ZnO Nanorods: An Effective Charge Collection System," *The Journal of Physical Chemistry C*, vol. 118, p. 140317091621004, 7 2014.

[181] J. R. Lakowicz, *Principles of fluorescence spectroscopy*. Springer Science & Business Media, 2007, 3, illustr ed., 2007.

[182] P. C. Braga and D. Ricci, *Atomic Force Microscopy*. New Jersey: Humana Press, 1 ed., 10 2003.

[183] J. N. H. Harland G. Tompkins, *Spectroscopic Ellipsometry Practical Application to Thin Film Characterization*. Momentum Press, 2016.

[184] M. Di, E. Bersch, A. C. Diebold, S. Consiglio, R. D. Clark, G. J. Leusink, and T. Kaack, "Comparison of methods to determine bandgaps of ultrathin HfO 2 films using spectroscopic ellipsometry," *Journal of Vacuum Science & Technology A: Vacuum, Surfaces, and Films*, vol. 29, p. 041001, 7 2011.

[185] G. E. Jellison and F. A. Modine, "Parameterization of the optical functions of amorphous materials in the interband region," *Applied Physics Letters*, vol. 69, pp. 371–373, 7 1996.

[186] J. P. Correa-Baena, M. Saliba, T. Buonassisi, M. Grätzel, A. Abate, W. Tress, and A. Hagfeldt, "Promises and challenges of perovskite solar cells," *Science*, vol. 358, no. 6364, pp. 739–744, 2017.

[187] W. E. Sha, X. Ren, L. Chen, and W. C. Choy, "The efficiency limit of CH3NH3PbI3 perovskite solar cells," *Applied Physics Letters*, vol. 106, p. 221104, 6 2015.

[188] I. L. Braly, D. W. Dequilettes, L. M. Pazos-Outón, S. Burke, M. E. Ziffer, D. S. Ginger, and H. W. Hillhouse, "Hybrid perovskite films approaching the radiative

limit with over 90% photoluminescence quantum efficiency," *Nature Photonics*, vol. 12, no. 6, pp. 355–361, 2018.

[189] Y. Jiang, I. Almansouri, S. Huang, T. Young, Y. Li, Y. Peng, Q. Hou, L. Spiccia, U. Bach, Y.-B. Cheng, M. Green, and A. Ho-Baillie, "Optical Analysis of Perovskite/Silicon Tandem Solar Cells," *J. Mater. Chem. C*, vol. 4, pp. 5679–5689, 2016.

[190] P. Mantilla-Perez, T. Feurer, J. P. Correa-Baena, Q. Liu, S. Colodrero, J. Toudert, M. Saliba, S. Buecheler, A. Hagfeldt, A. N. Tiwari, and J. Martorell, "Monolithic CIGS-Perovskite Tandem Cell for Optimal Light Harvesting without Current Matching," *ACS Photonics*, vol. 4, no. 4, pp. 861–867, 2017.

[191] M. Shirayama, H. Kadowaki, T. Miyadera, T. Sugita, M. Tamakoshi, M. Kato, T. Fujiseki, D. Murata, S. Hara, T. N. Murakami, S. Fujimoto, M. Chikamatsu, and H. Fujiwara, "Optical Transitions in Hybrid Perovskite Solar Cells: Ellipsometry, Density Functional Theory, and Quantum Efficiency Analyses for CH3NH3PbI3," *Physical Review Applied*, vol. 5, p. 014012, 1 2016.

[192] S. De Wolf, J. Holovsky, S. J. Moon, P. Löper, B. Niesen, M. Ledinsky, F. J. Haug, J. H. Yum, and C. Ballif, "Organometallic halide perovskites: Sharp optical absorption edge and its relation to photovoltaic performance," *Journal of Physical Chemistry Letters*, vol. 5, no. 6, pp. 1035–1039, 2014.

[193] J. Even, L. Pedesseau, and C. Katan, "Analysis of multivalley and multibandgap absorption and enhancement of free carriers related to exciton screening in hybrid perovskites," *Journal of Physical Chemistry C*, vol. 118, no. 22, pp. 11566–11572, 2014.

[194] G. Giorgi, J. I. Fujisawa, H. Segawa, and K. Yamashita, "Small photocarrier effective masses featuring ambipolar transport in methylammonium lead iodide perovskite: A density functional analysis," *Journal of Physical Chemistry Letters*, vol. 4, no. 24, pp. 4213–4216, 2013.

[195] M. E. Ziffer, J. C. Mohammed, and D. S. Ginger, "Electroabsorption Spectroscopy Measurements of the Exciton Binding Energy, Electron-Hole Reduced Effective

Mass, and Band Gap in the Perovskite CH3NH3PbI3," *ACS Photonics*, vol. 3, no. 6, pp. 1060–1068, 2016.

[196] Z. Li, J. Moon, A. Gharajeh, R. Haroldson, R. Hawkins, W. Hu, A. Zakhidov, and Q. Gu, "Room temperature Continuous-Wave Operation of Organometal Halide Perovskite Lasers," *ACS Nano*, vol. 12, pp. 10968–10976, 11 2018.

[197] S. Wang, Y. Liu, G. Li, J. Zhang, N. Zhang, S. Xiao, and Q. Song, "Lead Halide Perovskite Based Microdisk Lasers for On-Chip Integrated Photonic Circuits," *Advanced Optical Materials*, vol. 6, p. 1701266, 3 2018.

[198] K. Wang, W. Sun, J. Li, Z. Gu, S. Xiao, and Q. Song, "Unidirectional Lasing Emissions from CH3NH3PbBr3 Perovskite Microdisks," *ACS Photonics*, vol. 3, pp. 1125–1130, 6 2016.

[199] M. M. Stylianakis, T. Maksudov, A. Panagiotopoulos, G. Kakavelakis, and K. Petridis, "Inorganic and hybrid perovskite based laser devices: A Review," *Materials*, vol. 16, no. 6, pp. 1–28, 2019.

[200] Q. Liao, K. Hu, H. Zhang, X. Wang, J. Yao, and H. Fu, "Perovskite microdisk microlasers self-assembled from solution," *Advanced Materials*, vol. 27, pp. 3405–3410, 6 2015.

[201] H. Zhu, Y. Fu, F. Meng, X. Wu, Z. Gong, Q. Ding, M. V. Gustafsson, M. T. Trinh, S. Jin, and X. Y. Zhu, "Lead halide perovskite nanowire lasers with low lasing thresholds and high quality factors," *Nature Materials*, vol. 14, no. 6, pp. 636–642, 2015.

[202] Z. K. Tan, R. S. Moghaddam, M. L. Lai, P. Docampo, R. Higler, F. Deschler, M. Price, A. Sadhanala, L. M. Pazos, D. Credgington, F. Hanusch, T. Bein, H. J. Snaith, and R. H. Friend, "Bright light-emitting diodes based on organometal halide perovskite," *Nature Nanotechnology*, vol. 9, no. 9, pp. 687–692, 2014.

[203] H. Cho, S. H. Jeong, M. H. Park, Y. H. Kim, C. Wolf, C. L. Lee, J. H. Heo, A. Sadhanala, N. S. Myoung, S. Yoo, S. H. Im, R. H. Friend, and T. W. Lee, "Overcoming the electroluminescence efficiency limitations of perovskite light-emitting diodes," *Science*, vol. 350, pp. 1222–1225, 12 2015.

[204] Y. Ling, Z. Yuan, Y. Tian, X. Wang, J. C. Wang, Y. Xin, K. Hanson, B. Ma, and H. Gao, "Bright Light-Emitting Diodes Based on Organometal Halide Perovskite Nanoplatelets," *Advanced Materials*, vol. 28, pp. 305–311, 1 2016.

[205] J. Liang, Y. Zhang, X. Guo, Z. Gan, J. Lin, Y. Fan, and X. Liu, "Efficient perovskite light-emitting diodes by film annealing temperature control," *RSC Advances*, vol. 6, no. 75, pp. 71070–71075, 2016.

[206] M. I. Saidaminov, V. Adinolfi, R. Comin, A. L. Abdelhady, W. Peng, I. Dursun, M. Yuan, S. Hoogland, E. H. Sargent, and O. M. Bakr, "Planar-integrated single-crystalline perovskite photodetectors," *Nature Communications*, vol. 6, p. 8724, 12 2015.

[207] Y. Fang, Q. Dong, Y. Shao, Y. Yuan, and J. Huang, "Highly narrowband perovskite single-crystal photodetectors enabled by surface-charge recombination," *Nature Photonics*, vol. 9, pp. 679–686, 10 2015.

[208] C. Bao, Z. Chen, Y. Fang, H. Wei, Y. Deng, X. Xiao, L. Li, and J. Huang, "Low-Noise and Large-Linear-Dynamic-Range Photodetectors Based on Hybrid-Perovskite Thin-Single-Crystals," *Advanced Materials*, vol. 29, p. 1703209, 10 2017.

[209] J. M. Ball, S. D. Stranks, M. T. Hörantner, S. Hüttner, W. Zhang, E. J. Crossland, I. Ramirez, M. Riede, M. B. Johnston, R. H. Friend, and H. J. Snaith, "Optical properties and limiting photocurrent of thin-film perovskite solar cells," *Energy and Environmental Science*, vol. 8, no. 2, pp. 602–609, 2015.

[210] X. Ziang, L. Shifeng, Q. Laixiang, P. Shuping, W. Wei, Y. Yu, Y. Li, C. Zhijian, W. Shufeng, D. Honglin, Y. Minghui, and G. G. Qin, "Refractive index and extinction coefficient of CH_3NH_3PbI_3 studied by spectroscopic ellipsometry," *Optical Materials Express*, vol. 5, no. 1, p. 29, 2015.

[211] Y. Jiang, M. A. Green, R. Sheng, and A. Ho-Baillie, "Room temperature optical properties of organic-inorganic lead halide perovskites," *Solar Energy Materials and Solar Cells*, vol. 137, pp. 253–257, 6 2015.

[212] A. Marronnier, H. Lee, H. Lee, M. Kim, C. Eypert, J. P. Gaston, G. Roma, D. Tondelier, B. Geffroy, and Y. Bonnassieux, "Electrical and optical degradation study of methylammonium-based perovskite materials under ambient conditions," *Solar Energy Materials and Solar Cells*, vol. 178, pp. 179–185, 5 2018.

[213] X. Wang, J. Gong, X. Shan, M. Zhang, Z. Xu, R. Dai, Z. Wang, S. Wang, X. Fang, and Z. Zhang, "In Situ Monitoring of Thermal Degradation of CH 3 NH 3 PbI 3 Films by Spectroscopic Ellipsometry," *Journal of Physical Chemistry C*, vol. 123, no. 2, pp. 1362–1369, 2019.

[214] Q. Lin, A. Armin, R. C. R. Nagiri, P. L. Burn, and P. Meredith, "Electro-optics of perovskite solar cells," *Nature Photonics*, vol. 9, no. 2, pp. 106–112, 2015.

[215] A. M. Leguy, Y. Hu, M. Campoy-Quiles, M. I. Alonso, O. J. Weber, P. Azarhoosh, M. Van Schilfgaarde, M. T. Weller, T. Bein, J. Nelson, P. Docampo, and P. R. Barnes, "Reversible hydration of CH3NH3PbI3 in films, single crystals, and solar cells," *Chemistry of Materials*, vol. 27, no. 9, pp. 3397–3407, 2015.

[216] A. M. Leguy, P. Azarhoosh, M. I. Alonso, M. Campoy-Quiles, O. J. Weber, J. Yao, D. Bryant, M. T. Weller, J. Nelson, A. Walsh, M. Van Schilfgaarde, and P. R. Barnes, "Experimental and theoretical optical properties of methylammonium lead halide perovskites," *Nanoscale*, vol. 8, no. 12, pp. 6317–6327, 2016.

[217] P. Löper, M. Stuckelberger, B. Niesen, J. Werner, M. Filipič, S. J. Moon, J. H. Yum, M. Topič, S. De Wolf, and C. Ballif, "Complex refractive index spectra of CH3NH3PbI3 perovskite thin films determined by spectroscopic ellipsometry and spectrophotometry," *Journal of Physical Chemistry Letters*, vol. 6, no. 1, pp. 66–71, 2015.

[218] Y. Jiang, A. M. Soufiani, A. Gentle, F. Huang, A. Ho-Baillie, and M. A. Green, "Temperature dependent optical properties of CH 3 NH 3 PbI 3 perovskite by spectroscopic ellipsometry," *Applied Physics Letters*, vol. 108, no. 6, p. 61905, 2016.

[219] M. van Eerden, M. Jaysankar, A. Hadipour, T. Merckx, J. J. Schermer, T. Aernouts, J. Poortmans, and U. W. Paetzold, "Optical Analysis of Planar Multicrystalline Perovskite Solar Cells," *Advanced Optical Materials*, vol. 5, p. 1700151, 9 2017.

[220] D. O. Demchenko, N. Izyumskaya, M. Feneberg, V. Avrutin, Özgür, R. Goldhahn, and H. Morkoç, "Optical properties of the organic-inorganic hybrid perovskite C H3 N H3Pb I3: Theory and experiment," *Physical Review B*, vol. 94, no. 7, p. 75206, 2016.

[221] P. F. Ndione, Z. Li, and K. Zhu, "Effects of alloying on the optical properties of organic-inorganic lead halide perovskite thin films," *Journal of Materials Chemistry C*, vol. 4, no. 33, pp. 7775–7782, 2016.

[222] J. A. Guerra, A. Tejada, L. Korte, L. Kegelmann, J. A. Töfflinger, S. Albrecht, B. Rech, and R. Weingärtner, "Determination of the complex refractive index and optical bandgap of CH3NH3PbI3 thin films," *Journal of Applied Physics*, vol. 121, p. 173104, 5 2017.

[223] S. Brittman and E. C. Garnett, "Measuring n and k at the Microscale in Single Crystals of CH3NH3PbBr3 Perovskite," *Journal of Physical Chemistry C*, vol. 120, no. 1, pp. 616–620, 2016.

[224] X. Chen, Y. Wang, J. Song, X. Li, J. Xu, H. Zeng, and H. Sun, "Temperature Dependent Reflectance and Ellipsometry Studies on a CsPbBr 3 Single Crystal," *Journal of Physical Chemistry C*, vol. 123, no. 16, pp. 10564–10570, 2019.

[225] H. Shirai, "Spectroscopic Ellipsometry Study of Organic-Inorganic Halide: FAPbIxBr3x Perovskite Thin Films by Two-Step Method," in *Ellipsometry - Principles and Techniques for Materials Characterization*, InTech, 2017.

[226] M. Zhao, Y. Shi, J. Dai, and J. Lian, "Ellipsometric study of the complex optical constants of a CsPbBr 3 perovskite thin film," *Journal of Materials Chemistry C*, vol. 6, no. 39, pp. 10450–10455, 2018.

[227] M. S. Alias, I. Dursun, M. I. Saidaminov, E. M. Diallo, P. Mishra, T. K. Ng, O. M. Bakr, and B. S. Ooi, "Optical constants of CH_3NH_3PbBr_3 perovskite thin films

measured by spectroscopic ellipsometry," *Optics Express*, vol. 24, no. 15, p. 16586, 2016.

[228] J. Werner, G. Nogay, F. Sahli, T. C. J. Yang, M. Bräuninger, G. Christmann, A. Walter, B. A. Kamino, P. Fiala, P. Löper, S. Nicolay, Q. Jeangros, B. Niesen, and C. Ballif, "Complex Refractive Indices of Cesium-Formamidinium-Based Mixed-Halide Perovskites with Optical Band Gaps from 1.5 to 1.8 eV," *ACS Energy Letters*, vol. 3, no. 3, pp. 742–747, 2018.

[229] T. J. Whitcher, J. X. Zhu, X. Chi, H. Hu, D. Zhao, T. C. Asmara, X. Yu, M. B. Breese, A. H. Castro Neto, Y. M. Lam, A. T. Wee, E. E. Chia, and A. Rusydi, "Importance of Electronic Correlations and Unusual Excitonic Effects in Formamidinium Lead Halide Perovskites," *Physical Review X*, vol. 8, no. 2, 2018.

[230] B. Xia, Z. Wu, H. Dong, J. Xi, W. Wu, T. Lei, K. Xi, F. Yuan, B. Jiao, L. Xiao, Q. Gong, and X. Hou, "Formation of ultrasmooth perovskite films toward highly efficient inverted planar heterojunction solar cells by micro-flowing anti-solvent deposition in air," *Journal of Materials Chemistry A*, vol. 4, pp. 6295–6303, 4 2016.

[231] Y. Gao, L. Yang, F. Wang, Y. Sui, Y. Sun, M. Wei, J. Cao, and H. Liu, "Anti-solvent surface engineering via diethyl ether to enhance the photovoltaic conversion efficiency of perovskite solar cells to 18.76%," *Superlattices and Microstructures*, vol. 113, pp. 761–768, 12 2018.

[232] H. Fujiwara, M. Kato, M. Tamakoshi, T. Miyadera, and M. Chikamatsu, "Optical Characteristics and Operational Principles of Hybrid Perovskite Solar Cells," *Physica Status Solidi (A) Applications and Materials Science*, vol. 215, no. 12, 2018.

[233] V. D'Innocenzo, A. R. Srimath Kandada, M. De Bastiani, M. Gandini, and A. Petrozza, "Tuning the light emission properties by band gap engineering in hybrid lead-halide perovskite.," *Journal of the American Chemical Society*, vol. 136, no. 51, pp. 17730–17733, 2014.

[234] H. Kunugita, T. Hashimoto, Y. Kiyota, Y. Udagawa, Y. Takeoka, Y. Nakamura, J. Sano, T. Matsushita, T. Kondo, T. Miyasaka, and K. Ema, "Excitonic Feature in Hybrid Perovskite CH3NH3PbBr3 single crystals," *Chemistry Letters*, vol. 44, no. 6, pp. 852–854, 2015.

[235] S. Nah, B. Spokoyny, C. Stoumpos, C. M. Soe, M. Kanatzidis, and E. Harel, "Spatially segregated free-carrier and exciton populations in individual lead halide perovskite grains," *Nature Photonics*, vol. 11, no. 5, pp. 285–289, 2017.

[236] X. Wu, M. T. Trinh, D. Niesner, H. Zhu, Z. Norman, J. S. Owen, O. Yaffe, B. J. Kudisch, and X. Y. Zhu, "Trap states in lead iodide perovskites," *Journal of the American Chemical Society*, vol. 137, no. 5, pp. 2089–2096, 2015.

[237] T. Wang, B. Daiber, J. M. Frost, S. A. Mann, E. C. Garnett, A. Walsh, and B. Ehrler, "Indirect to direct bandgap transition in methylammonium lead halide perovskite," *Energy and Environmental Science*, vol. 10, no. 2, pp. 509–515, 2017.

[238] J. Kim, S.-H. Lee, J. H. Lee, and K.-h. Hong, "The Role of Intrinsic Defects in Methylammonium Lead Iodide Perovskite," *The Journal of Physical Chemistry Letters*, vol. 5, no. 8, pp. 1312–1317, 2014.

[239] E. Edri, S. Kirmayer, S. Mukhopadhyay, K. Gartsman, G. Hodes, and D. Cahen, "Elucidating the charge carrier separation and working mechanism of CH3NH3PbI(3-x)Cl(x) perovskite solar cells.," *Nature communications*, vol. 5, p. 3461, 3 2014.

[240] K. Miyano, N. Tripathi, M. Yanagida, and Y. Shirai, "Lead Halide Perovskite Photovoltaic as a Model p-i-n Diode.," *Accounts of chemical research*, vol. 49, pp. 303–10, 2 2016.

[241] D. Meggiolaro, E. Mosconi, F. De Angelis, S. G. Motti, A. J. Barker, J. Ball, C. Andrea Riccardo Perini, A. Petrozza, and F. Deschler, "Iodine chemistry determines the defect tolerance of lead-halide perovskites," *Energy and Environmental Science*, vol. 11, pp. 702–713, 3 2018.

[242] M. H. Du, "Density functional calculations of native defects in CH3NH3PbI3: Effects of spin - Orbit coupling and self-interaction error," *Journal of Physical Chemistry Letters*, vol. 6, no. 8, pp. 1461–1466, 2015.

[243] A. D. Wright, R. L. Milot, G. E. Eperon, H. J. Snaith, M. B. Johnston, and L. M. Herz, "Band-Tail Recombination in Hybrid Lead Iodide Perovskite," *Advanced Functional Materials*, vol. 27, p. 1700860, 6 2017.

[244] T. Du, J. Kim, J. Ngiam, S. Xu, P. R. Barnes, J. R. Durrant, and M. A. McLachlan, "Elucidating the Origins of Subgap Tail States and Open-Circuit Voltage in Methylammonium Lead Triiodide Perovskite Solar Cells," *Advanced Functional Materials*, vol. 28, p. 1801808, 8 2018.

[245] T. Leijtens, G. E. Eperon, A. J. Barker, G. Grancini, W. Zhang, J. M. Ball, A. R. S. Kandada, H. J. Snaith, and A. Petrozza, "Carrier trapping and recombination: The role of defect physics in enhancing the open circuit voltage of metal halide perovskite solar cells," *Energy and Environmental Science*, vol. 9, no. 11, pp. 3472–3481, 2016.

[246] W.-J. Yin, T. Shi, and Y. Yan, "Unusual defect physics in CH3NH3PbI3 perovskite solar cell absorber.," *Applied Physics Letters*, vol. 104, no. 6, pp. 1–063903, 2014.

[247] C. L. Davies, M. R. Filip, J. B. Patel, T. W. Crothers, C. Verdi, A. D. Wright, R. L. Milot, F. Giustino, M. B. Johnston, and L. M. Herz, "Bimolecular recombination in methylammonium lead triiodide perovskite is an inverse absorption process," *Nature Communications*, vol. 9, no. 1, 2018.

[248] Y. P. Varshni, "Temperature dependence of the energy gap in semiconductors," *Physica*, vol. 34, pp. 149–154, 1 1967.

[249] J. M. Frost, K. T. Butler, F. Brivio, C. H. Hendon, M. Van Schilfgaarde, and A. Walsh, "Atomistic origins of high-performance in hybrid halide perovskite solar cells," *Nano Letters*, vol. 14, no. 5, pp. 2584–2590, 2014.

[250] N. Sestu, M. Cadelano, V. Sarritzu, F. Chen, D. Marongiu, R. Piras, M. Mainas, F. Quochi, M. Saba, A. Mura, and G. Bongiovanni, "Absorption F-Sum Rule

for the Exciton Binding Energy in Methylammonium Lead Halide Perovskites," *Journal of Physical Chemistry Letters*, vol. 6, no. 22, pp. 4566–4572, 2015.

[251] M. I. Dar, N. Arora, S. M. Zakeeruddin, M. Grätzel, G. Jacopin, S. Meloni, A. Boziki, U. Rothlisberger, and A. Mattoni, "Origin of unusual bandgap shift and dual emission in organic-inorganic lead halide perovskites," *Science Advances*, vol. 2, no. 10, 2016.

[252] M. A. Pérez-Osorio, R. L. Milot, M. R. Filip, J. B. Patel, L. M. Herz, M. B. Johnston, and F. Giustino, "Vibrational Properties of the Organic-Inorganic Halide Perovskite CH3NH3PbI3 from Theory and Experiment: Factor Group Analysis, First-Principles Calculations, and Low-Temperature Infrared Spectra," *Journal of Physical Chemistry C*, vol. 119, pp. 25703–25718, 11 2015.

[253] A. D. Wright, C. Verdi, R. L. Milot, G. E. Eperon, M. A. Pérez-Osorio, H. J. Snaith, F. Giustino, M. B. Johnston, and L. M. Herz, "Electron-phonon coupling in hybrid lead halide perovskites," *Nature Communications*, vol. 7, 2016.

[254] M. Karakus, S. A. Jensen, F. D'Angelo, D. Turchinovich, M. Bonn, and E. Cánovas, "Phonon-Electron Scattering Limits Free Charge Mobility in Methylammonium Lead Iodide Perovskites," *Journal of Physical Chemistry Letters*, vol. 6, no. 24, pp. 4991–4996, 2015.

[255] A. M. Leguy, A. R. Goñi, J. M. Frost, J. Skelton, F. Brivio, X. Rodríguez-Martínez, O. J. Weber, A. Pallipurath, M. I. Alonso, M. Campoy-Quiles, M. T. Weller, J. Nelson, A. Walsh, and P. R. Barnes, "Dynamic disorder, phonon lifetimes, and the assignment of modes to the vibrational spectra of methylammonium lead halide perovskites," *Physical Chemistry Chemical Physics*, vol. 18, no. 39, pp. 27051–27066, 2016.

[256] M. N. Saha, "On a physical theory of stellar spectra," *Journal of Astrophysics and Astronomy*, vol. 15, pp. 203–221, 5 1994.

[257] J. Szczytko, L. Kappei, J. Berney, F. Morier-Genoud, M. T. Portella-Oberli, and B. Deveaud, "Determination of the exciton formation in quantum wells from time-resolved interband luminescence," *Physical Review Letters*, vol. 93, p. 137401, 9 2004.

[258] T. H. Gfroerer, L. P. Priestley, F. E. Weindruch, and M. W. Wanlass, "Defect-related density of states in low-band gap InxGa1-xAs/InAsyP1-y double heterostructures grown on InP substrates," *Applied Physics Letters*, vol. 80, pp. 4570–4572, 6 2002.

[259] A. Sadhanala, F. Deschler, T. H. Thomas, S. E. Dutton, K. C. Goedel, F. C. Hanusch, M. L. Lai, U. Steiner, T. Bein, P. Docampo, D. Cahen, and R. H. Friend, "Preparation of single-phase films of CH3NH3Pb(I 1- xBrx)3 with sharp optical band edges," *Journal of Physical Chemistry Letters*, vol. 5, pp. 2501–2505, 8 2014.

[260] T. Kirchartz, T. Markvart, U. Rau, and D. A. Egger, "Impact of Small Phonon Energies on the Charge-Carrier Lifetimes in Metal-Halide Perovskites," *J. Phys. Chem. Lett*, vol. 9, pp. 939–946, 2018.

[261] D. W. Dequilettes, S. Koch, S. Burke, R. K. Paranji, A. J. Shropshire, M. E. Ziffer, and D. S. Ginger, "Photoluminescence Lifetimes Exceeding 8 μs and Quantum Yields Exceeding 30% in Hybrid Perovskite Thin Films by Ligand Passivation," *ACS Energy Letters*, vol. 1, no. 2, pp. 438–444, 2016.

[262] J. M. Richter, M. Abdi-Jalebi, A. Sadhanala, M. Tabachnyk, J. P. Rivett, L. M. Pazos-Outón, K. C. Gödel, M. Price, F. Deschler, and R. H. Friend, "Enhancing photoluminescence yields in lead halide perovskites by photon recycling and light out-coupling," *Nature Communications*, vol. 7, p. 13941, 12 2016.

[263] J. Li, Q. Yu, B. Lu, H. He, and Z. Ye, "Ambience dependent photoluminescence reveals the localization and trap filling effects in CH3NH3PbI3-xClx perovskite films," *J. Mater. Chem. C*, vol. 5, pp. 54–58, 2016.

[264] M. Anaya, J. F. Galisteo-López, M. E. Calvo, J. P. Espinós, and H. Míguez, "Origin of Light-Induced Photophysical Effects in Organic Metal Halide Perovskites in

the Presence of Oxygen," *Journal of Physical Chemistry Letters*, vol. 9, no. 14, pp. 3891–3896, 2018.

[265] R. Brenes, C. Eames, V. Bulović, M. S. Islam, and S. D. Stranks, "The Impact of Atmosphere on the Local Luminescence Properties of Metal Halide Perovskite Grains," *Advanced Materials*, vol. 30, p. 1706208, 4 2018.

[266] S. G. Motti, M. Gandini, A. J. Barker, J. M. Ball, A. R. Srimath Kandada, and A. Petrozza, "Photoinduced Emissive Trap States in Lead Halide Perovskite Semiconductors," *ACS Energy Letters*, pp. 726–730, 2016.

[267] C. Li, Y. Zhong, C. A. M. Luna, T. Unger, K. Deichsel, A. Gräser, J. Köhler, A. Köhler, R. Hildner, and S. Huettner, "Emission enhancement and intermittency in polycrystalline organolead halide perovskite films," *Molecules*, vol. 21, p. 1081, 8 2016.

[268] N. K. Noel, A. Abate, S. D. Stranks, E. S. Parrott, V. M. Burlakov, A. Goriely, and H. J. Snaith, "Enhanced Photoluminescence and Solar Cell Performance ¡i¿via¡/i¿ Lewis Base Passivation of OrganicInorganic Lead Halide Perovskites," *ACS Nano*, vol. 8, pp. 9815–9821, 10 2014.

[269] M. Abdi-Jalebi, Z. Andaji-Garmaroudi, S. Cacovich, C. Stavrakas, B. Philippe, J. M. Richter, M. Alsari, E. P. Booker, E. M. Hutter, A. J. Pearson, S. Lilliu, T. J. Savenije, H. Rensmo, G. Divitini, C. Ducati, R. H. Friend, and S. D. Stranks, "Maximizing and stabilizing luminescence from halide perovskites with potassium passivation," *Nature*, vol. 555, pp. 497–501, 3 2018.

[270] W. Tress, N. Marinova, T. Moehl, S. M. Zakeeruddin, M. K. Nazeeruddin, and M. Grätzel, "Understanding the rate-dependent JV hysteresis, slow time component, and aging in CH ¡sub¿3¡/sub¿ NH ¡sub¿3¡/sub¿ PbI ¡sub¿3¡/sub¿ perovskite solar cells: the role of a compensated electric field," *Energy Environ. Sci.*, vol. 8, no. 3, pp. 995–1004, 2015.

[271] T. S. Sherkar, C. Momblona, L. Gil-Escrig, J. Ávila, M. Sessolo, H. J. Bolink, and L. J. A. Koster, "Recombination in Perovskite Solar Cells: Significance of Grain

Boundaries, Interface Traps, and Defect Ions," *ACS Energy Letters*, vol. 2, no. 5, pp. 1214–1222, 2017.

[272] G. Grancini, A. R. Srimath Kandada, J. M. Frost, A. J. Barker, M. De Bastiani, M. Gandini, S. Marras, G. Lanzani, A. Walsh, and A. Petrozza, "Role of microstructure in the electron-hole interaction of hybrid lead halide perovskites," *Nature Photonics*, vol. 9, pp. 695–701, 10 2015.

[273] X. Jiang, J. M. Hoffman, C. C. Stoumpos, M. G. Kanatzidis, and E. Harel, "Transient Sub-Bandgap States at Grain Boundaries of CH3NH3PbI3 Perovskite Act as Fast Temperature Relaxation Centers," *ACS Energy Letters*, vol. 4, no. 7, pp. 1741–1747, 2019.

[274] C. G. Bischak, E. M. Sanehira, J. T. Precht, J. M. Luther, and N. S. Ginsberg, "Heterogeneous Charge Carrier Dynamics in Organic-Inorganic Hybrid Materials: Nanoscale Lateral and Depth-Dependent Variation of Recombination Rates in Methylammonium Lead Halide Perovskite Thin Films," *Nano Letters*, vol. 15, no. 7, pp. 4799–4807, 2015.

[275] S. Shao, M. Abdu-Aguye, T. S. Sherkar, H.-H. Fang, S. Adjokatse, G. t. Brink, B. J. Kooi, L. J. A. Koster, and M. A. Loi, "The Effect of the Microstructure on Trap-Assisted Recombination and Light Soaking Phenomenon in Hybrid Perovskite Solar Cells," *Advanced Functional Materials*, vol. 26, pp. 8094–8102, 11 2016.

[276] C. Eames, J. M. Frost, P. R. Barnes, B. C. O'Regan, A. Walsh, and M. S. Islam, "Ionic transport in hybrid lead iodide perovskite solar cells," *Nature Communications*, vol. 6, p. 7497, 11 2015.

[277] S. Van Reenen, M. Kemerink, and H. J. Snaith, "Modeling Anomalous Hysteresis in Perovskite Solar Cells," *Journal of Physical Chemistry Letters*, vol. 6, no. 19, pp. 3808–3814, 2015.

[278] W. Li, S. K. Yadavalli, D. Lizarazo-Ferro, M. Chen, Y. Zhou, N. P. Padture, and R. Zia, "Subgrain special boundaries in halide perovskite thin films restrict carrier diffusion," *ACS Energy Letters*, vol. 3, pp. 2669–2670, 11 2018.

[279] J. Hieulle, C. Stecker, R. Ohmann, L. K. Ono, and Y. Qi, "Scanning Probe Microscopy Applied to Organic-Inorganic Halide Perovskite Materials and Solar Cells," *Small Methods*, vol. 2, no. 1, p. 1700295, 2018.

[280] Y. Luo, S. Aharon, M. Stuckelberger, E. Magaña, B. Lai, M. I. Bertoni, L. Etgar, and D. P. Fenning, "The Relationship between Chemical Flexibility and Nanoscale Charge Collection in Hybrid Halide Perovskites," 5 2018.

[281] M. Vrućinić, C. Matthiesen, A. Sadhanala, G. Divitini, S. Cacovich, S. E. Dutton, C. Ducati, M. Atatüre, H. Snaith, R. H. Friend, H. Sirringhaus, and F. Deschler, "Local Versus Long-Range Diffusion Effects of Photoexcited States on Radiative Recombination in Organic-Inorganic Lead Halide Perovskites," *Advanced Science*, pp. n/a–n/a, 2015.

[282] J. L. Garrett, E. M. Tennyson, M. Hu, J. Huang, J. N. Munday, and M. S. Leite, "Real-Time Nanoscale Open-Circuit Voltage Dynamics of Perovskite Solar Cells," *Nano Letters*, vol. 17, pp. 2554–2560, 4 2017.

[283] D. Ha, Y. Yoon, P. M. Haney, N. B. Zhitenev, and I. J. Park, "Nanoimaging of local photocurrent in hybrid perovskite solar cells via near-field scanning photocurrent microscopy," in *Organic, Hybrid, and Perovskite Photovoltaics XIX* (K. Lee, Z. H. Kafafi, and P. A. Lane, eds.), vol. 10737, p. 37, SPIE, 9 2018.

[284] M. Lv, X. Dong, X. Fang, B. Lin, S. Zhang, J. Ding, and N. Yuan, "A promising alternative solvent of perovskite to induce rapid crystallization for high-efficiency photovoltaic devices," *RSC Advances*, vol. 5, pp. 20521–20529, 2 2015.

[285] W. Zhang, S. Pathak, N. Sakai, T. Stergiopoulos, P. K. Nayak, N. K. Noel, A. A. Haghighirad, V. M. Burlakov, D. W. Dequilettes, A. Sadhanala, W. Li, L. Wang, D. S. Ginger, R. H. Friend, and H. J. Snaith, "Enhanced optoelectronic quality of perovskite thin films with hypophosphorous acid for planar heterojunction solar cells," *Nature Communications*, vol. 6, 2015.

[286] G. Li, T. Zhang, and Y. Zhao, "Hydrochloric acid accelerated formation of planar CH¡inf¿3¡/inf¿NH¡inf¿3¡/inf¿PbI¡inf¿3¡/inf¿ perovskite with high humidity tolerance," *Journal of Materials Chemistry A*, vol. 3, pp. 19674–19678, 9 2015.

[287] P. W. Liang, C. Y. Liao, C. C. Chueh, F. Zuo, S. T. Williams, X. K. Xin, J. Lin, and A. K.-Y. Jen, "Additive enhanced crystallization of solution-processed perovskite for highly efficient planar-heterojunction solar cells," *Advanced Materials*, vol. 26, pp. 3748–3754, 6 2014.

[288] S. T. Williams, F. Zuo, C. C. Chueh, C. Y. Liao, P. W. Liang, and A. K. Y. Jen, "Role of chloride in the morphological evolution of organo-lead halide perovskite thin films," *ACS Nano*, vol. 8, pp. 10640–10654, 10 2014.

[289] C. Wehrenfennig, M. Liu, H. J. Snaith, M. B. Johnston, and L. M. Herz, "Homogeneous Emission Line Broadening in the Organo Lead Halide Perovskite CH3NH3PbI3-xClx.," *The journal of physical chemistry letters*, vol. 5, no. 8, pp. 1300–6, 2014.

[290] C. R. Kagan, E. Lifshitz, E. H. Sargent, and D. V. Talapin, "Building devices from colloidal quantum dots," *Science*, vol. 353, p. aac5523, 8 2016.

[291] B. Mahler, P. Spinicelli, S. Buil, X. Quelin, J. P. Hermier, and B. Dubertret, "Towards non-blinking colloidal quantum dots," *Nature Materials*, vol. 7, no. 8, pp. 659–664, 2008.

[292] X. Dai, Z. Zhang, Y. Jin, Y. Niu, H. Cao, X. Liang, L. Chen, J. Wang, and X. Peng, "Solution-processed, high-performance light-emitting diodes based on quantum dots," *Nature*, vol. 515, no. 7525, pp. 96–99, 2014.

[293] J. Song, J. Li, X. Li, L. Xu, Y. Dong, and H. Zeng, "Quantum Dot Light-Emitting Diodes Based on Inorganic Perovskite Cesium Lead Halides (CsPbX3)," *Advanced Materials*, vol. 27, pp. 7162–7167, 11 2015.

[294] Q. Sun, Y. A. Wang, L. S. Li, D. Wang, T. Zhu, J. Xu, C. Yang, and Y. Li, "Bright, multicoloured light-emitting diodes based on quantum dots," *Nature Photonics*, vol. 1, no. 12, pp. 717–722, 2007.

[295] Y. Shirasaki, G. J. Supran, M. G. Bawendi, and V. Bulović, "Emergence of colloidal quantum-dot light-emitting technologies," 2013.

[296] A. Kongkanand, K. Tvrdy, K. Takechi, M. Kuno, and P. V. Kamat, "Quantum dot solar cells. Tuning photoresponse through size and shape control of CdSe-TiO2 architecture," *Journal of the American Chemical Society*, vol. 130, no. 12, pp. 4007–4015, 2008.

[297] I. Robel, V. Subramanian, M. Kuno, and P. V. Kamat, "Quantum dot solar cells. Harvesting light energy with CdSe nanocrystals molecularly linked to mesoscopic TiO2 films," *Journal of the American Chemical Society*, vol. 128, no. 7, pp. 2385–2393, 2006.

[298] E. H. Sargent, "Colloidal quantum dot solar cells," *Nature Photonics*, vol. 6, pp. 1–3, 3 2012.

[299] P. V. Kamat, "Quantum dot solar cells. Semiconductor nanocrystals as light harvesters," *Journal of Physical Chemistry C*, vol. 112, pp. 18737–18753, 12 2008.

[300] W. U. Huynh, J. J. Dittmer, and A. P. Alivisatos, "Hybrid Nanorod-Polymer Solar Cells," *Science*, vol. 295, no. 5564, pp. 2425 LP – 2427, 2002.

[301] D. Cui, J. Xu, T. Zhu, G. Paradee, S. Ashok, and M. Gerhold, "Harvest of near infrared light in PbSe nanocrystal-polymer hybrid photovoltaic cells," *Applied Physics Letters*, vol. 88, no. 18, pp. 1–4, 2006.

[302] J. Han, S. Luo, X. Yin, Y. Zhou, H. Nan, J. Li, X. Li, D. Oron, H. Shen, and H. Lin, "Hybrid PbS Quantum-Dot-in-Perovskite for High-Efficiency Perovskite Solar Cell," *Small*, vol. 1801016, p. 1801016, 2018.

[303] Y. Cabrera, S. M. Rupich, R. Shaw, B. Anand, M. De Anda Villa, R. Rahman, A. Dangerfield, Y. N. Gartstein, A. V. Malko, and Y. J. Chabal, "Energy transfer from colloidal nanocrystals to strongly absorbing perovskites," *Nanoscale*, vol. 9, no. 25, pp. 8695–8702, 2017.

[304] M. N. Lintangpradipto, N. Tsevtkov, B. C. Moon, and J. K. Kang, "Size-controlled CdSe quantum dots to boost light harvesting capability and stability of perovskite photovoltaic cells," *Nanoscale*, vol. 9, no. 28, pp. 10075–10083, 2017.

[305] H. J. Snaith, A. Abate, J. M. Ball, G. E. Eperon, T. Leijtens, N. K. Noel, S. D. Stranks, J. T. W. Wang, K. Wojciechowski, and W. Zhang, "Anomalous hysteresis in perovskite solar cells," *Journal of Physical Chemistry Letters*, vol. 5, no. 9, pp. 1511–1515, 2014.

[306] L. Cojocaru, S. Uchida, P. V. Jayaweera, H. Kaneko, J. Nakazaki, T. Kubo, and H. Segawa, "Origin of the hysteresis in I-V curves for planar structure perovskite solar cells rationalized with a surface boundary-induced capacitance model," *Chemistry Letters*, vol. 44, no. 12, pp. 1750–1752, 2015.

[307] E. L. Unger, E. T. Hoke, C. D. Bailie, W. H. Nguyen, A. R. Bowring, T. Heumüller, M. G. Christoforo, and M. D. McGehee, "Hysteresis and transient behavior in current-voltage measurements of hybrid-perovskite absorber solar cells," *Energy and Environmental Science*, vol. 7, no. 11, pp. 3690–3698, 2014.